Anisotropic Stress, Plasticity, and Microstructural Evolution in Crystalline Materials From Grain Boundaries to Nanostructures

Liu, K.

Important note

To cite this publication, please use the final published version (if applicable).
Please check the document version above.

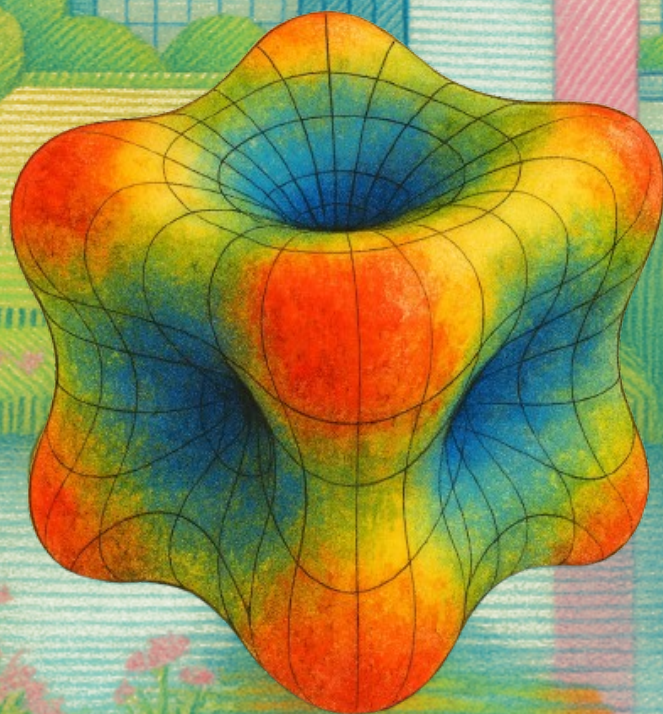# Anisotropic Stress, Plasticity, and Microstructural Evolution in Crystalline Materials:

From Grain Boundaries to Nanostructures

Kai Liu 刘 凯

Anisotropic Stress, Plasticity, and Microstructural Evolution in Crystalline Materials: From Grain Boundaries to Nanostructures

Anisotropic Stress, Plasticity, and Microstructural Evolution in Crystalline Materials: From Grain Boundaries to Nanostructures

Dissertation

for the purpose of obtaining the degree of doctor
at Delft University of Technology
by the authority of the Rector Magnificus Prof. dr. ir. T.H.J.J. van der Hagen,
chair of the Board for Doctorates,
to be defended publicly on
Monday 6 October 2025 at 17:30 o'clock

by

Kai LIU

Master of Engineering in Materials Science,
Harbin Institute of Technology, China,
born in Shaanxi, China.

This dissertation has been approved by the promotors.

Composition of the doctoral committee:

Rector Magnificus,	chairperson
Dr. ir. M.H.F. Sluiter,	Delft University of Technology, promotor
Dr. P. Dey,	Delft University of Technology, copromotor

Independent members:

Prof. dr. ir. L.A.I. Kestens,	Delft University of Technology
Prof. dr. ir. A.H. van den Boogaard,	University of Twente
Dr. F. Maresca,	Rijksuniversiteit Groningen
Prof. dr. ir. R. H. Petrov,	Ghent University
Dr. V.A. Popovich,	Delft University of Technology
Prof. dr. M.J. Santofimia Navarro,	Delft University of Technology, reserve member

Contents

Summary

Metallic materials exhibit structural and performance anisotropy at various scales, including the crystal structure, microstructure, and bulk levels. The anisotropy influences how stress and strain distribute within the material. The localized stress concentration is closely related to deformation and several failure mechanisms. A systematic exploration of the anisotropy can deepen our understanding of stress concentration and material failure, and guide the design of high-performance materials tailored for specific applications. Additionally, this work supports sustainable development by enhancing the service life and recyclability of metallic materials—an increasingly critical priority in materials science.

Anisotropy manifests itself on various length scales. The smallest length scale is that of the crystal structure. The regular arrangement of atoms in a crystal causes the elastic properties of all crystal structures to vary in different directions, even in the highly symmetric cubic crystal system. When subjected to external stress, additional stress fields arise near grain boundaries due to the difference in the Young's modulus across the grain boundary, known as incompatibility stress. In Chapter 2, I explore all possible grain boundaries in crystal structures under uniaxial stress. By introducing a decomposition method for rotating the crystal elastic tensor, the explicit expressions for incompatibility stress are derived in terms of external load, elastic properties, and grain orientations. For all cubic crystals, the highest incompatibility stress arises when a $(100)//(111)$ grain boundary is perpendicular to the uniaxial external load. The incompatibility stress is insensitive to the in-plane rotation. For general grain boundaries, the incompatibility stress is proportional to the difference in the reciprocal of Young's modulus across the grain boundary. In contrast to previous studies that focus on specific grain boundaries and metals, this work offers a broader and more systematic analysis of the stress state near grain boundaries.

In addition to the orientation difference between crystals on either side of the grain boundary, the orientation of a grain boundary relative to the applied external stress also influences the variation in the incompatibility stress. Therefore, I expanded the investigation of incompatibility stress to include grain boundaries with arbitrary inclinations. For cubic crystals, the incompatibility stress is demonstrated to arise solely from the deviatoric stress component of any stress tensor. Employing a simulated annealing algorithm, I explored the relationship between the maximum incompatibility stress at grain boundaries and the inclination angle for materials

with varying degrees of anisotropy. For materials with low anisotropy, grain boundaries perpendicular to the uniaxial loads exhibit the highest incompatibility stress. In contrast, for highly anisotropic materials, grain boundaries with inclination angles of 40 to 50 degrees show the highest incompatibility stress. This conclusion is applicable to all materials with cubic crystal structure, including metals, ceramics, and intermetallics.

Elastic anisotropy induces a heterogeneous stress field in polycrystalline metallic materials. At the grain scale, the mechanical properties of metallic materials with heterogeneous structures exhibit significant anisotropy due to their structural characteristics. Here, I investigate the anisotropy in the yield strength and plastic deformation mechanisms of pearlite under various loading conditions. Pearlite consists of ferrite and cementite, forming a regular lamellar microstructure. By developing a periodic bicrystal model to represent pearlite, the relationship between the activation barrier of the slip systems in the two phases and the loading direction is revealed. In molecular dynamics simulations, the loading is applied conventionally along one of the principal axes of the simulation box. I found that previous studies, which focused on loading directions aligned with the unit cell basis vectors of cementite, are not adequate to capture the anisotropy inherent in pearlite deformation. To address this limitation, I specifically designed models with varying periodicities. Therefore, tension can be applied in multiple directions while the atomistic configurations remain identical. This approach reveals a significant loading direction dependence of the plastic deformation of pearlite. Using the new loading approach, simulations show that under specific loading conditions, the slip band can be activated in cementite at a stress level lower than that of ferrite. For pearlite colonies with various orientations, the stresses corresponding to the initiation of plastic deformation vary strongly. This work contributes to a more comprehensive understanding of the deformation and strengthening mechanisms of pearlite. Additionally, it quantitatively elucidates the effects of factors such as the Schmid factor, interfacial dislocations, and the volume fractions of the two phases on pearlite plastic deformation. Moreover, it provides guidance for the design of high-performance materials with lamellar microstructures that are commonly found as products of eutectic or eutectoid transformations.

Metallic materials with nanoscale porous structures, such as sintered copper nanoparticles, exhibit considerable potential for applications in fields such as electronic packaging. Their porous structure induces anisotropy in macroscopic mechanical and physical properties. In Chapter 5, I employed molecular dynamics simulations to study the stress-induced sintering densification of copper nanoparticles and their tensile behavior along various directions. In collaboration with experimental characterization, two parameters are introduced to quantify the anisotropy of nanoscale porous structures: the standard deviation of the areal

density and the orientation distribution of sintering necks. It is found that applying external uniaxial stress during sintering reduces density variation along the stress direction, with the sintering necks tending to align perpendicular to the applied stress. These structural characteristics improve strength and toughness along the sintering stress direction compared to other orientations. This work provides a methodology for the design and performance optimization of porous sintered structures.

In summary, this research begins by modeling the stress concentration at grain boundaries under uniaxial stress using a bicrystal model, identifying the conditions for maximum stress concentration across all cubic crystals. It then extends to inclined grain boundaries and general external loads, revealing that incompatibility stress in highly anisotropic materials strongly depends on grain boundary inclination. At the atomic scale, molecular dynamics simulations explore the deformation of pearlite. The pronounced anisotropy of plasticity under various loading conditions is uncovered. On a larger scale, the anisotropy in the microstructure and mechanical properties of sintered copper nanoparticles is investigated through a combination of experiments and simulations. The stress distribution, plastic behavior, and microstructural evolution in polycrystalline metallic materials display anisotropy, influencing their mechanical properties. In certain cases, the overall performance of a material is limited by its lowest performing region. A good understanding of anisotropy can guide material design to minimize its adverse effects. Alternatively, harnessing anisotropy offers the potential to create advanced materials with enhanced performance in targeted directions.

Samenvatting

Metallische materialen vertonen anisotropie in structuur en in eigenschappen op verschillende schalen, waaronder de kristalstructuur, microstructuur en op bulk niveau. De anisotropie beïnvloedt hoe spanning en vervorming zich binnen het materiaal verdelen. De lokale spanningsconcentratie is nauw verbonden met vervorming en verschillende faalmechanismen. Een systematische verkenning van de anisotropie kan ons begrip van spanningsconcentratie en materiaalfalen verdiepen, en het ontwerpen van hoogwaardige materialen voor specifieke toepassingen begeleiden. Bovendien kan dit werk behulpzaam zijn voor duurzame ontwikkeling door de levensduur en recycleerbaarheid van metallische materialen te verbeteren. Dit is een steeds kritischer prioriteit in de materiaalkunde.

Anisotropie manifesteert zich op verschillende lengteschalen. De kleinste lengteschaal is die van de kristalstructuur. De regelmatige rangschikking van atomen in een kristal zorgt ervoor dat de elastische eigenschappen in verschillende richtingen variëren, zelfs in het zeer symmetrische kubische kristalsysteem. Wanneer blootgesteld aan externe spanning, ontstaan extra spanningsvelden nabij korrelgrenzen als gevolg van het verschil in de Young's modulus aan beide kanten van de korrelgrens, bekend als incompatibiliteitsspanning. In hoofdstuk 2 verken ik alle mogelijke korrelgrenzen in kubische kristalstructuren onder éénassige spanning. Door een decompositiemethode voor het roteren van de kristal elastische tensor te introduceren, worden expliciete uitdrukkingen voor incompatibiliteitsspanning afgeleid in termen van externe belasting, elastische eigenschappen en korreloriëntaties. Voor alle kubische kristallen ontstaat de hoogste incompatibiliteitsspanning wanneer een (100)//(111) korrelgrens loodrecht op de éénassige externe belasting staat. De incompatibiliteitsspanning is ongevoelig voor de rotatie rond de normaal van het grensvlak van een korrel relatief aan de andere korrel. Voor algemene korrelgrenzen is de incompatibiliteitsspanning evenredig aan het verschil in de reciproke van de Young's modulus aan de korrelgrens. In tegenstelling tot eerdere studies die zich richten op specifieke korrelgrenzen en metalen, biedt dit werk een bredere en meer systematische analyse van de spanningstoestand nabij korrelgrenzen.

Naast het oriëntatieverschil tussen kristallen aan weerszijden van de korrelgrens, beïnvloedt de oriëntatie van een korrelgrens ten opzichte van de toegepaste externe spanning ook de variatie in de incompatibiliteitsspanning. Daarom breidde ik het onderzoek naar incompatibiliteitsspanning uit naar korrelgrenzen met willekeurige inclinaties. Voor kubische kristallen wordt aangetoond dat de

incompatibiliteitsspanning uitsluitend voortkomt uit de deviatorische spannings-component van de spannings tensor. Door een gesimuleerde gloeiing (simulated annealing)-algoritme te gebruiken, onderzocht ik de relatie tussen de maximale incompatibiliteitsspanning bij korrelgrenzen en de inclinatiehoek voor materialen met verschillende graden van elastische anisotropie. Voor materialen met lage anisotropie vertonen korrelgrenzen loodrecht op een éénassige belasting de hoog-ste incompatibiliteitsspanning. Voor sterk anisotrope materialen, daarentegen, vertonen korrelgrenzen met inclinatiehoeken van 40 tot 50 graden de hoogste incompatibiliteitsspanning. Deze conclusie is van toepassing op alle materialen met kubische kristalstructuur, inclusief metalen, keramieken en intermetallische verbindingen.

Elastische anisotropie veroorzaakt een heterogeen spanningsveld in polycris-tallijne metallische materialen. Op de korrelschaal vertonen de mechanische ei-genschappen van metallische materialen met heterogene structuren aanzienlijke anisotropie vanwege hun structurele kenmerken. Hier onderzoek ik de anisotro-pie in de vloeigrens en plastische vervormingsmechanismen van perliet onder verschillende belastingcondities. Perliet bestaat uit ferriet en cementiet, die een regelmatige lamellaire microstructuur vormen. Door een periodiek bicrystal model te ontwikkelen voor perliet, wordt de relatie tussen de activeringsbarrière van de glijsystemen in de twee fasen en de belastingsrichting onthuld. In moleculaire dynamica simulates wordt de belasting conventioneel toegepast langs een van de hoofdassen van de simulatiecel. Ik ontdekte dat eerdere studies, die zich richtten op belastingsrichtingen die zijn uitgelijnd met de basisvectoren van de eenheidscel van cementiet, niet voldoende zijn om de anisotropie inherent aan perliet vervor-ming vast te leggen. Om deze beperking aan te pakken, ontwierp ik specifiek modellen met verschillende periodiciteiten. Daarom kan spanning in meerdere richtingen worden toegepast terwijl de atomistische configuraties identiek blijven. Deze aanpak onthult een significante afhankelijkheid van de belastingsrichting van de plastische vervorming van perliet. Met behulp van de nieuwe belastings-aanpak tonen simulates aan dat onder specifieke belastingcondities de glijband in cementiet kan worden geactiveerd bij een spanningsniveau lager dan dat van ferriet. Voor perlietkolonies met verschillende oriëntaties variëren de spanningen die overeenkomen met het begin van plastische vervorming sterk. Dit werk draagt bij aan een meer uitgebreide begrip van de vervormings- en versterkingsmechanis-men van perliet. Bovendien verduidelijkt het kwantitatief de effecten van factoren zoals de Schmid factor, grensvlak dislocaties en de volume fracties van de twee fasen op plastische vervorming van perliet. Verder biedt het richtlijnen voor het ontwerp van hoogwaardige materialen met lamellaire microstructuren die vaak worden gevonden als producten van eutectische of eutectoïde transformaties.

Metallische materialen met nanometer schaal poreuze structuren, zoals ge-

sinterde kopernanodeeltjes, vertonen aanzienlijk potentieel voor toepassingen in gebieden zoals elektronische verpakking. Hun poreuze structuur veroorzaakt anisotropie in macroscopische mechanische en andere fysieke eigenschappen. In hoofdstuk 5 gebruikte ik moleculaire dynamica simulaties om de spanningsgeïnduceerde sinterverdichting van kopernanodeeltjes en hun trekgedrag langs verschillende richtingen te bestuderen. In samenwerking met experimentele karakterisering worden twee parameters geïntroduceerd om de anisotropie van nanoscopische poreuze structuren te kwantificeren: de standaarddeviatie van de areale dichtheid en de oriëntatieverdeling van sinternekken. Het blijkt dat het toepassen van externe éénassige spanning tijdens het sinteren de dichtheidsvariatie langs de spanningsrichting vermindert, waarbij de sinternekken de neiging hebben om loodrecht op de toegepaste spanning uit te lijnen. Deze structurele kenmerken verbeteren de sterkte en taaiheid langs de sinterspanningsrichting vergeleken met andere oriëntaties. Dit werk biedt een methodologie voor het ontwerp en de prestatieoptimalisatie van poreuze gesinterde structuren.

Samenvattend begint dit onderzoek met het modelleren van de spanningsconcentratie bij korrelgrenzen onder éénassige spanning door middel van een bicrystal model, waarbij de voorwaarden voor maximale spanningsconcentratie voor alle kubische kristallen worden geïdentificeerd. Het breidt zich vervolgens uit naar korrelgrenzen die onder een hoek staan met de éénassige spanning en naar korrelgrenzen onder algemene externe belastingen. Daarbij is duidelijk geworden dat incompatibiliteitsspanning in sterk anisotrope materialen sterk afhankelijk is van de inclinatie van de korrelgrens. Op atomair niveau geven moleculaire dynamica simulaties inzicht in de vervorming van perliet. De uitgesproken anisotropie van de plasticiteit onder verschillende belastingcondities wordt onthuld. Voorbij de atomaire schaal wordt de anisotropie in de microstructuur en in de mechanische eigenschappen van gesinterde kopernanodeeltjes onderzocht door een combinatie van experimenten en simulaties. De spanningsverdeling, het plastisch gedrag en de microstructurele evolutie in polycristallijne metallische materialen vertonen anisotropie, wat de mechanische eigenschappen beïnvloedt. In bepaalde gevallen wordt de algehele eigenschappen van een materiaal beperkt door de laagst presterende regios. Een goed begrip van anisotropie kan het materiaalontwerp begeleiden om de nadelige effecten ervan te minimaliseren. Alternatief biedt het benutten van anisotropie de mogelijkheid om geavanceerde materialen te creëren met verbeterde prestaties in bepaalde richtingen.

1

1

INTRODUCTION

1

1.1 Background

Metals serve as the cornerstone of modern society, underpinning critical infrastructure and industries. Their unique combination of strength, ductility, and formability makes them indispensable for a wide range of applications, from pipelines and cables to automobiles and buildings. In the context of global challenges such as climate change and the transition toward sustainable development, advances in the metal industry are of paramount importance. The development of high-performance metallic materials, such as high-strength steels and lightweight, high-strength aluminum alloys, is essential to reduce material usage and vehicle weight, thus contributing to improved energy efficiency [1]. Improving properties of materials, such as creep resistance and corrosion resistance, can extend the lifespan of products, thereby amortizing manufacturing costs and environmental impacts. Recycling and reusing of metals bypasses energy-intensive ore reduction processes, significantly reducing pollution and carbon emissions, making it another critical area for development. The recycling and reuse of metals also demand a deep understanding of the relationship between microstructure and mechanical properties. For example, designing processes to control impurity distribution is critical for metal recycling.

Metallic materials exhibit anisotropy at different scales, and the anisotropy at each scale influences the properties at higher scales. Some aspects of anisotropy, such as texture, have been extensively studied, while others, such as the relationship between stress fields near grain boundaries (GBs) and crystallographic anisotropy, have received less attention. Research on the general anisotropy of metallic materials requires integrated multiscale computational approaches. Therefore, this work is not limited to specific methods or material systems but aims to broadly reveal the sources and effects of anisotropy across multiple scales.

This work provides a perspective on the relationship between the mechanical properties of metals and their microstructures, highlighting the origins and impacts of anisotropy at various spatial scales, and discussing computational and simulation methods to better guide experimental design and performance optimization.

1.2 Anisotropy in mechanical properties of metallic materials

Polycrystalline metals are often treated as isotropic materials, characterized by a single set of averaged mechanical properties such as elastic modulus, Poisson's ratio, and yield strength. However, macroscopic mechanical properties can exhibit significant anisotropy, which can compromise performance or be leveraged to advantage. Fig. 1.1 illustrates anisotropy in metallic materials on different length scales, originating from the following key factors:

1. Intrinsic Crystal Structure Anisotropy: Atomic arrangements in crystals lead

to orientation-dependent mechanical properties, as shown in Fig. 1.1(a). In single crystals or textured materials, properties like elastic modulus, strength, and phase transformation exhibit pronounced directional dependence.

2. Directional Distribution of Grains and Defects: Manufacturing processes such as rolling and wire-drawing, can align GBs, dislocations, and precipitates. Fig. 1.1(b) shows the non-uniform microstructure of an Ag-Cu alloy prepared by selective laser melting, where controlled grain morphology results in anisotropic strength and ductility.

3. Heterogeneous Microstructures: Alloys may develop anisotropic microstructures through processes like eutectoid transformation or spinodal decomposition. For example, Fig. 1.1(c) shows the lamellar structure of pearlite. The low symmetry microstructure of pearlite leads to anisotropic mechanical behavior.

4. Pore Distribution in Porous Materials: In porous materials, the distribution, shape, and orientation of pores and necks significantly influence mechanical properties, conductivity, and gas permeability. Sintered or foamed metals, for instance, exhibit directional variations in stiffness, strength, and fracture behavior due to anisotropic pore and neck arrangements.

5. Residual Stresses and Surface Effects: Processing-induced residual stresses (e.g., from welding, machining, or heat treatment) create localized anisotropy. Surface effects, particularly in nanostructured or thin-film materials, further contribute as a result of high surface-to-volume ratios and surface energy influences.

1

(a)

(b)

(c)

(d)
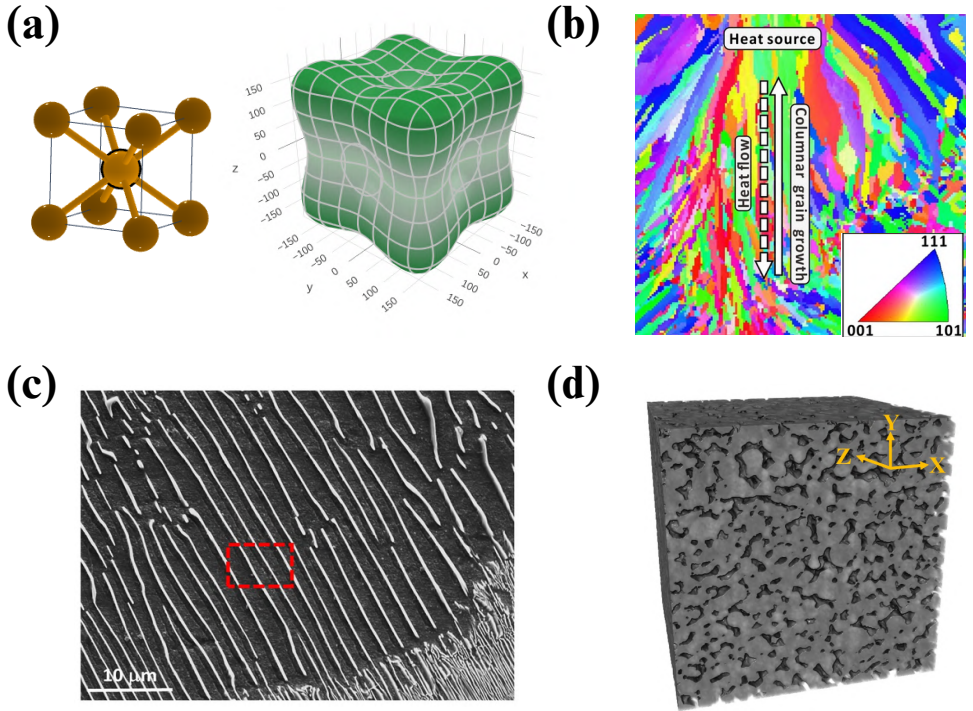
Figure 1.1: The figure illustrates the anisotropy in metallic materials at four different scales. (a) The anisotropy in the spatial distribution of Young's modulus for BCC-structured iron [2].(b) The microstructure of an Ag-Cu alloy produced by selective laser sintering, where colors represent different grain orientations [3]. Both grain shapes and orientation distributions exhibit anisotropy.(c) Pearlite with a lamellar structure [4], where the black regions represent ferrite and the white regions represent cementite.(d) A porous Cu structure formed by the sintering of nanoparticles [5]. The non-uniform distribution of pores and Cu particles in the structure lead to anisotropy in mechanical properties.

1.3 Elastic anisotropy in crystalline metals

The Zener ratio is the simplest metric for anisotropy quantification in cubic crystals [6]:

$$A = \frac{2C_{44}}{C_{11} - C_{12}},\tag{1.1}$$

where C_{11}, C_{12}, and C_{44} are the three elastic components for cubic crystals. Physically, the Zener ratio represents the ratio in the resistance to two types of shear deformations. $\frac{C_{11}-C_{12}}{2}$ is for shear resistance along $(110)[1\bar{1}0]$, while C_{44} is for shear resistance along $(100)[010]$. For an isotropic crystal, $A = 1$.

Chung and Buessem [7] proposed an empirical measurement of anisotropy for cubic material:

$$A^C = \frac{G^V - G^R}{G^V + G^R} = \frac{3(A-1)^2}{3(A-1)^2 + 25A},\tag{1.2}$$

where A is the Zener ratio, G^V and G^R are averaged polycrystalline shear moduli calculated using the Voigt and Reuss schemes, respectively, as

$$G^V = \frac{C_{11} - C_{12} + 3C_{44}}{5}$$

$$G^R = \frac{5(C_{11} - C_{12})C_{44}}{4C_{44} + 3(C_{11} - C_{12})}.$$

Theoretically, G^V provides an upper bound estimate of the shear modulus for polycrystalline materials, while G^R gives the lower bound estimate. The parameter A^C quantifies the difference between these two shear moduli. For an isotropic crystal, $A^C = 0$. However, this method is limited to cubic crystals, as it only considers the three independent elastic constants.

Shivakumar et al. [8] introduced a universal elastic anisotropy index, which quantifies anisotropy for all crystal structures. The averaged stiffness tensor $\langle \mathbf{C}^d \rangle$ and compliance tensor $\langle \mathbf{S}^t \rangle$ for a crystal are given by:

$$\mathbf{C}^V = \langle \mathbf{C}^d \rangle = 2G^V \mathbf{K} + 3K^V \mathbf{J},$$
$$\mathbf{S}^R = \langle \mathbf{S}^t \rangle = \frac{1}{2G^R}\mathbf{K} + \frac{1}{3K^R}\mathbf{J},\tag{1.3}$$

where the superscripts d and t indicate displacement and traction boundary conditions, respectively. The superscripts V and R denote the Voigt and Reuss averages. $\mathbf{K}$ and $\mathbf{J}$ are the deviatoric and spherical projection tensors of rank four, respectively. For a perfectly isotropic crystal, it holds that $\mathbf{C}^V = (\mathbf{S}^R)^{-1}$ and:

$$\sum_{i=1}^{6} \sum_{j=1}^{6} C_{ij}^V S_{ij}^R = 6.$$

Therefore, the universal anisotropy index A^U is defined as:

$$A^U = \sum_{i=1}^{6} \sum_{j=1}^{6} C_{ij}^V S_{ij}^R - 6 = 5\frac{G^V}{G^R} + \frac{K^V}{K^R} - 6 \geq 0. \tag{1.4}$$

Since all elastic components are included in the evaluation, A^U is expected to be applicable to all crystal structures.

For medium-entropy alloys and high-entropy alloys, the anisotropy in elastic properties becomes significantly more complex. This anisotropy is primarily influenced by the proportion of each constituent element in the alloy [9, 10]. Additionally, local ordering of atoms can further alter the elastic properties. For instance, in the case of the CrCoNi ternary medium-entropy alloy (with an FCC lattice), studies have shown that its $C_{11} - C_{12}$ values range between 43 and 223 GPa, while its C_{44} values range between 50 and 110 GPa [11]. This corresponds to Zener ratios ranging from 0.5 to 5, highlighting the significant variability in anisotropy. Such richness in elastic anisotropy offers promising opportunities to tailor material properties in advanced material design.

1.4 Grain boundary characteristics and modeling methods

The degrees of freedom (DOF) of a GB describe the independent parameters required to fully characterize its geometric and crystallographic configuration. In polycrystalline materials, GBs are interfaces between adjacent crystallites (grains) with different crystallographic orientations. The DOFs of GBs are typically defined by five parameters [12]:

1. Three rotational DOFs: These describe the misorientation between the two grains, expressed as three angular parameters (e.g., Euler angles or axis-angle representation).

2. Two translational DOFs: These define the orientation of the boundary plane. This orientation can be specified using Miller indices $[hkl]$ relative to the crystallographic reference frame of one of the grains. Alternatively, the boundary-plane orientation can be expressed with two Euler rotation angles.

These five parameters capture the essential crystallographic and geometric features of GBs.

When the atomic structure at GBs is analyzed, additional DOFs must be considered, such as atomic relaxation, chemical composition and segregation, and the presence of other defects. Regarding atomic relaxation, Tschopp et al. [13] developed an algorithm to construct stable GB structures. In this method, rigid-body

translations are applied to one lattice relative to the other along two directions within the GB plane. Overlapping atoms are removed, and the system undergoes energy minimization to reach a stable configuration. This approach introduces four additional microscopic DOFs to fully describe the GB structure.

The global coordinate system is represented in the local crystal coordinate system by normalized Miller indices. Taking the components of the global X, Y, and Z directions in the local coordinate system as column vectors, the orientation matrix can be constructed. For two grains with known orientation matrices, g_1 and g_2, a rotation matrix R is defined as

$$R = g_2 \cdot g_1^{-1}. \tag{1.5}$$

The rotation defined by R is equivalent to rotation around axis $u = (u_1, u_2, u_3)$ by angle θ, where

$$\theta = \cos^{-1}\left(\frac{tr(R) - 1}{2}\right), \tag{1.6}$$

and

$$u_1 = \frac{R_{32} - R_{23}}{2\sin\theta}, u_2 = \frac{R_{13} - R_{31}}{2\sin\theta}, u_3 = \frac{R_{21} - R_{12}}{2\sin\theta}. \tag{1.7}$$

The Coincident Site Lattice (CSL) theory describes the periodic overlap of lattice points from two adjacent crystal grains [14]. In this framework, a GB is characterized by an index Σn, where $\frac{1}{n}$ represents the fraction of coincident atomic sites between the two grains. Such a boundary is referred to as a Σn GB. Grain boundaries with $n \leq 29$ are generally classified as low-Σ GBs, as they exhibit a higher degree of coincidence and are often associated with lower interfacial energy and special properties.

For grain boundaries with a known rotation axis u and rotation angle θ, the CSL index is typically determined using a CSL table (see, e.g., [15]). Brandon [16] proposed that grain boundaries with moderate deviations in u and θ should also be distinguished from general high-angle GBs. The permissible angular deviation $\Delta\theta$ for a given n is defined as:

$$\Delta\theta = \theta_0 n^{-\frac{1}{2}}, \tag{1.8}$$

where $\theta_0 = 15^\circ$. The concept of extended low-Σ GB is widely adopted, and alternative formulations for permissible deviations have been proposed also, as discussed in [17].

Modern tools are now available for CSL analysis, significantly simplifying the process of studying GBs. For example, the open-source software AimsGB [18] has been developed to generate periodic grain boundaries with a specified Σ value and rotation axis. MTEX [19], a MATLAB-based toolbox for crystallographic analysis, also provides tools to calculate CSL relationships and analyze grain boundaries.

1

When considering the atomic structure of GBs, the dislocation model is used to study low-angle grain boundaries, where the misorientation is attributed to periodically arranged dislocations [20, 21]. The structural unit model (SUM) has been proposed for high-angle GBs [22–24]. GB structures are described as a combination of building blocks or structural units in two dimensions. This model effectively captures the continuous structural evolution of tilt grain boundaries as the tilt angle changes. However, the existence of metastable GB states and other GB behaviors (such as GB sliding and the absorption/emission of dislocations) make the prediction of GB structures still challenging. Jian Han et al. [25] employed molecular dynamics simulations to investigate structural units and their evolution in metastable GBs. The study also proposed a method to predict the structure and energy of GBs with specific misorientations based on structural units.

Advances in computational resources and atomic simulation techniques now enable the use of more complex and higher-dimensional data to describe local atomic structures, marking a shift from physics-based descriptors to data-based descriptors. Examples of such descriptors include the Smooth Overlap of Atomic Positions (SOAP) [26, 27], Atom-centered Symmetry Functions (ACSF) [28], Atomic Cluster Expansion (ACE) [29], and Many-body Tensor Representation [30]. These descriptors provide powerful tools for the quantitative characterization of GBs.

Taking SOAP as an example, SOAP is a descriptor that encodes regions of atomic geometries by expanding a Gaussian-smeared atomic density using orthonormal functions based on spherical harmonics and radial basis functions. A common implementation of SOAP is provided in [31]. Fujii et al. [32] utilized SOAP to investigate the relationship between thermal conductivity and the structure of various MgO grain boundaries. Using SOAP to quantitatively compare the similarity of atomic environments, the study classified over a thousand atoms in the grain boundaries into six categories: highly under-coordinated, moderately under-coordinated, strongly strained, moderately strained, and others. The relationship between atomic environment and thermal conductivity was established using linear regression, which demonstrated strong predictive accuracy for new GBs. Owens et al. [33] compared a variety of descriptors for grain boundaries (such as centrosymmetry parameter [34], common neighbor analysis [35], ACE, SOAP, ACSF, and graph description), and systematic examined the performance of each descriptor in predicting grain boundary energies.

Since GBs exhibit phase-like behavior as their structure and properties may change discontinuously at critical values of thermodynamic parameters, GBs can be treated as thermodynamically stable interfacial states, referred as GB complexions [36, 37]. These complexions are characterized by unique atomic structures, chemical compositions, and properties. They can significantly influence the behavior of materials.

1.5 HETEROGENEOUS MICROSTRUCTURES IN METALLIC MATERIALS

Heterogeneous microstructures in metallic materials originate from two primary sources. The first is phase-transformation-driven spontaneous formation, such as resulting from eutectic reaction [38] and spinodal decomposition [39]. The second is artificially engineered heterogeneous structures, which are fabricated using advanced manufacturing techniques, including additive manufacturing [40], powder metallurgy [41], and rolling [42].

Heterogeneous microstructures encompass a variety of configurations, such as gradient grain structures [43–45], lamellar structures [38, 42, 46], core-shell structures [41, 47, 48] (also referred to as harmonic structures [49]), and interwoven nanophases [39, 50]. A comprehensive overview of these structures can be found in [51].

The deformation behavior of heterogeneous materials is more complex than that of homogeneous materials due to differences in elastic properties, yield strength, and work hardening capabilities among their constituent regions. For instance, in core-shell structures, studies [49, 52, 53] have shown that plastic deformation usually begins in the core region, which typically has larger grains and lower strength. As deformation progresses, the core-shell interface impedes further plastic deformation, leading to the generation of a high density of geometrically necessary dislocations near the interface. This results in back stress acting on the core region, enhancing both the overall strength and work-hardening. Such mechanisms effectively suppress plastic instability and improve ductility.

Eutectic reactions offer a versatile pathway for generating diverse heterogeneous microstructures. Extensive research has been conducted on eutectic alloys in aluminum-based, titanium-based, nickel-based, and high-entropy alloy systems, as reviewed in [54, 55]. Eutectic reactions refine grain size and enable coordinated deformation through hierarchical microstructures, thereby enhancing yield strength and fracture toughness. A notable example is pearlite, which forms through a eutectic reaction from austenite and consists of a hard, brittle cementite phase and a softer ferrite phase. The fine lamellar structure in pearlite imparts excellent plastic deformability. After severe deformation, the decomposition of cementite induces additional solid solution strengthening and dislocation strengthening [56, 57]. The ultimate strength for deformed pearlite can be up to 7 GPa [58].

Metallic materials with porous structures exhibit unique properties, such as low modulus, low density, and high surface-to-volume ratios. These characteristics make porous structures particularly suitable for applications in medical fields [59, 60]. However, in certain materials prepared by sintering, due to process limitations such as restricted sintering duration and relatively low sintering

temperatures, porous structures may be unintentionally introduced [61–63]. For example, sintering of nanoparticles is widely used to connect chips and substrates in electronic packaging. The resulting interconnecting layer often exhibits a porous structure. Numerous studies have investigated the relationships between critical parameters of porous sintered structures, such as porous sintered structures, such as relative density and pore size, and their corresponding mechanical properties [64–66].

Despite significant progress, the design of heterogeneous structures remains largely empirical. The multiscale nature of their internal structures presents challenges for modeling and simulation. Advanced characterization techniques, robust mechanical theories, and multiscale simulation methods are essential to elucidate the strengthening mechanisms of heterogeneous structures. These tools can guide the design and fabrication of heterogeneous materials with unprecedented mechanical properties, paving the way for future innovations in materials science.

1.6 Outline of the thesis

This work explores the heterogeneity in the structure and properties of metallic materials on multiple scales. The spatial scales, sources of anisotropy, and corresponding material systems addressed in each chapter are summarized in Table 1.1.

Chapter	Scale	Anisotropy source	Effects	System
2	crystal	elastic tensor	incompatibility stress near GBs	cubic crystals
3	grain	GB inclination	incompatibility stress near GBs	cubic crystals
4	multiphase domain	heterogeneous microstructure	anisotropy in plastic deformation	pearlite
5	porous bulk	porous structure	anisotropy in mechanical properties	sintered Cu nanoparticles

Table 1.1: The outline of each chapter in this thesis.

Chapter 2 introduces a bicrystal model to investigate grain boundaries in metals with cubic crystal structures. External stress is applied perpendicular to the grain boundary plane, and the maximum additional stress arising from elastic incompatibility near the grain boundary is derived analytically. Under uniaxial stress, the largest incompatibility stress in cubic materials occurs when the two

1

grains are oriented along the loading axis as $< 111 >$ and $< 100 >$, respectively. Surprisingly, the incompatibility stress is very insensitive to the in-plane rotation. Furthermore, for general bicrystals, the magnitude of the incompatibility stress is correlated with the difference of the Young's modulus of the two grains along the loading direction.

In Chapter 3, the incompatibility stresses for GBs with arbitrary inclinations are analyzed with the bicrystal model. The effects of elastic anisotropy and the inclination angle of the grain boundary relative to the external stress direction are systematically examined for metals with varying degrees of elastic anisotropy.

Chapter 4 applies the analytical model presented in Chapter 3 to pearlite with the Bagaryatskii orientation relationship. Using supercells with various periodicities, the plasticity behavior of pearlite is simulated with molecular dynamics. A range of loading conditions that were not explored in previous studies are investigated. The influence of interface dislocations, cementite-ferrite volume ratio, and loading directions on the plastic deformation behavior of pearlite is discussed.

Chapter 5 focuses on sintered copper nanoparticles for electronic packaging applications, where the heterogeneous structure significantly influences their mechanical properties. Molecular dynamics simulations reveal the evolution of the porous structure during stress-assisted sintering. By analyzing variations in areal relative density and the orientation distribution of sintering necks, the anisotropic mechanical properties of sintered copper nanoparticles are elucidated.

Chapter 6 provides a summary of the study of anisotropy in both crystal elasticity and macroscopic mechanical properties. The importance and prevalence of anisotropy are discussed and potential directions for further research are outlined.

References

[1] Dierk Raabe. The materials science behind sustainable metals and alloys. *Chemical reviews*, 123(5):2436–2608, 2023.

[2] Romain Gaillac, Pluton Pullumbi, and François-Xavier Coudert. ELATE: an open-source online application for analysis and visualization of elastic tensors. *Journal of Physics: Condensed Matter*, 28(27):275201, 2016.

[3] Wei Xiong, Liang Hao, Ton Peijs, Chunze Yan, Kaka Cheng, Ping Gong, Qian Cui, Danna Tang, Shamoon Al Islam, and Yan Li. Simultaneous strength and ductility enhancements of high thermal conductive Ag7.5Cu alloy by selective laser melting. *Scientific Reports*, 12(1):4250, 2022.

[4] MI Khan, HK Mehtani, A Durgaprasad, GK Goyal, MJNV Prasad, S Parida, T Dasgupta, Nick Birbilis, and I Samajdar. The defining role of interface

1

crystallography in corrosion of a two-phase pearlitic steel. *Philosophical Magazine*, 100(11):1439–1453, 2020.

[5] Leiming Du, Kai Liu, Dong Hu, Olof Bäcke, Xiao Hu, Xinrui Ji, Jiajie Fan, René H Poelma, Magnus Hörnqvist Colliander, and Guoqi Zhang. Microstructural and mechanical anisotropy in pressure-assisted sintered copper nanoparticles. *Acta Materialia*, page 120772, 2025.

[6] Clarence M Zener and Sidney Siegel. Elasticity and anelasticity of metals. *The Journal of Physical Chemistry*, 53(9):1468–1468, 1949.

[7] DH Chung and WR Buessem. The elastic anisotropy of crystals. *Journal of Applied Physics*, 38(5):2010–2012, 1967.

[8] Shivakumar I Ranganathan and Martin Ostoja-Starzewski. Universal elastic anisotropy index. *Physical review letters*, 101(5):055504, 2008.

[9] Stephan Schönecker, Xiaojie Li, Daixiu Wei, Shogo Nozaki, Hidemi Kato, Levente Vitos, and Xiaoqing Li. Harnessing elastic anisotropy to achieve low-modulus refractory high-entropy alloys for biomedical applications. *Materials & design*, 215:110430, 2022.

[10] Hualei Zhang, Xun Sun, Song Lu, Zhihua Dong, Xiangdong Ding, Yunzhi Wang, and Levente Vitos. Elastic properties of Al_xCrMnFeCoNi ($0 \leq x \leq 5$) high-entropy alloys from ab initio theory. *Acta Materialia*, 155:12–22, 2018.

[11] Qing-Jie Li, Howard Sheng, and Evan Ma. Strengthening in multi-principal element alloys with local-chemical-order roughened dislocation pathways. *Nature communications*, 10(1):3563, 2019.

[12] Gregory S Rohrer, David M Saylor, Bassem El Dasher, Brent L Adams, Anthony D Rollett, and Paul Wynblatt. The distribution of internal interfaces in polycrystals. *International Journal of Materials Research*, 95(4):197–214, 2021.

[13] Mark A Tschopp, Shawn P Coleman, and David L McDowell. Symmetric and asymmetric tilt grain boundary structure and energy in Cu and Al (and transferability to other fcc metals). *Integrating Materials and Manufacturing Innovation*, 4:176–189, 2015.

[14] OBM Hardouin Duparc. A review of some elements in the history of grain boundaries, centered on georges friedel, the coincident 'site'lattice and the twin index. *Journal of materials science*, 46:4116–4134, 2011.

1

[15] H Grimmer, WT Bollmann, and DH Warrington. Coincidence-site lattices and complete pattern-shift in cubic crystals. *Acta Crystallographica Section A: Crystal Physics, Diffraction, Theoretical and General Crystallography*, 30(2):197–207, 1974.

[16] DG Brandon. The structure of high-angle grain boundaries. *Acta metallurgica*, 14(11):1479–1484, 1966.

[17] Stuart I Wright. Investigation of coincident site lattice boundary criteria in Cu thin films. *Journal of electronic materials*, 31:50–54, 2002.

[18] Jianli Cheng, Jian Luo, and Kesong Yang. Aimsgb: An algorithm and open-source python library to generate periodic grain boundary structures. *Computational Materials Science*, 155:92–103, 2018.

[19] F Bachmann, Ralf Hielscher, and Helmut Schaeben. Texture analysis with MTEX–free and open source software toolbox. *Solid state phenomena*, 160:63–68, 2010.

[20] William T Read and WJPR Shockley. Dislocation models of crystal grain boundaries. *Physical review*, 78(3):275, 1950.

[21] W Shockley and WT Read. Quantitative predictions from dislocation models of crystal grain boundaries. *Physical Review*, 75(4):692, 1949.

[22] G Ho Bishop and Bo Chalmers. A coincidence—ledge—dislocation description of grain boundaries. *Scripta Metallurgica*, 2(2):133–139, 1968.

[23] Adrian Peter Sutton and V Vitek. On the structure of tilt grain boundaries in cubic metals I. Symmetrical tilt boundaries. *Philosophical Transactions of the Royal Society of London. Series A, Mathematical and Physical Sciences*, 309(1506):1–36, 1983.

[24] AA Nazarov, OA Shenderova, and DW Brenner. On the disclination-structural unit model of grain boundaries. *Materials Science and Engineering: A*, 281(1-2):148–155, 2000.

[25] Jian Han, Vaclav Vitek, and David J Srolovitz. The grain-boundary structural unit model redux. *Acta Materialia*, 133:186–199, 2017.

[26] Albert P Bartók, Risi Kondor, and Gábor Csányi. On representing chemical environments. *Physical Review B—Condensed Matter and Materials Physics*, 87(18):184115, 2013.

[27] James P Darby, James R Kermode, and Gábor Csányi. Compressing local atomic neighbourhood descriptors. *npj Computational Materials*, 8(1):166, 2022.

[28] Jörg Behler. Atom-centered symmetry functions for constructing high-dimensional neural network potentials. *The Journal of chemical physics*, 134(7), 2011.

[29] Ralf Drautz. Atomic cluster expansion for accurate and transferable inter-atomic potentials. *Physical Review B*, 99(1):014104, 2019.

[30] Haoyan Huo and Matthias Rupp. Unified representation of molecules and crystals for machine learning. *Machine Learning: Science and Technology*, 3(4):045017, 2022.

[31] Lauri Himanen, Marc O. J. Jäger, Eiaki V. Morooka, Filippo Federici Canova, Yashasvi S. Ranawat, David Z. Gao, Patrick Rinke, and Adam S. Foster. DScribe: Library of descriptors for machine learning in materials science. *Computer Physics Communications*, 247:106949, 2020.

[32] Susumu Fujii, Tatsuya Yokoi, Craig AJ Fisher, Hiroki Moriwake, and Masato Yoshiya. Quantitative prediction of grain boundary thermal conductivities from local atomic environments. *Nature communications*, 11(1):1854, 2020.

[33] C Braxton Owens, Nithin Mathew, Tyce W Olaveson, Jacob P Tavenner, Edward M Kober, Garritt J Tucker, Gus LW Hart, and Eric R Homer. Feature engineering descriptors, transforms, and machine learning for grain boundaries and variable-sized atom clusters. *npj Computational Materials*, 11(1):21, 2025.

[34] Cynthia L Kelchner, SJ Plimpton, and JC Hamilton. Dislocation nucleation and defect structure during surface indentation. *Physical review B*, 58(17):11085, 1998.

[35] J Dana Honeycutt and Hans C Andersen. Molecular dynamics study of melting and freezing of small Lennard-Jones clusters. *Journal of Physical Chemistry*, 91(19):4950–4963, 1987.

[36] Shen J Dillon, Ming Tang, W Craig Carter, and Martin P Harmer. Complexion: a new concept for kinetic engineering in materials science. *Acta Materialia*, 55(18):6208–6218, 2007.

[37] Patrick R Cantwell, Ming Tang, Shen J Dillon, Jian Luo, Gregory S Rohrer, and Martin P Harmer. Grain boundary complexions. *Acta Materialia*, 62:1–48, 2014.

[38] Christine Borchers and Reiner Kirchheim. Cold-drawn pearlitic steel wires. *Progress in Materials Science*, 82:405–444, 2016.

[39] Huai Guan, Hui Xie, Zhao-Ping Luo, Wei-Kang Bao, Ze-Sheng You, Zhaohui Jin, and Hai-Jun Jin. Ultrastrong spinodoid alloys enabled by electrochemical dealloying and refilling. *Proceedings of the National Academy of Sciences*, 120(1):e2214773120, 2023.

[40] Haoxiu Chen, Yixiao He, Soumya Sobhan Dash, and Yu Zou. Additive manufacturing of metals and alloys to achieve heterogeneous microstructures for exceptional mechanical properties. *Materials Research Letters*, 12(3):149–171, 2024.

[41] Zhe Zhang, Sanjay Kumar Vajpai, Dmitry Orlov, and Kei Ameyama. Improvement of mechanical properties in SUS304L steel through the control of bimodal microstructure characteristics. *Materials Science and Engineering: A*, 598:106–113, 2014.

[42] Xiaolong Ma, Chongxiang Huang, Jordan Moering, Mathis Ruppert, Heinz Werner Höppel, Mathias Göken, Jagdish Narayan, and Yuntian Zhu. Mechanical properties of copper/bronze laminates: role of interfaces. *Acta Materialia*, 116:43–52, 2016.

[43] XiaoLei Wu, Ping Jiang, Liu Chen, Fuping Yuan, and Yuntian Zhu. Extraordinary strain hardening by gradient structure. In *Heterostructured Materials*, pages 53–71. Jenny Stanford Publishing, 2021.

[44] K Lu. Making strong nanomaterials ductile with gradients. *Science*, 345(6203):1455–1456, 2014.

[45] Xiaoyan Li, Lei Lu, Jianguo Li, Xuan Zhang, and Huajian Gao. Mechanical properties and deformation mechanisms of gradient nanostructured metals and alloys. *Nature Reviews Materials*, 5(9):706–723, 2020.

[46] PJ Maziasz and CT Liu. Development of ultrafine lamellar structures in two-phase γ-TiAl alloys. *Metallurgical and Materials Transactions A*, 29:105–117, 1998.

[47] Qian Zhang, Zehao Chen, Yong Dong, Chuanqiang Li, and Yu Wang. High strength and ductility eutectic high entropy alloy with unique core-shell structure. *Journal of Alloys and Compounds*, 976:173141, 2024.

[48] Xuezheng Zhang, Yao He, Tijun Chen, Guangli Bi, Yuandong Li, Dan Tang, and Xiaoming Wang. Coordinating the deformation of a low-alloyed magnesium

1

alloy for a superior combination of strength and ductility through core-shell structured reinforcements. *Acta Materialia*, 281:120365, 2024.

[49] Kei Ameyama, Fabien Cazes, Hervé Couque, Guy Dirras, Shoichi Kikuchi, Jia Li, Frédéric Mompiou, K Mondal, Dmytro Orlov, Bhupendra Sharma, et al. Harmonic structure, a promising microstructure design. *Materials Research Letters*, 10(7):440–471, 2022.

[50] Huai Guan, Hui Xie, Cui-Hong Li, and Hai-Jun Jin. Thermally induced reaction and transient hardening of miscible spinodoid alloys. *Acta Materialia*, 265:119611, 2024.

[51] Swantje Bargmann, Benjamin Klusemann, Jürgen Markmann, Jan Eike Schnabel, Konrad Schneider, Celal Soyarslan, and Jana Wilmers. Generation of 3D representative volume elements for heterogeneous materials: A review. *Progress in Materials Science*, 96:322–384, 2018.

[52] Jianguo Li, Qian Zhang, Ruirui Huang, Xiaoyan Li, and Huajian Gao. Towards understanding the structure–property relationships of heterogeneous-structured materials. *Scripta Materialia*, 186:304–311, 2020.

[53] Jiaxi Jiang, Zekun Chen, Huachun Ma, Hanzheng Xing, and Xiaoyan Li. Strength-ductility synergy in heterogeneous-structured metals and alloys. *Matter*, 5(8):2430–2433, 2022.

[54] Isaac Chang and Qing Cai. From simple binary to complex multicomponent eutectic alloys. *Progress in Materials Science*, 123:100779, 2022.

[55] Chandra Sekhar Tiwary, Prafull Pandey, Suman Sarkar, Rakesh Das, Sumanta Samal, Krishanu Biswas, and Kamanio Chattopadhyay. Five decades of research on the development of eutectic as engineering materials. *Progress in Materials Science*, 123:100793, 2022.

[56] Xiaodan Zhang, Andy Godfrey, Xiaoxu Huang, Niels Hansen, and Qing Liu. Microstructure and strengthening mechanisms in cold-drawn pearlitic steel wire. *Acta Materialia*, 59(9):3422–3430, 2011.

[57] P-Y Tung, Xuyang Zhou, David Mayweg, Lutz Morsdorf, and Michael Herbig. Under-stoichiometric cementite in decomposing binary Fe-C pearlite exposed to rolling contact fatigue. *Acta Materialia*, 216:117144, 2021.

[58] Yujiao Li, Dierk Raabe, Michael Herbig, Pyuck-Pa Choi, Shoji Goto, Aleksander Kostka, Hiroshi Yarita, Christine Borchers, and Reiner Kirchheim. Segregation

stabilizes nanocrystalline bulk steel with near theoretical strength. *Physical review letters*, 113(10):106104, 2014.

[59] Ruben Wauthle, Seyed Mohammad Ahmadi, Saber Amin Yavari, Michiel Mulier, Amir Abbas Zadpoor, Harrie Weinans, Jan Van Humbeeck, Jean-Pierre Kruth, and Jan Schrooten. Revival of pure titanium for dynamically loaded porous implants using additive manufacturing. *Materials Science and Engineering: C*, 54:94–100, 2015.

[60] Chunze Yan, Liang Hao, Ahmed Hussein, and Philippe Young. Ti–6Al–4V triply periodic minimal surface structures for bone implants fabricated via selective laser melting. *Journal of the mechanical behavior of biomedical materials*, 51:61–73, 2015.

[61] Li Yin, Fan Yang, Xin Bao, Wenhua Xue, Zhipeng Du, Xinyu Wang, Jinxuan Cheng, Hongjun Ji, Jiehe Sui, Xingjun Liu, et al. Low-temperature sintering of Ag nanoparticles for high-performance thermoelectric module design. *Nature Energy*, 8(7):665–674, 2023.

[62] Yujian Wang, Dou Xu, Haidong Yan, Cai-Fu Li, Chuantong Chen, and Wanli Li. Low-temperature copper sinter-joining technology for power electronics packaging: A review. *Journal of Materials Processing Technology*, page 118526, 2024.

[63] Waqas Saeed, Zhongyu Liu, Rubin Yan, Yuejun Li, Hongsheng Xu, Ye Tian, Xing Chen, and Wei Liu. Nanostructured compliant interconnections for advanced micro-electronic packaging. *Materials & Design*, page 113166, 2024.

[64] Prasanta Jana, Sumit Ray, Diya Goldar, Navya Kota, Sujoy Kumar Kar, and Siddhartha Roy. Study of the elastic properties of porous copper fabricated via the lost carbonate sintering process. *Materials Science and Engineering: A*, 836:142713, 2022.

[65] Jiajie Fan, Dawei Jiang, Hao Zhang, Dong Hu, Xu Liu, Xuejun Fan, and Guoqi Zhang. High-temperature nanoindentation characterization of sintered nano-copper particles used in high power electronics packaging. *Results in Physics*, 33:105168, 2022.

[66] Wenwu Zhang, Penghao Zhang, Dashi Lu, Hao Pan, Xiangli Liu, Chengyan Xu, Jun Wei, Mingyu Li, and Hongjun Ji. A supersaturated Cu-Ag nanoalloy joint with ultrahigh shear strength and ultrafine nanoprecipitates for power electronic packaging. *Journal of Materials Science & Technology*, 145:56–65, 2023.

2

INCOMPATIBILITY STRESS AT GRAIN BOUNDARIES UNDER UNIAXIAL LOADING

The contents of this chapter have been published as a journal paper: Kai Liu, Marcel HF Sluiter. "Stresses at grain boundaries: The maximum incompatibility stress in an infinitely extended elastic bicrystal under uniaxial loading." Scripta Materialia 234 (2023): 115570.

2

2.1 Abstract

In a material under stress, grain boundaries may give rise to stress discontinuities. Stress localization is crucial to materials' behavior such as segregation, precipitation, and void nucleation. Here, the stress state at a grain boundary perpendicular to a uniaxial external stress is studied systematically. The grain boundary with the most extreme stress discontinuity is determined for cubic materials within the elastic limit for a bicrystal model. Additionally, grain boundaries with negligible stress discontinuity are identified. The influence of the elastic tensor components, C_{11}, C_{12}, and C_{44}, and grain orientation is studied quantitatively.

2.2 Introduction

Grain boundaries (GBs) act as walls that divide the bulk into parts with different orientations and discontinuous tensorial properties. Under loading, the misorientation of grains and the intrinsic anisotropy of the crystal lead to a stress discontinuity at the GBs, resulting in stress states that deviate significantly from the average. The stress discontinuity at GBs strongly influences some phenomena at the grain scale, such as grain growth [1, 2] and segregation [3]. Moreover, since the failure of materials is controlled by extreme values of localized stresses rather than by the average stress level in the material, the stress discontinuity at certain GBs strongly affects materials' mechanical behavior, such as crack initiation under loading [4], fatigue [5–7], corrosion cracking [8], and creep [9–11]. Grain boundary engineering [12] and new manufacturing methods show great promise for optimizing material performance through control of texture [13, 14] and GB structure [15]. Therefore, investigating how stress states at GBs are influenced by grain orientations can help design polycrystalline materials with optimized textures [16].

Theoretically, already three decades ago, certain special GBs, such as the tilt symmetrical GB and twist GB [17–19], were studied and analytic solutions for those particular incompatibility stresses (IS) were derived. A few years ago, for bicrystals, an explicit closed-form solution for IS for general GBs was derived and verified through finite element method (FEM) simulations [20]. This solution was then applied to study the stress state at $\Sigma 3 \langle 1\ 1\ 1 \rangle$ twin boundaries[21] and the activation of dislocations in nickel bicrystalline micropillars[22]. It was revealed that IS plays a crucial role in activating slip, which directly affects the plastic deformation of metals. For polycrystals, FEM simulations and statistical analysis have shown that the inclination angle of grain boundaries, grain size, and triple junctions have a significant influence on IS [23–26].

In addition to IS at GBs, there are several theoretical studies on the interaction of dislocations with GBs. The elastic field induced by dislocations [27] and the dislocation pile-ups behavior [27, 28] near GBs in anisotropic materials are strongly

affected by the orientations of the grains.

Previous works either focus on special cases, which are not guaranteed to find the stress build-up extrema [17–19], or focus on polycrystals, which yield many details but do not easily reveal general rules about specific GBs [23–26].

This work starts from a bicrystal model with an external stress σ^E perpendicular to the GB, aiming to identify the extrema of the IS and to gain insight into the stress state. We derive an analytical solution for the extreme value of the IS at the GB in terms of the elastic tensor components. It is revealed that the GB with the highest IS is the same for all cubic materials. Furthermore, the magnitude of IS for general GBs under perpendicular uniaxial applied stress is quantitatively described.

2.3 Bicrystal Model

The bicrystal model applied in this study is shown in Fig. 3.1. The 3-dimensional space is divided into two semi-infinite half-spaces separated by the GB. In keeping consistency with previous work [21], the GB plane is fixed parallel to the global XOZ plane, and the direction of σ^E is set along the global Y-axis, perpendicular to the GB. We firstly focus on the stress state near GBs that are perpendicular to σ^E. Experiments [29] and simulations [25] suggest that GBs perpendicular to σ^E are more likely to be the initial site of failure.

Two grains with the same material property but with different orientations are labeled as grain I and grain II. For cubic materials, the orientations of crystals can be conveniently described with Miller indices. For grain I,

$$\hat{e}^I = \begin{bmatrix} l_x^I & l_y^I & l_z^I \\ m_x^I & m_y^I & m_z^I \\ n_x^I & n_y^I & n_z^I \end{bmatrix}, \tag{2.1}$$

where $\boldsymbol{l}^I$, $\boldsymbol{m}^I$, $\boldsymbol{n}^I$ are normalized Miller indices of the crystallographic orientation of grain I corresponding to X, Y, and Z-axis in global coordinate system, respectively. Then the orientation of grain I is uniquely represented with $[l_x^I \ l_y^I \ l_z^I]$ and $[m_x^I \ m_y^I \ m_z^I]$, and analogously for grain II.

The compliance tensor S' after rotation $\hat{e}$, is given by

$$S'_{mnop} = \hat{e}_{mi}\hat{e}_{nj}\hat{e}_{ok}\hat{e}_{pl}S_{ijkl}, \tag{2.2}$$

in which S is the compliance tensor in the cubic crystal coordinate system.

Within the continuum description of GBs the following constraints apply for the bicrystal model.

1. The two grains are rigidly glued together at the GB. No relative motion is allowed at the GB.

2
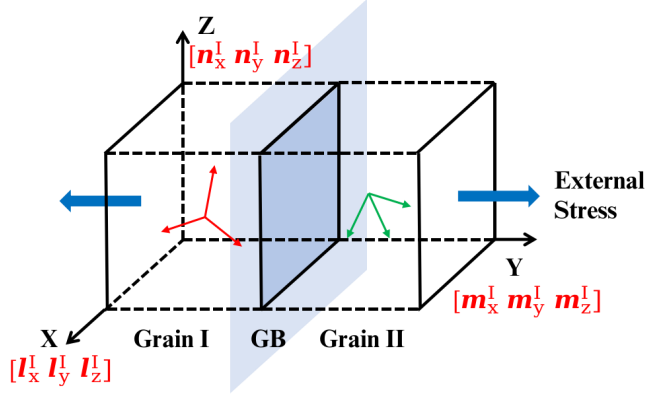
Figure 2.1: (Color online) The schematic figure of the bicrystal model in this work. The size of the GB in the X and Z direction is infinite. The two grains are semi-infinite. The orientation of each grain is represented by three Miller indices. The blue arrows show the uniaxial external stress σ^{E} applied far from the GB, which is perpendicular to GB plane. The label of the grain is shown at the superscript.

2. The model contains only one GB with infinite size. The interaction between GBs is not included.

3. The model is valid within the linear elastic limit.

4. σ^{E} is along global Y-axis, which is perpendicular to the GB plane.

Considering the equilibrium equations for momentum, the stress field in the bicrystal model must be invariant with respect to the Y coordinate. The discontinuity of a scalar field $g(x_i)$ at the GB is represented as $[g] = g^{\mathrm{I}} - g^{\mathrm{II}}$ then IS can be presented as $[\sigma_{\mathrm{ij}}]$.

The constitutive equation of a linear elastic material is

$$\varepsilon_{ij} = S_{ijkl}\sigma_{kl}. \tag{2.3}$$

According to the first constraint listed above, strain components in the GB plane are continuous,

$$[\varepsilon_{ij}] = 0, \quad i, j = 1, 3. \tag{2.4}$$

Since σ^{E} is a far-field stress, global stress equilibrium requires

$$\frac{1}{V}\int_V \sigma_{ij}dV = \Sigma_{ij}, \tag{2.5}$$

where Σ_{ij} is the general external stress [20]. In this problem Σ_{ij} only contains σ^E. So

$$\begin{cases} \sigma_{22}^I = \sigma_{22}^{II} = \sigma^E \\ \sigma_{23}^I = \sigma_{23}^{II} = 0 \\ \sigma_{12}^I = \sigma_{12}^{II} = 0 \end{cases} . \tag{2.6}$$

Since the model assumes that each grain occupies half the space, Eq. 4.4 is equivalent to

$$\Sigma_{ij} = \frac{1}{2}(\sigma_{ij}^I + \sigma_{ij}^{II}). \tag{2.7}$$

Then for in-plane stress components can be written as

$$\sigma_{ij}^I + \sigma_{ij}^{II} = 0, \quad i, j = 1, 3. \tag{2.8}$$

According to Eq. 2.6, the stress states at both sides of the GB are

$$\begin{cases} \sigma^I = [\sigma_1, \sigma^E, \sigma_3, 0, \sigma_5, 0] \\ \sigma^{II} = [-\sigma_1, \sigma^E, -\sigma_3, 0, -\sigma_5, 0], \end{cases} \tag{2.9}$$

with Voigt notation (xx $\rightarrow$ 1, yy $\rightarrow$ 2, zz $\rightarrow$ 3, yz $\rightarrow$ 4, xz $\rightarrow$ 5, xy $\rightarrow$ 6). Noticing σ_4 and σ_6 are zero, the global Y-axis is one of the principal directions for the stress state. When the global coordinate system is rotated around its Y-axis, the in-plane stress components can be represented by a Mohr circle. Then $(\sigma_1 + \sigma_3)$ is an invariant for $[\sigma_{ij}]$ during the rotation.

Consider the discontinuity of hydrostatic stress σ_h at the GB,

$$[\sigma_h] = \frac{2(\sigma_1 + \sigma_3)}{3}. \tag{2.10}$$

As our description is in the linear elastic limit, all stresses are proportional to σ^E. Therefore it is convenient to define an incompatibility factor (IF) as

$$IF = \frac{\sigma_1 + \sigma_3}{\sigma^E}. \tag{2.11}$$

When exchanging the labeling of the two grains, IF changes sign, so that only the absolute value of IF has physical meaning. Then σ_h at either side of GB can be expressed as

$$\sigma_h = \frac{(1 \pm IF)\sigma^E}{3} \tag{2.12}$$

In Appendix A a Python module is provided for computing IF analytically.

2.4 Analytical expression for the extreme incompatibility stress

Hayes and Shuvalov proposed a parameter χ to characterize the Young's modulus anisotropy of cubic crystals [30],

$$\chi = 2s_{11} - 2s_{12} - s_{44}. \tag{2.13}$$

Here s_{ij} refers to compliance components written with Voigt notation and with the engineering convention ($s_{44} = 4s_{yzyz} = 4s_{xyxy} = 4s_{xzxz}$). Here we derive a property of 4th rank tensors of cubic crystals using Voigt notation, with special application to the compliance matrix. The compliance matrix after rotation is given as (see Appendix B for details)

$$S' = S + \chi F(l, m, n), \tag{2.14}$$

where F is a 6 by 6 symmetric matrix of polynomials of l, m, n components, e.g.

$$F_{22} = -(m_x^2 m_y^2 + m_x^2 m_z^2 + m_y^2 m_z^2), \tag{2.15}$$

$$F_{25} = m_x^2 l_x n_x + m_y^2 l_y n_y + m_z^2 l_z n_z, \tag{2.16}$$

$$F_{55} = -4(n_x n_y l_x l_y + n_x n_z l_x l_z + n_y n_z l_y l_z). \tag{2.17}$$

Since F doesn't contain any elastic tensor components, it is common for all cubic materials.

For two grains with compliance tensor S^{I} and S^{II} it is convenient to properly rotate the coordinate system along Y axis to make $\sigma_1 = \sigma_3$. According to Eq. 4.1, 3.8, and B.50, the strain continuity equation (Eq.4.2) can be recast as

$$
\begin{cases}
[(F_{11}^{I} + F_{11}^{II})\chi + 2s_{11} + (F_{13}^{I} + F_{13}^{II})\chi + 2s_{12}]\sigma_1 + (F_{12}^{I} - F_{12}^{II})\chi\sigma^{E} + (F_{15}^{I} + F_{15}^{II})\chi\sigma_5 = 0, \\
[(F_{33}^{I} + F_{33}^{II})\chi + 2s_{11} + (F_{31}^{I} + F_{31}^{II})\chi + 2s_{12}]\sigma_1 + (F_{32}^{I} - F_{32}^{II})\chi\sigma^{E} + (F_{35}^{I} + F_{35}^{II})\chi\sigma_5 = 0, \\
(F_{51}^{I} + F_{51}^{II} + F_{53}^{I} + F_{53}^{II})\chi\sigma_1 + (F_{52}^{I} - F_{52}^{II})\chi\sigma^{E} + [(F_{55}^{I} + F_{55}^{II})\chi + 2s_{44}]\sigma_5 = 0.
\end{cases}
\tag{2.18}
$$

Then considering the orthonormality of l, m, and n of $\hat{e}$, the expression for σ_1 is simplified as

$$\frac{\sigma_1}{\sigma^{E}} = \frac{(F_{22}^{I} - F_{22}^{II})[(F_{55}^{I} + F_{55}^{II})\chi + 2s_{44}]\chi - [(F_{25}^{I})^2 - (F_{25}^{II})^2]\chi^2}{[(F_{22}^{I} + F_{22}^{II})\chi + 4s_{11} + 4s_{12}][(F_{55}^{I} + F_{55}^{II})\chi + 2s_{44}] - (F_{25}^{I} + F_{25}^{II})^2\chi^2}. \tag{2.19}$$

Considering a global coordinate system rotated around Y-axis such that $\sigma_1 = \sigma_3$, it follows that

$$IF = \frac{2\sigma_1}{\sigma^{E}}. \tag{2.20}$$

Then, Eq. 2.19 shows the orientation dependence of σ_1 as well as of IF. Referring to Eq. 3.15, B.40, and B.43, for each grain, we can consider F_{22} as reflecting the effects

of two degrees of freedom of the grain rotation, while F_{25} contains the remaining 1 degree of freedom, which represents the rotation of the grain around the Y-axis. Considering the connection between Young's modulus of the grain along the global Y-axis and compliance components, as

$$E_Y = \frac{1}{S'_{22}} = \frac{1}{F_{22}\chi + s_{11}}, \tag{2.21}$$

terms with F_{22} show the influence of the stiffness of the grain along the global Y-axis. Eq. 2.19 fits well with our intuition about the IS. Intuitively, one might link the IS to the difference of transverse strain (induced by the Poisson effect) across the GB. A grain with a low (high) Young's modulus along the loading direction has a large (small) positive longitudinal elastic strain, which leads to a large (small) negative transverse strain in the GB plane. Thus the IF is related to the discontinuity of the Young's modulus along the Y-axis.

According to Eq. 3.15, the range of F_{22} is estimated as

$$F_{22} = -(m_x^2 m_y^2 + m_x^2 m_z^2 + m_y^2 m_z^2) = \frac{m_x^4 + m_y^4 + m_z^4 - 1}{2}. \tag{2.22}$$

The maximum (minimum) of F_{22} is 0 $(-\frac{1}{3})$ when $\boldsymbol{m}$ is along $\langle 1\ 0\ 0 \rangle$ ($\langle 1\ 1\ 1 \rangle$). For F_{55}, Eq. B.43 can be written as

$$F_{55} = -4(n_x n_y l_x l_y + n_x n_z l_x l_z + n_y n_z l_y l_z) = 2(l_x^2 n_x^2 + l_y^2 n_y^2 + l_z^2 n_z^2). \tag{2.23}$$

The maximum (minimum) of F_{55} is 1 (0) when $\boldsymbol{l}$, $\boldsymbol{n}$ are along $\langle 1\ 1\ 0 \rangle$ and $\langle -1\ 1\ 0 \rangle$ ($\langle 1\ 0\ 0 \rangle$ and $\langle 0\ 1\ 1 \rangle$), $\boldsymbol{l}$ and $\boldsymbol{n}$ can be exchanged.

The value of F_{25} is found numerically, which gives a maximum of $\frac{1}{4}$ when $\boldsymbol{l}$, $\boldsymbol{m}$ are along $\langle 1\ -1\ \sqrt{2} \rangle$ and $\langle 1\ 1\ 0 \rangle$ (in arbitrary order), respectively. When exchanging the sequence of $\boldsymbol{l}$ and $\boldsymbol{n}$, F_{25} changes its sign. F_{25} approaches 0 when F_{22} approaches its extrema.

It's difficult to derive the extreme value of σ_1/σ^E mathematically since Eq. 2.19 contains both rotation variables and material elastic components. The following two points are considered to search for the maximum σ_1/σ^E.

1. F_{25} is much less than 1, and it appears quadratically only. This shows that the influence of the rotation of the grain around the Y-axis is relatively small.

2. When F_{22} approaches its extremum, i.e. $F_{22} = 0$ and $F_{22} = -\frac{1}{3}$, terms with F_{25} vanish.

Then the expression of $\sigma_1/\sigma^{\mathrm{E}}$ simplifies to

$$
\begin{aligned}
\frac{\sigma_1}{\sigma^{\mathrm{E}}} &\approx \frac{(F_{22}^{\mathrm{I}} - F_{22}^{\mathrm{II}})[(F_{55}^{\mathrm{I}} + F_{55}^{\mathrm{II}})\chi + 2s_{44}]\chi}{[(F_{22}^{\mathrm{I}} + F_{22}^{\mathrm{II}})\chi + 4s_{11} + 4s_{12}][(F_{55}^{\mathrm{I}} + F_{55}^{\mathrm{II}})\chi + 2s_{44}]} \\
&= \frac{(F_{22}^{\mathrm{I}} - F_{22}^{\mathrm{II}})\chi}{[(F_{22}^{\mathrm{I}} + F_{22}^{\mathrm{II}})\chi + 4s_{11} + 4s_{12}]}.
\end{aligned}
\tag{2.24}
$$
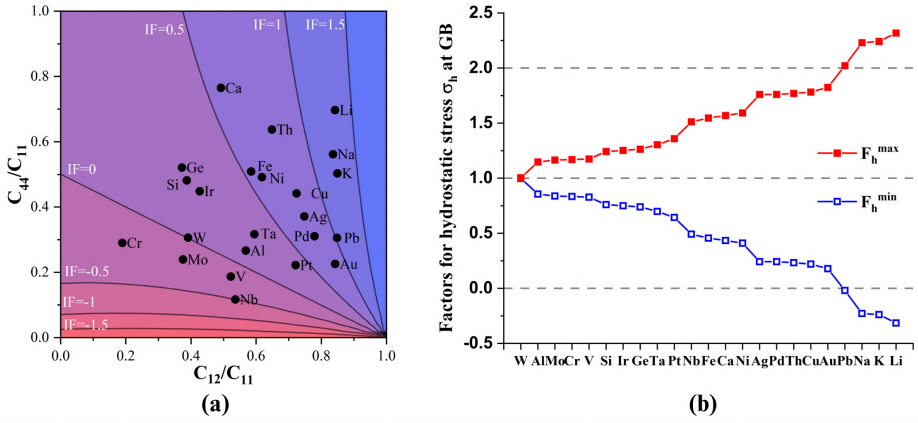
Figure 2.2: (Color online) (a) The relation between elastic components and maximum incompatibility factor, according to Eq. 6.1. The positions of common metals are labeled with black solid circles. (b) The maximum and minimum stress concentration factor F_{h} for hydrostatic stress σ_{h} at GBs for common metals, according to Eq. 2.31.

For $\chi > 0$ ($\chi < 0$), the maximum (minimum) for Eq. 2.24 is achieved when $F_{22}^{\mathrm{I}} = 0$ and $F_{22}^{\mathrm{II}} = -\frac{1}{3}$, which corresponds to $\boldsymbol{m}^I$ and $\boldsymbol{m}^{\mathrm{II}}$ parallel to $\langle 1\ 0\ 0 \rangle$ and $\langle 1\ 1\ 1 \rangle$, respectively. With Eq. 3.11 and 2.24, and $\sigma_1 = \sigma_3$, the maximum value of IF is

$$
\begin{aligned}
IF^{\max} &= \frac{2\chi/3}{-\chi/3 + 4s_{11} + 4s_{12}} \\
&= \frac{4s_{11} - 4s_{12} - 2s_{44}}{10s_{11} + 14s_{12} + s_{44}} \\
&= \frac{-2(C_{11} - C_{12} - 2C_{44})(C_{11} + 2C_{12})}{(10C_{11} - 4C_{12})C_{44} + (C_{11} - C_{12})(C_{11} + 2C_{12})}.
\end{aligned}
\tag{2.25}
$$

The relationship between the stiffness constants C_{ij} and the compliance constants

s_{ij} for a cubic crystal system is given by:

$$s_{11} = \frac{C_{11} + C_{12}}{(C_{11} - C_{12})(C_{11} + 2C_{12})}, \tag{2.26}$$

$$s_{12} = \frac{-C_{12}}{(C_{11} - C_{12})(C_{11} + 2C_{12})}, \tag{2.27}$$

$$s_{44} = \frac{1}{C_{44}}. \tag{2.28}$$

After conducting large-scale sampling of IF for the bicrystal model with various grain orientations, it is confirmed that Eq. 6.1 represents the global maximum of IF.

We found the magnitude of IF is related to the elastic instability of cubic crystals. The elastic stability conditions for cubic crystals are

$$C_{11} - C_{12} > 0, \quad C_{11} + 2C_{12} > 0, \quad C_{44} > 0, \tag{2.29}$$

or, equivalently

$$-\frac{1}{2} < \frac{C_{12}}{C_{11}} < 1, \quad \frac{C_{44}}{C_{11}} > 0. \tag{2.30}$$

The IF^{max} values, as computed with Eq. 6.1, for common metals are shown in Fig. 2.2(a) using the experimentally determined elastic tensor components [31]. When C_{12}/C_{11} approaches 1, or C_{44}/C_{11} approaches 0, which means the stability of the crystal is low according to Eq. 2.30, the absolute value of IF^{max} rises rapidly.

In alloys the IF^{max} can be designed on purpose. The types and concentrations of alloying elements can influence the elastic properties of alloys as has been shown experimentally and computationally [32, 33]. By designing alloys with low IF^{max} using Fig. 2.2(a), it might be possible to improve properties that are sensitive to the stress state at GBs.

2.5 Incompatibility stress for general grain boundaries

At the GB, not only the discontinuities in stresses are of interest, but large values of local stresses themselves are of importance too. Therefore, the σ_{h} values on both sides of the GB corresponding to IF^{max} are calculated. The stress concentration factor F_{h} is defined as the ratio of the σ_{h} values on both sides of the GB to the value of the hydrostatic stress without a GB under σ^{E},

$$F_{\mathrm{h}} = \frac{3\sigma_{\mathrm{h}}}{\sigma^{\mathrm{E}}} = 1 \pm IF. \tag{2.31}$$

The most extreme F_{h} for common metals are shown in Fig. 2.2(b). For common engineering metal bicrystals under a uniaxial σ^{E} perpendicular to the GB, the

variation of σ_h at a GB is 14% for aluminum, 54% for iron and nickel, and 78% for copper. In alkali metals, F_h can take a negative value, indicating that dilatation in bulk can give rise to compression on one side of the GB and large tension on the other side. As both σ_h and its gradient [34] play significant roles in the segregation and diffusivity [35] of interstitial atomic species and poorly fitting substitutional atomic species, precipitation processes can be affected particularly in materials with large variations in F_h values.

Based on Eq. 2.21 and 2.24, IF is further simplified as

$$
\begin{aligned}
IF &\approx \frac{1/E_Y^I - 1/E_Y^{II}}{(F_{22}^I + F_{22}^{II})\chi + 4s_{11} + 4s_{12}} \\
&\approx \frac{6(1/E_Y^I - 1/E_Y^{II})}{10s_{11} + 14s_{12} + s_{44}},
\end{aligned}
\tag{2.32}
$$

where E_Y^I (E_Y^{II}) is the Young's modulus of grain I (II) along the global Y-axis. Here $(F_{22}^I + F_{22}^{II})\chi$ in the denominator is replaced by $-\frac{1}{3}\chi$ to ensure the accuracy of the approximation in predicting high absolute values of IF.

Eq. 6.2 disregards the stress variations arising from rotating the two grains around the direction of σ^E for two reasons. Firstly, IF, being defined as sum of σ_1/σ^E and σ_3/σ^E, is less sensitive to variations of individual stress components. Secondly, the bicrystal structure displays at least a four-fold symmetry during the rotation around global Y-axis. This equation is in good agreement with the analytical results (see Appendix C). Hence, while $\boldsymbol{m}^I$ and $\boldsymbol{m}^{II}$ have a strong influence on IF, the other four Miller indices have little effect. Therefore, the GB in the bicrystal model can be characterized by $\boldsymbol{m}^I$ and $\boldsymbol{m}^{II}$.

In order to clarify the role of the orientations of the two grains, we define a rescaled incompatibility factor for GBs

$$
IF^{GB} = IF/IF^{max},
\tag{2.33}
$$

ranging from -1 to 1, which is independent of the elastic anisotropy. The IF^{GB} for low-index GBs are shown in Fig. 2.3(a).

For general GBs, it is convenient to define the compliance factor (CF) to separate the contributions to IF^{GB} from each grain. For grain I,

$$
\begin{aligned}
CF^I &= \frac{1/E^{min} - 1/E_Y^I}{1/E^{min} - 1/E^{max}} \\
&= -3F_{22}^I \\
&= 3\left((m_x^I m_y^I)^2 + (m_x^I m_z^I)^2 + (m_y^I m_z^I)^2\right),
\end{aligned}
\tag{2.34}
$$
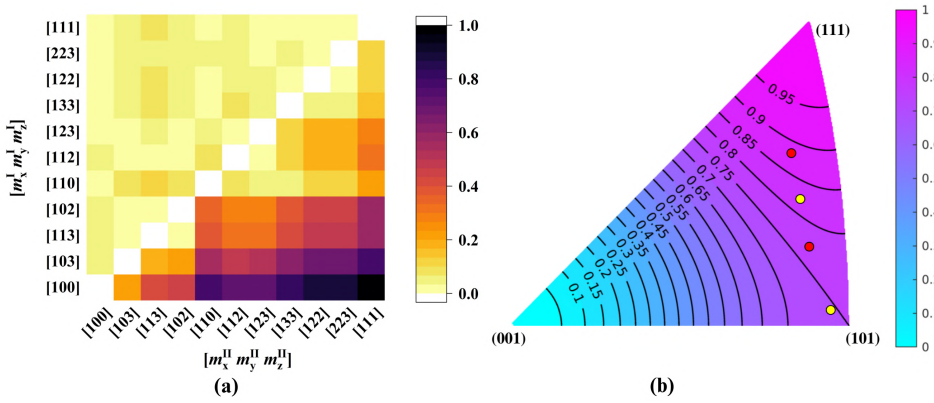
Figure 2.3: (Color online) (a) For low-index GBs, IF^{GB} estimated by Eq. 2.35 are shown below the diagonal, while above the diagonal the maximum absolute value of IF^{GB}(exact) - IF^{GB}(Eq. 2.35) that occurs when one of the two grains is rotated around the Y-axis is displayed. (b) Compliance factor as function of the grain orientation according to Eq. 2.34. The orientations of two bicrystals in [36] are presented by red dots for one bicrystal and yellow dots for another bicrystal.

where E^{min}, E^{max} are the minimum and maximum Young's modulus for the material, and analogous for grain II. Then IF^{GB} is expressed as

$$IF^{GB} = CF^{II} - CF^{I}. \tag{2.35}$$

Fig. 2.3(b) shows a contour plot of CF as function of $\boldsymbol{m}$ of each grain in a (0 0 1) inverse pole figure. This figure displays two important features.

First, the geometry of each GB can be presented as two points, corresponding to grain I and grain II, in Fig. 2.3(b). Then the rescaled IF for a given GB can be read from the map according to Eq. 2.35, e.g. the maximum of IF^{GB}, at 1, corresponds to $\boldsymbol{m}^{I}$, $\boldsymbol{m}^{II}$ parallel to [1 0 0] and [1 1 1], respectively.

Second, the IF for GBs with large misorientation is not always large. The IF vanishes for two grains with orientations located along a contour line. Therefore, even for materials with high anisotropy, it is possible to design textures with near-zero stress incompatibility at GBs.

Considering the proportional relationship between IF and $[\sigma_h]$ shown in Eq. 2.21, Fig. 2.3 is also valid for estimating the magnitude of $[\sigma_h]$ for various GBs.

In recent in-situ tensile tests of bicrystals [36], the orientations of grains at both sides of GBs are represented by pairs of dots in Fig. 2.3(b). The corresponding IF^{GB} is approximately 0.1. This implies that the stress incompatibility in the experiments are only 1/10 of the most extreme configuration. This may explain why the initial fracture position in the experiments did not occur at pre-existing GBs [36].

2.6 Conclusion

In summary, we have quantified incompatibility factor $IF = (\sigma_1 + \sigma_3)/\sigma^E$ and the discontinuity in hydrostatic stress σ_h near grain boundaries under external stress σ^E with a bicrystal model. The extreme values have been derived in terms of elastic tensor components. The incompatibility factors for general grain boundaries are estimated based on grain orientations. These findings provide valuable insights into failure phenomena, such as creep and fatigue, that occur in polycrystalline materials. Moreover, identifying grain boundaries with high and low stress concentration can guide the design of higher-performing materials.

APPENDIX A PYTHON MODULE FOR INCOMPATIBILITY FACTOR CALCULATION

The module is made available under MIT license on gitlab.tudelft.nl/kliu6/incompatibility-stress.

APPENDIX B COMPONENTS OF MATRIX F

Rotation matrix is denoted as

$$\hat{e} = \begin{bmatrix} l_x & l_y & l_z \\ m_x & m_y & m_z \\ n_x & n_y & n_z \end{bmatrix} \tag{B.1}$$

The $\mathbf{l}$, $\mathbf{m}$, and $\mathbf{n}$ satisfy the following equations:

$$\mathbf{l} \cdot \mathbf{l} = \mathbf{m} \cdot \mathbf{m} = \mathbf{n} \cdot \mathbf{n} = 1 \tag{B.2}$$

$$\mathbf{l} \cdot \mathbf{m} = \mathbf{m} \cdot \mathbf{n} = \mathbf{n} \cdot \mathbf{l} = 0 \tag{B.3}$$

$$l_i l_j + m_i m_j + n_i n_j = 0 \tag{B.4}$$

$$l_i^2 + m_i^2 + n_i^2 = 1 \tag{B.5}$$

where $i, j = \{x, y, z\}$. For convenience of presentation, the compliance before rotation is given in matrix form with Voigt notation (xx $\to$ 1, yy $\to$ 2, zz$\to$ 3, yz $\to$ 4, xz $\to$ 5, xy $\to$ 6, $s_{44} = 4s_{yzyz} = 4s_{xyxy} = 4s_{xzxz}$):

$$S = \begin{bmatrix} s_{11} & s_{12} & s_{12} & 0 & 0 & 0 \\ s_{12} & s_{11} & s_{12} & 0 & 0 & 0 \\ s_{12} & s_{12} & s_{11} & 0 & 0 & 0 \\ 0 & 0 & 0 & s_{44} & 0 & 0 \\ 0 & 0 & 0 & 0 & s_{44} & 0 \\ 0 & 0 & 0 & 0 & 0 & s_{44} \end{bmatrix} \tag{B.6}$$

The compliance tensor S' after rotating the crystal with $\hat{e}$ is given by

$$S'_{mnop} = \hat{e}_{mi}\hat{e}_{nj}\hat{e}_{ok}\hat{e}_{pl}S_{ijkl}. \tag{B.7}$$

Then S'_{11} can be explicitly calculated as

$$S'_{11} = l_x{}^4 s_{11} + (l_y{}^2 + l_z{}^2)(2s_{12} + s_{44})l_x{}^2 + l_y{}^4 s_{11} + l_z{}^2(2s_{12} + s_{44})l_y{}^2 + l_z{}^4 s_{11}. \tag{B.8}$$

Since

$$(l_x^2 + l_y^2 + l_z^2)^2 = l_x^4 + l_y^4 + l_z^4 + 2l_x^2 l_y^2 + 2l_x^2 l_z^2 + 2l_y^2 l_z^2 = 1, \tag{B.9}$$

2

Eq. B.8 is recast as

$$S'_{11} = [1 - 2(l_x^2 l_y^2 + l_x^2 l_z^2 + l_y^2 l_z^2)]s_{11} + 2(l_x^2 l_y^2 + l_x^2 l_z^2 + l_y^2 l_z^2)s_{22} + (l_x^2 l_y^2 + l_x^2 l_z^2 + l_y^2 l_z^2)s_{44}.$$
(B.10)

substituting the definition of χ, $2s_{11} - 2s_{12} - s_{44} = \chi$, then yields,

$$S'_{11} = s_{11} + F_{11}\chi,$$
(B.11)

where

$$F_{11} = -(l_x^2 l_y^2 + l_x^2 l_z^2 + l_y^2 l_z^2).$$
(B.12)

S'_{12} can be explicitly calculated as

$$S'_{12} = m_x^2 l_x^2 s_{11} + m_x^2 l_y^2 s_{12} + m_x^2 l_z^2 s_{12} + m_x m_y l_x l_y s_{44} + m_x m_z l_x l_z s_{44} + m_y^2 l_x^2 s_{12}$$
$$+ m_y^2 l_y^2 s_{11} + m_y^2 l_z^2 s_{12} + m_y m_z l_y l_z s_{44} + m_z^2 l_x^2 s_{12} + m_z^2 l_y^2 s_{12} + m_z^2 l_z^2 s_{11}$$
(B.13)

Utilizing the following equations

$$(m_x l_x + m_y l_y + m_z l_z)^2 = m_x^2 l_x^2 + m_y^2 l_y^2 + m_z^2 l_z^2 + 2(m_x m_y l_x l_y + m_x m_z l_x l_z + m_y m_z l_y l_z) = 0,$$
(B.14)
$$m_x^2 l_x^2 + m_y^2 l_y^2 + m_z^2 l_z^2 = -2(m_x m_y l_x l_y + m_x m_z l_x l_z + m_y m_z l_y l_z),$$
(B.15)

and

$$(l_x^2 + l_y^2 + l_z^2)(m_x^2 + m_y^2 + m_z^2) = (m_x^2 l_x^2 + m_y^2 l_y^2 + m_z^2 l_z^2) + (m_x^2 l_y^2 + m_y^2 l_z^2 + m_z^2 l_x^2 + m_x^2 l_z^2 + m_z^2 l_y^2 + m_y^2 l_x^2) = 1,$$
(B.16)

which gives

$$m_x^2 l_y^2 + m_y^2 l_z^2 + m_z^2 l_x^2 + m_x^2 l_z^2 + m_z^2 l_y^2 + m_y^2 l_x^2 = 1 - m_x^2 l_x^2 + m_y^2 l_y^2 + m_z^2 l_z^2$$
$$= 1 + 2(m_x m_y l_x l_y + m_x m_z l_x l_z + m_y m_z l_y l_z),$$
(B.17)

Eq. B.13 is recast as

$$S'_{12} = -2(m_x m_y l_x l_y + m_x m_z l_x l_z + m_y m_z l_y l_z)s_{11} + [1 + 2(m_x m_y l_x l_y + m_x m_z l_x l_z + m_y m_z l_y l_z)]s_{12}$$
$$+ (m_x m_y l_x l_y + m_x m_z l_x l_z + m_y m_z l_y l_z)s_{44}.$$
(B.18)

and upon substituting the definition of χ,

$$S'_{12} = s_{12} + F_{12}\chi,$$
(B.19)

where

$$F_{12} = -(m_x m_y l_x l_y + m_x m_z l_x l_z + m_y m_z l_y l_z).$$
(B.20)

S'_{14} can be explicitly calculated as

$$
\begin{aligned}
S'_{14} =&(2m_x n_x l_x{}^2 + 2m_y n_y l_y{}^2 + 2m_z n_z l_z{}^2)s_{11} + (2m_y n_y + 2m_z n_z)s_{12}l_x{}^2 \\
&+ [(m_x n_y + m_y n_x)l_y + l_z(m_x n_z + m_z n_x)]s_{44}l_x \\
&+ (2m_x n_x + 2m_z n_z)s_{12}l_y{}^2 + s_{44}l_z(m_y n_z + m_z n_y)l_y + (2m_x n_x + 2m_y n_y)s_{12}l_z{}^2
\end{aligned}
$$
(B.21)

Considering

$$
n_x l_x + n_y l_y + n_z l_z = 0,
\tag{B.22}
$$

the coefficient of s_{44} reduces to

$$
\begin{aligned}
((m_x n_y &+ m_y n_x)l_y + l_z(m_x n_z + m_z n_x)) + l_z(m_y n_z + m_z n_y)l_y \\
&= m_x l_x(n_y l_y + n_z l_z) + m_y l_y(n_x l_x + n_z l_z) + m_z l_z(n_x l_x + n_y l_y) \\
&= -(m_x n_x l_x^2 + m_y n_y l_y^2 + m_z n_z l_z^2)
\end{aligned}
$$
(B.23)

Considering

$$
m_x n_x + m_y n_y + m_z n_z = 0,
\tag{B.24}
$$

the coefficient of s_{12} reduces to

$$
\begin{aligned}
(2m_y n_y &+ 2m_z n_z)l_x^2 + (2m_x n_x + 2m_z n_z)l_y^2 + (2m_x n_x + 2m_y n_y)l_z^2 \\
&= 2(m_x n_x l_x{}^2 + 2m_y n_y l_y{}^2 + 2m_z n_z l_z{}^2)
\end{aligned}
$$
(B.25)

Then again introducing χ, Eq. B.21 is recast as

$$
S'_{14} = F_{14}\chi,
\tag{B.26}
$$

where

$$
F_{14} = m_x n_x l_x^2 + m_y n_y l_y^2 + m_z n_z l_z^2.
\tag{B.27}
$$

With similar transformations the other elements S'_{13}, S'_{15}, S'_{16}, etc., of the compliance matrix after rotation can be written as

$$
S' =
\begin{bmatrix}
s_{11} + F_{11}\chi & s_{12} + F_{12}\chi & s_{12} + F_{13}\chi & F_{14}\chi & F_{15}\chi & F_{16}\chi \\
 & s_{11} + F_{22}\chi & s_{12} + F_{23}\chi & F_{24}\chi & F_{25}\chi & F_{26}\chi \\
 & & s_{11} + F_{33}\chi & F_{34}\chi & F_{35}\chi & F_{36}\chi \\
 & & & s_{44} + F_{44}\chi & F_{45}\chi & F_{46}\chi \\
 & symmetric & & & s_{44} + F_{55}\chi & F_{56}\chi \\
 & & & & & s_{44} + F_{66}\chi
\end{bmatrix}
$$
(B.28)

where F_{ij} are polynomials of l, m, n, as

$$
F_{11} = -(l_x^2 l_y^2 + l_x^2 l_z^2 + l_y^2 l_z^2)
\tag{B.29}
$$

$$F_{12} = -(m_x m_y l_x l_y + m_x m_z l_x l_z + m_y m_z l_y l_z) \tag{B.30}$$

$$F_{22} = -(m_x^2 m_y^2 + m_x^2 m_z^2 + m_y^2 m_z^2) \tag{B.31}$$

$$F_{13} = -(n_x n_y l_x l_y + n_x n_z l_x l_z + n_y n_z l_y l_z) \tag{B.32}$$

$$F_{23} = -(n_x n_y m_x m_y + n_x n_z m_x m_z + n_y n_z m_y m_z) \tag{B.33}$$

$$F_{33} = -(n_x^2 n_y^2 + n_x^2 n_z^2 + n_y^2 n_z^2) \tag{B.34}$$

$$F_{14} = m_x n_x l_x^2 + m_y n_y l_y^2 + m_z n_z l_z^2 \tag{B.35}$$

$$F_{24} = m_x^3 n_x + m_y^3 n_y + m_z^3 n_z \tag{B.36}$$

$$F_{34} = m_x n_x^3 + m_y n_y^3 + m_z n_z^3 \tag{B.37}$$

$$F_{44} = -4(n_x n_y m_x m_y + n_x n_z m_x m_z + n_y n_z m_y m_z) \tag{B.38}$$

$$F_{15} = l_x^3 n_x + l_y^3 n_y + l_z^3 n_z \tag{B.39}$$

$$F_{25} = m_x^2 n_x l_x + m_y^2 n_y l_y + m_z^2 n_z l_z \tag{B.40}$$

$$F_{35} = l_x n_x^3 + l_y n_y^3 + l_z n_z^3 \tag{B.41}$$

$$F_{45} = 2(m_x n_x^2 l_x + m_y n_y^2 l_y + m_z n_z^2 l_z) \tag{B.42}$$

$$F_{55} = -4(n_x n_y l_x l_y + n_x n_z l_x l_z + n_y n_z l_y l_z) \tag{B.43}$$

$$F_{16} = l_x^3 m_x + l_y^3 m_y + l_z^3 m_z \tag{B.44}$$

$$F_{26} = l_x m_x^3 + l_y m_y^3 + l_z m_z^3 \tag{B.45}$$

$$F_{36} = m_x n_x^2 l_x + m_y n_y^2 l_y + m_z n_z^2 l_z \tag{B.46}$$

$$F_{46} = 2(m_x^2 n_x l_x + m_y^2 n_y l_y + m_z^2 n_z l_z) \tag{B.47}$$

$$F_{56} = 2(m_x n_x l_x^2 + m_y n_y l_y^2 + m_z n_z l_z^2) \tag{B.48}$$

$$F_{66} = -4(m_x m_y l_x l_y + m_x m_z l_x l_z + m_y m_z l_y l_z) \tag{B.49}$$

Therefore

$$S' = S + \chi F(\boldsymbol{l}, \boldsymbol{m}, \boldsymbol{n}), \tag{B.50}$$

Of course, any other 4th rank tensor can be rotated in a similar fashion.

APPENDIX C APPROXIMATION OF IF FOR AN ARBITRARY GB

In the main text, we derived the exact expression for σ_1, one of the incompatibility stress components, as Eq. 19 in main text. The incompatibility factor IF is proportional to σ_1. The expression for σ_1 indicates that the rotations of the two grains around global Y-axis have a minor influence to the magnitude of σ_1. By disregarding the influence of the rotation around Y-axis and fixing the denominator as a constant, we derived the following equation to estimate the IF for an arbitrary GB.

$$IF \approx \frac{6(1/E_{\mathrm{I}} - 1/E_{\mathrm{II}})}{10s_{11} + 14s_{12} + s_{44}}, \tag{B.51}$$

IF as computed from Eq. B.51 are compared with the exact values for 50000 different GBs, for four metals (Al, Fe, Cu, Li). The results are shown in Fig.C.1. The histogram of IF and mean absolute error (MAE) of the estimation from Eq. B.51 are also presented. The MAE of the estimation from Eq.B.51 is within 10% for all 4 metals. The error is largest for Li, the most elastically anisotropic of the metals considered.
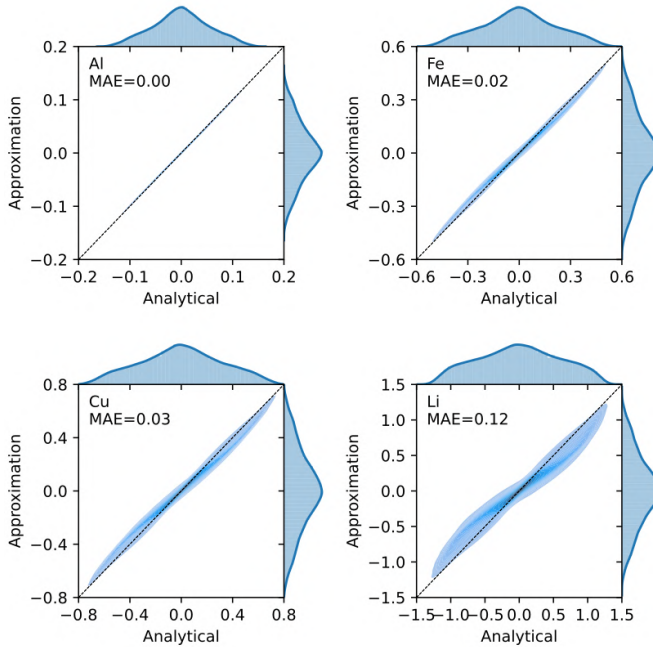
Figure C.1: Comparison of the analytical solution of IF, as computed according to the python module listed under Appendix A, and its approximation using Eq.B.51 for Al, Fe, Cu, and Li (in order of increasing elastic anisotropy).

2

References

[1] B. Schonfelder, D. Wolf, S.R. Phillpot, and M. Furtkamp. Molecular-dynamics method for the simulation of grain-boundary migration. *Interf. Sci.*, 5:245–262, 1997.

[2] M. Tonks, P. Millett, W. Cai, and D. Wolf. Analysis of the elastic strain energy driving force for grain boundary migration using phase field simulation. *Scr. Mater.*, 63:1049–1052, 11 2010.

[3] P. Lejcek and S. Hofmann. Thermodynamics and structural aspects of grain boundary segregation. *Crit. Rev. Solid. State*, 20:1–85, 1995.

[4] S. J. Fensin, J. P. Escobedo-Diaz, C. Brandl, E. K. Cerreta, G. T. Gray, T. C. Germann, and S. M. Valone. Effect of loading direction on grain boundary failure under shock loading. *Acta Mater.*, 64:113–122, 2014.

[5] N. J. Teng and T. H. Lin. Elastic anisotropy effect of crystals on polycrystal fatigue crack initiation. *J. Eng. Mater. Technol.*, 117:470–477, 1995.

[6] F. Lu, Z. Guang, and Z. Ke-shi. Grain boundary effects on the inelastic deformation behavior of bicrystals. *Mater. Sci. Eng. A*, 361:83–92, 11 2003.

[7] L. L. Li, P. Zhang, Z. J. Zhang, and Z. F. Zhang. Effect of crystallographic orientation and grain boundary character on fatigue cracking behaviors of coaxial copper bicrystals. *Acta Mater.*, 61:425–438, 2013.

[8] D. C. Crawford and G. S. Was. The role of grain boundary misorientation in intergranular cracking of Ni-16Cr-9Fe in 360 ^oC argon and high-purity water. *Metall. Mater. Trans. A*, 23:1195–1206, 1992.

[9] Y. Wei, A. F. Bower, and H. Gao. Recoverable creep deformation and transient local stress concentration due to heterogeneous grain-boundary diffusion and sliding in polycrystalline solids. *J. Mech. Phys. Solids*, 56:1460–1483, 2008.

[10] M. E. Kassner and M. T. Pérez-Prado. Five-power-law creep in single phase metals and alloys. *Prog. Mater. Sci.*, 45:1–102, 2000.

[11] B. Chen, P.E.J. Flewitt, A.C.F. Cocks, and D.J. Smith. A review of the changes of internal state related to high temperature creep of polycrystalline metals and alloys. *Int. Mater. Rev.*, 60:1–29, 2015.

[12] V. Randle. Grain boundary engineering: An overview after 25 years. *Mater. Sci. Technol.*, 26:253–261, 2010.

[13] J. Sidor, A. Miroux, R. Petrov, and L. Kestens. Microstructural and crystallographic aspects of conventional and asymmetric rolling processes. *Acta Mater.*, 56:2495–2507, 2008.

[14] K. A. Sofinowski, S. Raman, X. Wang, B. Gaskey, and M. Seita. Layer-wise engineering of grain orientation (LEGO) in laser powder bed fusion of stainless steel 316L. *Addit. Manuf.*, 38, 2 2021.

[15] J. Hou, R. Li, Q. Wang, H. Yu, Z. Zhang, Q. Chen, H. Ma, X. Wu, X. Li, and Z. Zhang. Breaking the trade-off relation of strength and electrical conductivity in pure Al wire by controlling texture and grain boundary. *J. Alloy. Compd.*, 769:96–109, 2018.

[16] L.A.I. Kestens and H. Pirgazi. Texture formation in metal alloys with cubic crystal structures. *Mater. Sci. Technol.*, 32:1303–1315, 2016.

[17] P. Peralta, L. Llanes, J. Bassani, and C. Laird. Deformation from twin-boundary stresses and the role of texture: Application to fatigue. *Philo. Mag.*, 70:219–232, 1994.

[18] S. Kumar, S. K. Kurtz, and V. K. Agarwala. Micro-stress distribution within polycrystalline aggregate. *Acta Mech.*, 114:203–216, 1996.

[19] P. Peralta and C. Laird. Compatibility stresses in fatigued bicrystals: Dependence on misorientation and small plastic deformations. *Acta Mater.*, 45:5129–5143, 1997.

[20] T. Richeton and S. Berbenni. Effects of heterogeneous elasticity coupled to plasticity on stresses and lattice rotations in bicrystals: A field dislocation mechanics viewpoint. *Eur. J. Mech. A-Solids*, 37:231–247, 2013.

[21] T. Richeton, I. Tiba, S. Berbenni, and O. Bouaziz. Analytical expressions of incompatibility stresses at $\Sigma 3 < 111 >$ twin boundaries and consequences on single-slip promotion parallel to twin plane. *Philos. Mag.*, 95:12–31, 2015.

[22] I. Tiba, T. Richeton, C. Motz, H. Vehoff, and S. Berbenni. Incompatibility stresses at grain boundaries in Ni bicrystalline micropillars analyzed by an anisotropic model and slip activity. *Acta Mater.*, 83:227–238, 2015.

[23] R. Ahluwalia, T. Lookman, and A. Saxena. Elastic deformation of polycrystals. *Phys. Rev. Lett.*, 91:1–4, 2003.

[24] Y. Zhao and R. Tryon. Automatic 3-D simulation and micro-stress distribution of polycrystalline metallic materials. *Comput. Methods Appl. Mech. Eng.*, 193:3919–3934, 2004.

2

[25] M. Kamaya, Y. Kawamura, and T. Kitamura. Three-dimensional local stress analysis on grain boundaries in polycrystalline material. *Int. J. Solids Struct.*, 44:3267–3277, 2007.

[26] Alireza Fallahi and Arash Ataee. Effects of crystal orientation on stress distribution near the triple junction in a tricrystal γ-TiAl. *Mater. Sci. Eng. A*, 527(18-19):4576–4581, 2010.

[27] Xiaolei Chen, Thiebaud Richeton, Christian Motz, and Stéphane Berbenni. Elastic fields due to dislocations in anisotropic bi-and tri-materials: applications to discrete dislocation pile-ups at grain boundaries. *International Journal of Solids and Structures*, 164:141–156, 2019.

[28] RH Wagoner. Calculating dislocation spacings in pile-ups at grain boundaries. *Metallurgical Transactions A*, 12:2015–2023, 1981.

[29] C. Gandhi and M. F. Ashby. Overview no. 5. fracture-mechanism maps for materials which cleave: F.C.C., B.C.C. and H.C.P. metals and ceramics. *Acta Metall.*, 27:1565–1602, 1979. Reference book for fracture type.

[30] M. Hayes and A. Shuvalov. On the extreme values of Young's modulus, the shear modulus, and Poisson's ratio for cubic materials a stress analysis method for bi-axially loaded fastener hole in composite laminate of finite geometry. *J. Appl. Mech.*, 65:786–787, 1998.

[31] E. A. Brandes and G. B. Brook. *Smithells metals reference book*. Elsevier, 2013.

[32] N. Gunkelmann, H. Ledbetter, and H. M. Urbassek. Experimental and atomistic study of the elastic properties of α' Fe-C martensite. *Acta Mater.*, 60:4901–4907, 2012.

[33] V. Revi, S. Kasodariya, A. Talapatra, G. Pilania, and A. Alankar. Machine learning elastic constants of multi-component alloys. *Comp. Mater. Sci.*, 198, 10 2021.

[34] H. Abdolvand. Progressive modelling and experimentation of hydrogen diffusion and precipitation in anisotropic polycrystals. *Int J Plasticity*, 116:39–61, 2019.

[35] M. Werner, H. Mehrer, and H. D. Hochheimer. Effect of hydrostatic pressure, temperature, and doping on self-diffusion in germanium. *Phys. Rev. B*, 32(6):3930, 1985.

[36] M. T. Kiani, L. T. Gan, R. Traylor, R. Yang, C. M. Barr, K. Hattar, J. A. Fan, and X. W. Gu. In situ TEM tensile testing of bicrystals with tailored misorientation angles. *Acta Mater.*, 224:117505, 2022.

2

3

3

INCOMPATIBILITY STRESS AT INCLINED GRAIN BOUNDARIES FOR CUBIC CRYSTALS UNDER HYDROSTATIC STRESS AND UNIAXIAL STRESS

3.1 Abstract

In a material under stress, grain boundaries may give rise to stress discontinuities. The stress state at grain boundaries strongly affects microscopic processes, such as diffusion and segregation, as well as failure initiation, such as fatigue, creep, and corrosion. Here the general condition of incompatibility stress at grain boundaries is studied with a bicrystal model for linear elastic materials. In materials with cubic crystal structures, it is proven that hydrostatic stress does not lead to a stress discontinuity at grain boundaries. For bicrystals with inclined grain boundaries under uniaxial stress, the extreme values of the incompatibility stress as a function of the inclination angle are obtained by a simulated annealing method. A simple criterion is proposed to classify cubic materials into three groups. For cubic crystals with at most moderate anisotropy, the highest incompatibility stress occurs when the grain boundary plane is perpendicular to the uniaxial stress. For highly anisotropic materials, such as alkali metals and polymorphic high-temperature phases, the highest incompatibility stress occurs on grain boundaries with an inclination of about 47º.

Keywords: Grain boundary, incompatibility stress, anisotropy, grain boundary inclination, stress concentration

3.2 Introduction

Most commercial metals are polycrystalline with properties that are strongly dependent on the amount and character of grain boundaries (GBs). Due to the anisotropy of the elastic tensor and the discontinuity of crystal orientations across GBs, maintaining deformation compatibility causes the stress states near GBs to deviate significantly from the average stress state.

Many microscopic processes in materials are strongly influenced by stress states near GBs, such as diffusion [1–3], segregation [4–6], and (nano)void formation [7]. Therefore failure processes also are connected with the stress state at GBs, such as fatigue [8–12], creep [13–15] and stress corrosion cracking[16–19]. The initiation of phase transformation is also strongly influenced by the local stress state [20–22].

The study of the stress state at GBs and its relation to GB parameters has been a challenge due to the many degrees of freedom of GBs [23]. Analytical solutions for the stress state near GBs were derived for several special grain boundaries [24, 25]. For general grain boundaries, Richeton and Berbenni [26] proposed an analytical solution with a bicrystal model. The model was verified by comparing it with finite element method (FEM) simulations. The results were used to study the activation of slip systems near the $\Sigma 3\langle 111 \rangle$ twin boundary [27]. Recently, Shawish and Mede [28] introduced a semi-analytical solution for the distribution of stresses along the GB normal within polycrystals under an arbitrary load with a perturbation method.

The stresses near grain boundaries for applied loads perpendicular to the grain boundaries were explored in Chapter 2. The GBs with the largest incompatibility stress were determined for all cubic materials with the GB plane being perpendicular to the external stress.

FEM provides a helpful tool for studying the stresses near GBs. By performing FEM simulation for the stress distribution in polycrystals under load, the relationship between stress states and GB parameters (grain orientation, GB inclination angle, etc) is clarified by statistical methods [29, 30] and machine learning [31]. These works revealed that the GB area, GB inclination angle, and the orientations of adjacent grains influence the occurrence of stress concentrations near GBs. However, these statistics-based correlations are descriptive rather than quantitative. In order to gain insight into the magnitude of stress discontinuities at an arbitrarily inclined GB in a general material and therefore take advantage of the local stress state, it is necessary to establish quantitative and physically meaningful rules between the GB characters, external stresses, and the stress discontinuities.

This work investigates the incompatibility stress for general GBs in materials with a cubic crystal structure with a bicrystal model. Section 2 introduces the bicrystal model for calculating the incompatibility stress with a fixed GB plane under arbitrary external stress. An approximation for incompatibility stress for cubic materials under arbitrary external stress is derived in section 3.1. In section 3.2, we prove that hydrostatic external stress does not lead to any stress discontinuity at GBs. In section 3.3, the incompatibility stress at inclined GBs is considered using a coordinate transformation. The extreme incompatibility stresses for GBs with various inclination angles are explored with a simulated annealing method. The influence of GB inclination angle on the magnitude of incompatibility stress is systematically explored.

3.3 MODEL DESCRIPTION

We first consider the incompatibility stress for a GB fixed parallel to the XOZ plane under an arbitrary external stress σ^{E}. A schematic figure of the bicrystal model is shown as Fig. 3.1. The 3-dimensional space is divided into two semi-infinite half-spaces separated by the GB. The left (right) of the GB is grain I(II). The two grains consist of the same material.

The orientations of crystals can be conveniently described with Miller indices. For grain I,

$$\hat{\boldsymbol{e}}^{\mathrm{I}} = \begin{bmatrix} l_{\mathrm{x}}^{\mathrm{I}} & l_{\mathrm{y}}^{\mathrm{I}} & l_{\mathrm{z}}^{\mathrm{I}} \\ m_{\mathrm{x}}^{\mathrm{I}} & m_{\mathrm{y}}^{\mathrm{I}} & m_{\mathrm{z}}^{\mathrm{I}} \\ n_{\mathrm{x}}^{\mathrm{I}} & n_{\mathrm{y}}^{\mathrm{I}} & n_{\mathrm{z}}^{\mathrm{I}} \end{bmatrix}, \tag{3.1}$$

where $\boldsymbol{l}^{\mathrm{I}}$, $\boldsymbol{m}^{\mathrm{I}}$, $\boldsymbol{n}^{\mathrm{I}}$ are normalized Miller indices of the crystallographic orientation of

3
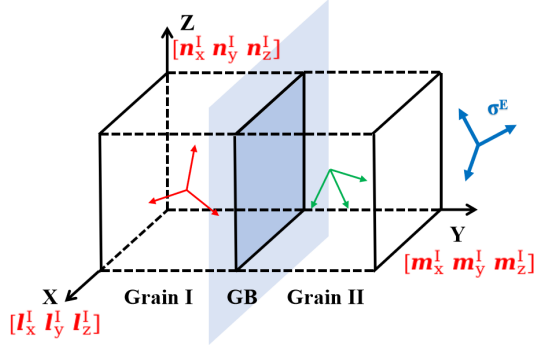
Figure 3.1: (Color online) Schematic figure of the bicrystal model. Grains I (II) on the left (right side) are separated by a GB perpendicular to the global Y-axis. The GB is infinitely extended in the X and Z directions. The orientation of each grain is represented by three vectors represented by Miller indices. The label of the grain is shown with a superscript. The external stress σ^{E} can be of any type.

grain I corresponding to X, Y, and Z-axis in the global coordinate system, respectively, and analogously for grain II.

Within the continuum description of GBs, the following constraints apply to the bicrystal model.

1. The two grains are rigidly glued together at the GB. No relative motion is allowed at the GB.

2. The model contains only one infinitely extended GB. The interaction between GBs is not included.

3. There is a linear relation between stress and strain.

With Voigt notation (xx $\to$ 1, yy $\to$ 2, zz $\to$ 3, yz $\to$ 4, xz $\to$ 5, xy $\to$ 6) with the engineering convention ($\varepsilon_4 = 2\varepsilon_{xy}$), the constitutive equation of linear elastic material is

$$
\begin{bmatrix} \varepsilon_1 \\ \varepsilon_2 \\ \varepsilon_3 \\ \varepsilon_4 \\ \varepsilon_5 \\ \varepsilon_6 \end{bmatrix}
=
\begin{bmatrix}
s_{11} & s_{12} & s_{13} & s_{14} & s_{15} & s_{16} \\
s_{12} & s_{22} & s_{23} & s_{24} & s_{25} & s_{26} \\
s_{13} & s_{23} & s_{33} & s_{34} & s_{35} & s_{36} \\
s_{14} & s_{24} & s_{34} & s_{44} & s_{45} & s_{46} \\
s_{15} & s_{25} & s_{35} & s_{45} & s_{55} & s_{56} \\
s_{16} & s_{26} & s_{36} & s_{46} & s_{56} & s_{66}
\end{bmatrix}
\begin{bmatrix} \sigma_1 \\ \sigma_2 \\ \sigma_3 \\ \sigma_4 \\ \sigma_5 \\ \sigma_6 \end{bmatrix}
\tag{3.2}
$$

Since there is no constraint on the shape of the compliance matrix, the model is valid for all crystal structures.

The discontinuity of a scalar field $g(x_i)$ at the GB is denoted as

$$
[[g]] = g^{\mathrm{I}} - g^{\mathrm{II}}. \tag{3.3}
$$

According to the first constraint listed above, strain components in the GB plane are continuous,

$$[[\varepsilon_i]] = 0, \quad i, j = 1, 3, 5. \tag{3.4}$$

Since σ^E is a far-field stress, global stress equilibrium requires

$$\frac{1}{V} \int_V \sigma_i dV = \sigma_i^E, \tag{3.5}$$

where σ^E is the applied external stress[26]. Since the model assumes that each grain occupies half the space,

$$\sigma_i^E = \frac{1}{2}(\sigma_i^I + \sigma_i^{II}). \tag{3.6}$$

The tractions on the GB must be continuous, and the difference at the GB must vanish (Eq. 3.3),

$$[[\sigma_i]] = 0, \quad i = 2, 4, 6. \tag{3.7}$$

σ^I and σ^{II} as function of σ^E for any GB can be calculated by solving Eqs. 4.1, 4.2, 3.6, and 3.7.

Eq. 3.7 shows that only in-plane components of incompatibility stress are non-zero. Then the stress states on both sides of the GB can be written as the superposition of σ^E and the additional stress field,

$$\begin{cases} \sigma^I = [\Delta\sigma_1 + \sigma_1^E, \sigma_2^E, \Delta\sigma_3 + \sigma_3^E, \sigma_4^E, \Delta\sigma_5 + \sigma_5^E, \sigma_6^E] \\ \sigma^{II} = [-\Delta\sigma_1 + \sigma_1^E, \sigma_2^E, -\Delta\sigma_3 + \sigma_3^E, \sigma_4^E, -\Delta\sigma_5 + \sigma_5^E, \sigma_6^E]. \end{cases} \tag{3.8}$$

The magnitudes of the three additional stress components, i.e. $\Delta\sigma_1$, $\Delta\sigma_3$, and $\Delta\sigma_5$, are influenced by the choice of the observation coordinate system. As is evident from the Mohr circle construction, $\Delta\sigma_5$ can be made to vanish by an appropriate rotation of the coordinate system while $\Delta\sigma_1$ and $\Delta\sigma_3$ cannot. In keeping consistency with Chapter 2, the incompatibility stress (IS) is defined as

$$IS = \Delta\sigma_1 + \Delta\sigma_3. \tag{3.9}$$

The advantage of the definition is that IS is directly connected with hydrostatic stress σ_h at both sides of GBs, which is independent of the reference coordinate system,

$$\begin{aligned} [[\sigma_h]] &= \frac{2(\Delta\sigma_1 + \Delta\sigma_3)}{3} \\ &= \frac{2}{3}IS. \end{aligned} \tag{3.10}$$

The problem is in the elastic limit, therefore IS induced by each stress component σ_i^{E} is linearly proportional to the magnitude of σ_i^{E}. For a uniaxial σ^{E}, which is common in applications, it is convenient to define incompatibility factor IF as

$$IF = \frac{IS}{\sigma^{\mathrm{E}}}. \tag{3.11}$$

3.4 Results and discussion

3.4.1 Approximation for incompatibility stress under arbitrary external stress in cubic crystals

The analytical solution shown in Section 2 is accurate but not intuitive. Here, an approximation for the incompatibility stress under arbitrary external stress is derived for cubic crystals.

In Chapter 2, the compliance tensor after rotation (see the Appendix A) is shown. The compliance tensor before (S, with Voigt notation) and after rotation (S') can be written as

$$S' = S + \chi F(l, m, n) \tag{3.12}$$

in which l, m, and n describe the rotation (see Eq. 3.1), F is a 6 by 6 matrix defined in Appendix B, while χ gives the anisotropy in the compliance of the material,

$$\chi = 2s_{11} - 2s_{12} - s_{44}. \tag{3.13}$$

Under σ_2^{E},

$$IS \approx \frac{2[[F_{22}]]\sigma_2^{\mathrm{E}}\chi}{(F_{22}^{\mathrm{I}} + F_{22}^{\mathrm{II}})\chi + 4s_{11} + 4s_{12}}, \tag{3.14}$$

with

$$F_{22} = -(m_{\mathrm{x}}^2 m_{\mathrm{y}}^2 + m_{\mathrm{x}}^2 m_{\mathrm{z}}^2 + m_{\mathrm{y}}^2 m_{\mathrm{z}}^2). \tag{3.15}$$

As our description is in the linear elastic limit, the superposition principle applies to IS, which means IS induced by each component of σ^E can be treated separately. With similar simplification, IS for arbitrary σ^E is estimated with superposition principle, as

$$IS_{approx} = \frac{2\sum_{i=1}^{6}[[F_{i2}]]\sigma_i^{\mathrm{E}}\chi}{(F_{22}^{\mathrm{I}} + F_{22}^{\mathrm{II}})\chi + 4s_{11} + 4s_{12}} \tag{3.16}$$

Noticing $(F_{22}^{\mathrm{I}} + F_{22}^{\mathrm{II}})$ approaches to $-\frac{1}{3}$ for configurations with high IS, Eq. 3.16 is further simplified as

$$IS_{approx} = \frac{6\chi}{10s_{11} + 14s_{12} + s_{44}} \sum_{i=1}^{6}[[F_{i2}]]\sigma_i^{\mathrm{E}} \tag{3.17}$$

The accuracy of Eq. 3.17 is illustrated in Fig. 3.2. For Al, Fe(BCC), Cu, and Li (in order of increasing elastic anisotropy), the IS obtained by Eq. 3.17 for 50000 arbitrarily oriented bicrystals under randomly chosen external stress states (each of the six stress components is randomly chosen in $[-1, 1]$) are compared with exact solutions to Eq. 3.9. The histograms at the top and right side of each scatter plot show the distributions of IS by analytical solution and by approximation, respectively. The mean absolute error (MAE) for each metal is shown in the figure.

3
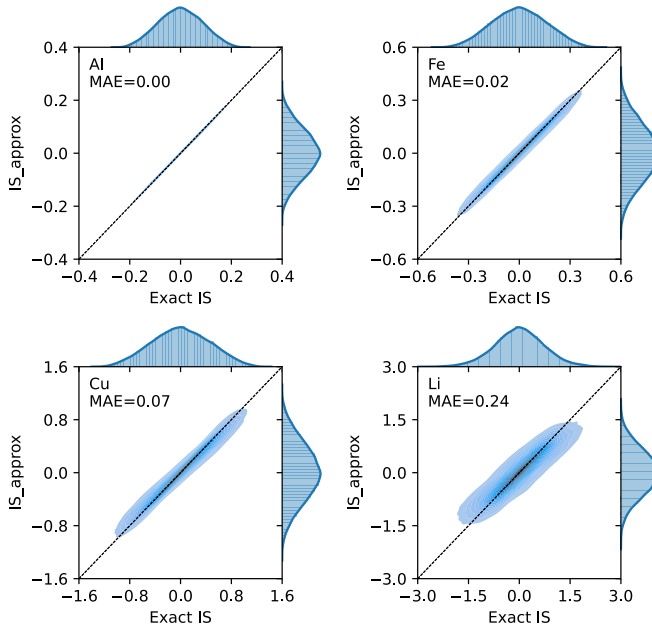
Figure 3.2: Comparison between incompatibility stress calculated exactly with Eq. 3.9 and estimated with Eq. 3.17 for Al, Fe (BCC), Cu, and Li (in the sequence of ascending anisotropy). The distribution of IS obtained exactly and approximately (Eq. 3.17) are presented in histograms at the top and right side of each scatter plot, respectively. Dashed lines are guides to the eye.

For Al, Fe (BCC), and Cu, the IS obtained by approximation (Eq.3.17) are in good agreement with the analytical results. For Li, the approximation underestimates the extreme value of IS. The extraordinarily high level of IS in materials with high anisotropy is further discussed in Section 3.3.

Eq.3.17 shows that the value of IS is controlled by three factors, i.e. the material elastic property (χ and compliance components), the difference of the orientations of the two grains ($[[F_{i2}]]$), and σ^E. That means that for a given σ^E, the configurations of the bicrystal that lead to extreme IS are the same for all cubic materials. Such is the case for uniaxial stress perpendicular to the GB where it could be proven

that the $< 100 >< 111 >$ GB gives the largest IS for all cubic materials. Conversely, one can also seek to determine which σ^{E} leads to the largest IS for a bicrystal with given orientations of the two grains using Eq.3.17. Particularly for polycrystals with strong textures, for which anisotropic mechanical properties are well documented [32, 33], it is promising to identify the relation between loading conditions and the distribution of IS at GBs.

3.4.2 Incompatibility stress in cubic crystals under hydrostatic external stress for bicrystal model

Here we prove hydrostatic external stress does not lead to incompatibility stress at the GB in the bicrystal model. The absence of hydrostatically induced incompatibility stresses in cubic materials can be intuitively derived from a *Gedankenexperiment*: Hydrostatically compressing a monocrystalline sphere with a cubic crystal structure causes a volume change only, without change of shape, irrespective of the grain's orientation. When two spheres with different orientations are cut in half and subsequently recombined to create a bicrystal sphere, no additional stress is necessary as the cut sections match perfectly. Consequently, hydrostatic stress does not induce IS in cubic crystals. It follows that in cubic crystals the deviatoric stress only causes IS. However, in lower symmetry crystal structures, e.g. hexagonal, hydrostatic external stress generally contributes to IS at GBs. A detailed proof is shown in Appendix D.

Since the stress state at GBs under hydrostatic stress can hardly be experimentally determined, there's no direct evidence for the findings. The molecular dynamics simulation of the segregation energy for several alloy systems by Zhang et al. [34] indirectly confirms our findings. In the simulation, hydrostatic stresses with the magnitude of 2 to 12 GPa were applied to polycrystal models, and the distributions of segregation energy were studied. The local atomic stress analysis showed that for Al-Mg, Al-Ni, and Ni-Nb alloys, the external hydrostatic stress level led to minor changes to the fraction of GB sites that were under a tensile stress state. Noticing the matrices of the alloys are all cubic crystals, the simulations match the analytical conclusion well.

3.4.3 Bicrystal model with inclined grain boundary under uniaxial external stress in cubic crystals

Assume the uniaxial external stress is along the global Y-axis, i.e. $\sigma^{\mathrm{E}} = [0, 1, 0, 0, 0, 0]$, the schematic figure for the bicrystal model with inclined GB is shown as Fig. 3.3. The two grains are semi-infinite and the model is still subject to the constraints described in Section 2. The orientation of the grain boundary is defined with θ, the angle between the GB normal n and the global Y-axis, and ϕ, the angle between the projection of $\vec{n}$ on XOZ plane and X-axis. Experimentally, the distribution of θ for

GBs in polycrystals can be measured, as one of the five parameters of GBs [23]. In Section 3.3, *IS* for a GB parallel to the XOZ plane under an arbitrary σ^E is derived. By defining a GB coordinate system in which the GB aligns to the local XOZ plane and representing the problem within the GB coordinate system, the stress state for an inclined GB can be solved with the same method.
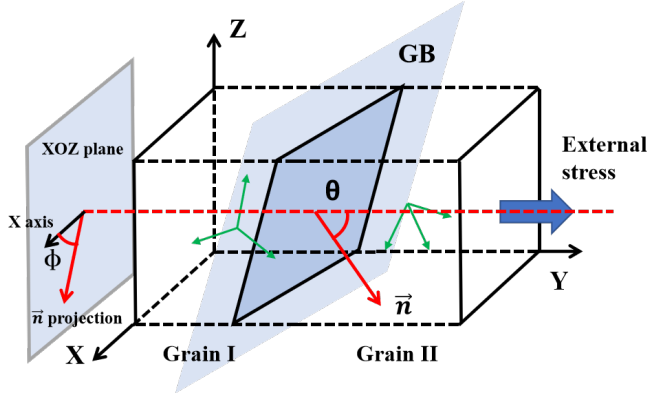
Figure 3.3: The schematic figure of the bicrystal model with inclined grain boundary under uniaxial external stress. The orientation of the grain boundary is defined with θ, the angle between the grain boundary normal $\vec{n}$ and the global Y-axis, and ϕ, the angle between the projection of $\vec{n}$ on the XOZ plane and X-axis.

The normal vector of GB plane $\vec{n}$ is uniquely represented as

$$[\sin\theta\cos\phi \quad \cos\theta \quad -\sin\theta\sin\phi].$$

Since there's no constraint on the choice of the other two basis vectors, for convenience, the GB coordinate system can be chosen as

$$Q = \begin{bmatrix} \sin\phi & 0 & \cos\phi \\ \sin\theta\cos\phi & \cos\theta & -\sin\theta\sin\phi \\ -\cos\theta\cos\phi & \sin\theta & \cos\theta\sin\phi \end{bmatrix}. \tag{3.18}$$

For a grain with orientation $\hat{e}$ defined in global coordinate system, the corresponding orientation $\hat{e}^{GB}$ in the GB coordinate system Q can be obtained by

$$\hat{e}^{GB} = Q\hat{e}. \tag{3.19}$$

For uniaxial external stress with a magnitude of σ^E along the global Y axis, the external stress acting on the GB plane $\sigma^{E,GB}$ is calculated as

$$\sigma^{E,GB} = Q \cdot \begin{bmatrix} 0 & 0 & 0 \\ 0 & \sigma^E & 0 \\ 0 & 0 & 0 \end{bmatrix} \cdot Q^T = \sigma^E \begin{bmatrix} 0 & 0 & 0 \\ 0 & \cos^2\theta & \sin\theta\cos\theta \\ 0 & \sin\theta\cos\theta & \sin^2\theta \end{bmatrix}. \tag{3.20}$$

From Eq. 3.20, $\sigma^{E,GB}$ is only controlled by θ, which ranges from 0 (GB perpendicular to the uniaxial external stress) to 90° (GB parallel to the uniaxial external stress). The second degree of freedom of the GB plane, ϕ, is included in the coordinate transformation of elastic tensors for the two grains(Eq. 3.19). IF_θ^{max} denotes the maximum IF over ϕ values for GBs with a specific inclination angle θ while IF_{max}^{max}, IF_{min}^{max} denotes the maximum and minimum IF for bicrystals for all θ values, respectively.

In Chapter 2, GBs perpendicular to the uniaxial external stress ($\theta = 0^o$) have been studied systematically. $IF_{\theta=0^o}^{max}$, the maximum incompatibility factor for GB with $\theta = 0^o$, was found as a function of elastic components,

$$
\begin{aligned}
IF_{\theta=0^o}^{max} &= \frac{4s_{11} - 4s_{12} - 2s_{44}}{10s_{11} + 14s_{12} + s_{44}} \\
&= \frac{-2(C_{11} - C_{12} - 2C_{44}(C_{11} + 2C_{12}))}{(10C_{11} - 4C_{12})C_{44} + (C_{11} - C_{12})(C_{11} + 2C_{12})}.
\end{aligned}
\tag{3.21}
$$

For several materials Eq. 3.21 yields negative $IF_{\theta=0^o}^{max}$. Since IF for a given bicrystal changes its sign when the two grains exchange the label, we use the absolute value to assess the magnitude of $IF_{\theta=0^o}^{max}$. For bicrystal with GB plane inclined by arbitrary θ, no analytical solution for IF_θ^{max} was found. For θ ranging from 0 to 90° with 1° increments, a simulated annealing approach was applied to search for the extreme value of IF for each θ. For several materials in cubic crystal (including metals, intermetallics, oxides, and carbides), the elastic components, Zener ratio ($A = \frac{2C_{44}}{C_{11} - C_{12}}$), $IF_{\theta=0^o}^{max}$, the θ corresponding to IF_{max}^{max} and IF_{min}^{max} are listed in Table 3.1, in a sequence of ascending $|IF_{\theta=0^o}^{max}|$.

To emphasize the influence of θ and to make various materials comparable, IF_θ^{max} is normalized by $|IF_{\theta=0^o}^{max}|$. Normalized IF_θ^{max} curves are shown as function of θ in Fig. 3.4.

Table. 3.1 and Fig. 3.4 clearly illustrate that cubic materials can be classified into three groups. Materials in each group have similar features of the distribution of IF_θ^{max}. The criteria and features of each group are listed as follows.

1. For materials with $|IF_{\theta=0^o}^{max}| < 0.7$, including metals, carbides, and oxides, IF_θ^{max} decreases when θ increases, IF_θ^{max} achieves its maximum when $\theta = 0^o$, while achieves its minimum at $\theta = 90^o$, as is shown in Fig. 3.4(a). The influence of θ on IF_θ^{max} is getting smaller with the increase of $IF_{\theta=0^o}^{max}$, which is contrary to intuition. For example, the relative variation of IF_θ^{max} for iron (BCC) is about 13% while the value for aluminum is 22%. In this group, the $IF_{\theta=0^o}^{max}$ for some materials are negative. These materials have slightly higher $IF_{\theta=90^o}^{max}$, comparing with materials with positive $IF_{\theta=0^o}^{max}$ of same magnitude.
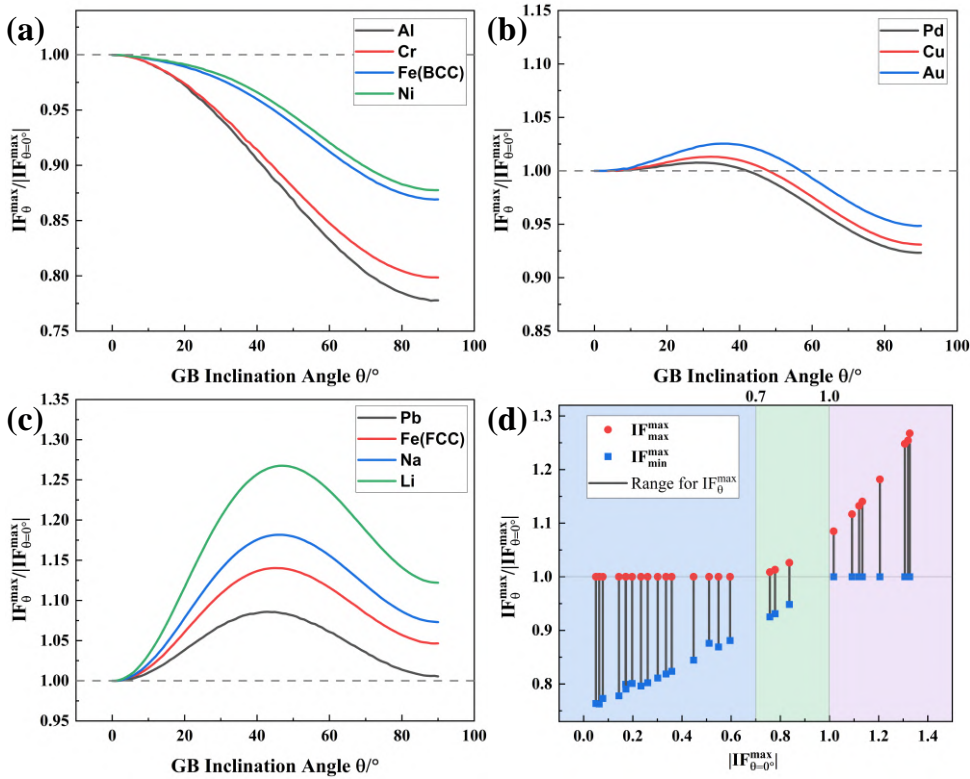
Figure 3.4: The variation of the maximum incompatibility factor IF_θ^{max} with respect to the grain boundary inclination angle θ for (a) materials with $|IF_{\theta=0^\circ}^{max}| < 0.7$; (b) materials with $0.7 \leq |IF_{\theta=0^\circ}^{max}| < 1.0$; (c) materials with $|IF_{\theta=0^\circ}^{max}| > 1.0$. Figure (d) shows the range of normalized IF_θ^{max} for all materials listed in Table 3.1. IF_θ^{max} is scaled by $|IF_{\theta=0^\circ}^{max}|$ (as is listed in Table 3.1) to emphasis the influence of θ.

2. For materials with medium anisotropy, i.e. $0.7 \leq |IF_{\theta=0^\circ}^{max}| < 1.0$, including Group 11 elements and Pd, IF_θ^{max} have small relative variation (about 10%) with respect to θ. IF_{max}^{max} is achieved for GB with about 32°, and IF_{min}^{max} is at $\theta = 90^\circ$, as is shown in Fig. 3.4(b).

3. For materials with high anisotropy, i.e. $IF_{\theta=0^\circ}^{max} > 1.0$, including lead, alkali metals, and polymorphic high-temperature stable phases for several metals, IF_θ^{max} significantly rises when θ rises from 0° to about 45°, as is shown in Fig. 3.4(c). IF^{max} is achieved when θ is $43^\circ - 47^\circ$. For these materials, the difference of IF_θ^{max} with the variation of θ is amplified by their high $IF_{\theta=0^\circ}^{max}$.

Also, we notice $|IF_{\theta=0^\circ}^{max}|$ is a good indicator for the classification of materials, compared with the Zener ratio. For given elastic components, $|IF_{\theta=0^\circ}^{max}|$ calculated

from Eq. 3.21 can properly predicts the shape of $IF_\theta^{\max}$, as well as the approximate range for $IF_\theta^{\max}$, as is shown in Fig. 3.4(d).

The configurations of the bicrystal (i.e. the orientations of the two grains and the GB plane) in the global coordinate system corresponding to $IF_\theta^{\max}$ are also of concern. For θ less than 10°, the problem is similar to bicrystals with GB fixed perpendicular to the uniaxial σ^{E}. It is found that IF for GBs which have two grains with crystallographic orientation of $\langle 100 \rangle$ and $\langle 111 \rangle$ along the direction of σ^{E} in the global coordinate system, respectively, are close to $IF_\theta^{\max}$. Configurations that correspond to $IF_{\max}^{\max}$ and $IF_{\min}^{\max}$ are obtained with a simulated annealing method, as is listed in Table 3.2. Since exact θ and configurations for $IF^{\max}$ are not the same for materials with medium to high anisotropy, the configurations given in the list are good approximations of the exact orientations.

For two grains with orientations given in Table. 3.2, keep θ varying from 0° to 90° and $\phi = 0^{\mathrm{o}}$, IF for three typical metals are shown in Fig. 3.5. It can be observed that even for a bicrystal system with only one degree of freedom (i.e. θ), IF could vary in a wide range. Curves shown in Fig. 3.4 are the upper envelopes of IF curves for all possible configurations of the bicrystal with different material properties.

Song et al.[48] studied the relation between intergranular stress concentration and GB orientations in Ni-based superalloy statistically by microscopic characterizations, and found that GB inclination angle has little influence on the stress concentration tendency. The necessity of two degrees of freedom for GB orientation in the determination of IF explains why the microscopic characterization (which generally shows cut lines of GB planes) failed to reveal the influence of GB orientation on stress concentration.

The value of IS indicates stress discontinuity and stress concentration, as described in Eq. 3.10. A direct application of the hydrostatic stress at GBs is the segregation tendency. Both Monte Carlo simulation [49] and crystal plasticity FEM [50] confirmed the profound influence of local hydrostatic stress on the segregation tendency. Jothi et al.[51] studied the hydrogen re-distribution near $\langle 001 \rangle$ tilt GBs induced by the incompatibility stress with the aim to identify GBs with low hydrogen concentration tendency in nickel. In this work, a wide range of GB configurations and stresses were analyzed to relate the relative magnitude of IF to the inclination of GBs. The value of $IF_\theta^{\max}$ and its variation with respect to θ for cubic crystals presented here can provide insights for segregation engineering[52].
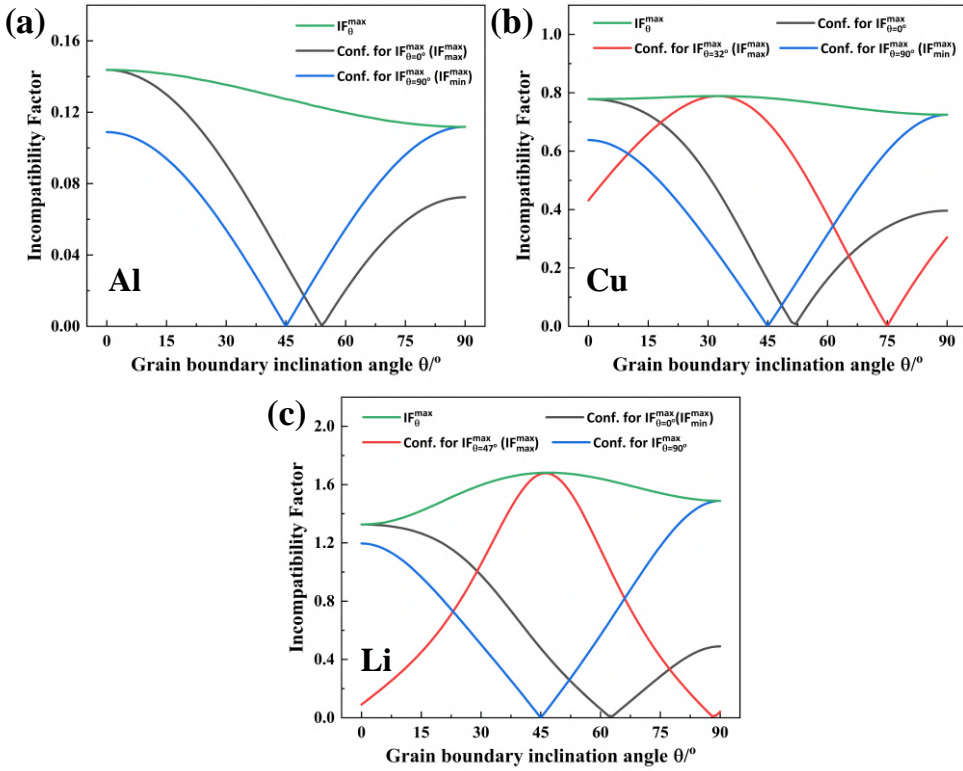
Figure 3.5: The variation of IF as a function of the grain boundary inclination angle for special configurations ($IF_{\max}^{\max}$, $IF_{\min}^{\max}$, $IF_{\theta=0°}^{\max}$, and $IF_{\theta=90°}^{\max}$) for three typical material: (a) low-anisotropy material Al; (b) medium-anisotropy material Cu; and (c) high-anisotropy material Li. Curves for $IF_{\theta}^{\max}$, as the upper envelope of IF curves for all possible configurations of the bicrystal, are also presented.

3

Material	C_{11}	C_{12}	C_{44}	A	$IF_{\theta=0°}^{\max}$	Range of $IF_{\theta}^{\max}$	θ for $IF_{\max}^{\max}$	θ for $IF_{\min}^{\max}$
Unit	GPa	GPa	GPa		Dimensionless		Degree	
W [35]	523.0	203.0	160.0	1.00	0.0	0.0	–	–
TiC [36]	500.0	113.0	175.0	0.90	-0.0499	[0.0381, 0.0499]		
Fe$_3$O$_4$ [37]	275.0	104.0	95.5	1.12	0.0632	[0.0482, 0.0632]		
ZrC [38]	472.0	98.7	159.3	0.85	-0.0780	[0.0603, 0.0780]		
Al [35]	108.0	62.0	28.3	1.23	0.1437	[0.1118, 0.1437]		
Cr [35]	348.0	67.0	100.0	0.71	-0.1710	[0.1367, 0.1710]		
V [35]	230.0	120.0	43.1	0.78	-0.1719	[0.1359, 0.1719]		
Mo [35]	465.0	163.0	109.0	0.72	-0.1970	[0.1578, 0.1970]		
Si [35]	165.0	63.0	79.1	1.55	0.2332	[0.1857, 0.2332]	0	90
Ir [35]	600.0	260.0	270.0	1.59	0.2605	[0.2090, 0.2605]		
Ta [35]	264.0	158.0	82.6	1.56	0.3013	[0.2444, 0.3013]		
GaAs [39]	118.8	53.7	59.4	1.82	0.3349	[0.2742, 0.3349]		
Pt [40]	347.0	251.0	76.5	1.59	0.3583	[0.2951, 0.3583]		
MgAl$_2$O$_4$ [41]	298.6	153.7	157.6	2.18	0.4472	[0.3777, 0.4472]		
Nb [35]	245.0	132.0	28.4	0.50	-0.5104	[0.4471, 0.5104]		
Fe(BCC) [35]	230.0	135.0	117.0	2.46	0.5485	[0.4767, 0.5485]		
Ni [35]	247.0	153.0	122.0	2.60	0.5954	[0.5246, 0.5954]		
Pd [35]	221.0	171.0	70.8	2.83	0.7573	[0.7007, 0.7639]	30	
Cu [35]	169.0	122.0	75.3	3.20	0.7785	[0.7247, 0.7888]	32	90
Ag [35]	122.0	92.0	45.5	3.03	0.7786	[0.7251, 0.7887]	32	
Au [35]	191.0	162.0	42.2	2.91	0.8368	[0.7936, 0.8588]	36	
Pb [35]	48.8	41.4	14.8	4.00	1.0170	[1.0170, 1.1033]	43	
NiTi(B2) [42]	175.0	153.0	48.0	4.36	1.0917	[1.0917, 1.2191]	45	
Ti(BCC) [43]	97.7	82.7	37.5	5.00	1.1204	[1.1204, 1.2686]	46	
Fe(FCC) [44]	188.0	156.0	87.0	5.44	1.1335	[1.1335, 1.2926]	46	0
Na [35]	7.6	6.3	4.3	6.62	1.2052	[1.2052, 1.4242]	47	
K [45]	3.7	3.2	1.9	7.60	1.3063	[1.3063, 1.6303]	47	
Zr(BCC) [46]	104.0	93.0	38.0	6.91	1.3194	[1.3194, 1.6548]	47	
Li [47]	13.4	11.3	9.6	9.14	1.3266	[1.3266, 1.6816]	47	

Table 3.1: Elastic components (C_{11}, C_{12}, and C_{44}), anisotropy indicator (Zener ratio A and $IF_{\theta=0°}^{\max}$), the range of $IF_{\theta}^{\max}$ and the grain boundary inclination angle θ corresponding to the maximum and minimum of $IF_{\theta}^{\max}$ for common cubic materials. The materials are listed in a sequence of ascending elastic anisotropy and divided into three groups according to the magnitude of their $IF_{\theta}^{\max}$.

3

Anisotropy	Orientations for $IF_{\max}^{\max}$		Orientations for $IF_{\min}^{\max}$	
	Grain I	Grain II	Grain I	Grain II
$-0.7 < IF_{\theta=0^{\circ}}^{\max} < 0$	$\boldsymbol{m}^{\mathrm{I}} = \frac{1}{\sqrt{3}}\langle 1\ 1\ 1\rangle$	$\boldsymbol{m}^{\mathrm{II}} = \langle 1\ 0\ 0\rangle$	$\boldsymbol{l}^{\mathrm{I}}=[0\ 1\ 0]$ $\boldsymbol{m}^{\mathrm{I}}=\frac{1}{\sqrt{2}}[1\ 0\ 1]$	$\boldsymbol{l}^{\mathrm{II}}=\frac{1}{\sqrt{2}}[1\ 0\ -1]$ $\boldsymbol{m}^{\mathrm{II}}=\frac{1}{\sqrt{2}}[1\ 0\ 1]$
$0 < IF_{\theta=0^{\circ}}^{\max} < 0.7$			$\boldsymbol{l}^{\mathrm{I}}=\frac{1}{\sqrt{2}}[1\ 0\ 1]$ $\boldsymbol{m}^{\mathrm{I}}=\frac{1}{\sqrt{2}}[1\ 0\ -1]$	$\boldsymbol{l}^{\mathrm{II}}=\frac{1}{\sqrt{2}}[1\ 0\ 1]$ $\boldsymbol{m}^{\mathrm{II}}=[0\ 1\ 0]$
$0.7 \leq IF_{\theta=0^{\circ}}^{\max} < 1.0$	$\boldsymbol{l}^{\mathrm{I}}=\frac{1}{\sqrt{37}}[6\ 0\ -1]$ $\boldsymbol{m}^{\mathrm{I}}=\frac{1}{\sqrt{37}}[-1\ 0\ -6]$	$\boldsymbol{l}^{\mathrm{II}}=\frac{1}{\sqrt{14}}[\sqrt{5}\ \sqrt{5}\ 2]$ $\boldsymbol{m}^{\mathrm{II}}=\frac{1}{\sqrt{7}}[1\ 1\ -\sqrt{5}]$		
$IF_{\theta=0^{\circ}}^{\max} \geq 1.0$	$\boldsymbol{l}^{\mathrm{I}}=\frac{1}{\sqrt{26}}[5\ 1\ 0]$ $\boldsymbol{m}^{\mathrm{I}}=\frac{1}{\sqrt{26}}[-1\ 5\ 0]$	$\boldsymbol{l}^{\mathrm{II}}=\frac{1}{\sqrt{54}}[-5\ 5\ -2]$ $\boldsymbol{m}^{\mathrm{II}}=\frac{1}{\sqrt{27}}[-1\ 1\ 5]$	$\boldsymbol{m}^{\mathrm{I}} = \frac{1}{\sqrt{3}}\langle 1\ 1\ 1\rangle$	$\boldsymbol{m}^{\mathrm{II}} = \langle 1\ 0\ 0\rangle$

Table 3.2: The orientations for the bicrystal with varying anisotropy to achieve $IF_{\max}^{\max}$ and $IF_{\min}^{\max}$. $\boldsymbol{l}$ and $\boldsymbol{m}$ are the Miller indices along the global X- and Y-axis, respectively. θ, the inclination angle of the grain boundary plane, is given in Table 3.1. ϕ, the second degree of freedom of the grain boundary plane, is fixed as 0° for all the configurations.

3.5 Conclusion

This work examines the difference of stress states on both sides of GBs under arbitrary external stress in linear elastic cubic materials with a bicrystal model. For linear elasticity, there is a proportionality between the additional normal stress at GBs and the applied uniaxial stress. We define the ratio of the additional normal stress at GBs over the applied uniaxial stress as the incompatibility factor(IF). The variation of $IF_\theta^{\max}$, the highest IF for a GB with an inclination angle θ and two grains with arbitrary orientations, is explored systematically. The following conclusions are obtained:

1. The incompatibility stress for GB under external applied stress σ^{E} can be estimated with

$$IS_{approx} = \frac{6\chi}{10s_{11} + 14s_{12} + s_{44}} \sum_{i=1}^{6} [[F_{i2}]]\sigma_i^{\mathrm{E}}, \tag{3.22}$$

   where s_{11}, s_{12}, s_{44}, and $\chi = 2s_{11} - 2s_{12} - s_{44}$ show the influence of the material elastic property while the $[[F_{i2}]]$ show the influence of the orientations of the two grains.

2. For cubic crystals, hydrostatic external stress does not induce any incompatibility stress at GBs. The incompatibility stress is caused by the deviatoric stress only.

3. The anisotropy of cubic materials is evaluated with $IF_{\theta=0^\circ}^{\max}$, which is a simple function of s_{11}, s_{12}, and s_{44}. $IF_{\theta=0^\circ}^{\max}$ is somewhat correlated with the Zener anisotropy A or the universal elastic anisotropy index [53]. Cubic materials are classified into three groups according to the magnitude of $IF_{\theta=0^\circ}^{\max}$. Materials within each group share that the most extreme incompatibility stress occurs for 1) the same grain boundary inclination angle with respect to the direction of the σ^{E}, 2) the same bicrystal grain orientations, and 3) display the same variation of the incompatibility stress with respect to the inclination angle.

4. Only materials with small $IF_{\theta=0^\circ}^{\max}$ values (and small Zener anisotropy A), exhibit the highest additional stress at GBs which are perpendicular to the uniaxial σ^{E}. More anisotropic cubic materials exhibit the highest additional stress at inclined GBs.

5. $IF_\theta^{\max}$ for materials with high anisotropy, such as alkali metals and polymorphic high-temperature phases [NiTi(B2), Fe(FCC), and Ti(BCC)], are the most affected by θ. These materials would have the highest additional stress at GBs with 47° inclination with respect to the uniaxial σ^{E}.

Appendix D Incompatibility stress under hydrostatic external stress

Chapter 2 showed that the compliance tensor after rotation (S', with Voigt notation) can be written as

$$S' = \begin{bmatrix} s_{11} + F_{11}\chi & s_{12} + F_{12}\chi & s_{12} + F_{13}\chi & F_{14}\chi & F_{15}\chi & F_{16}\chi \\ & s_{11} + F_{22}\chi & s_{12} + F_{23}\chi & F_{24}\chi & F_{25}\chi & F_{26}\chi \\ & & s_{11} + F_{33}\chi & F_{34}\chi & F_{35}\chi & F_{36}\chi \\ & & & s_{44} + F_{44}\chi & F_{45}\chi & F_{46}\chi \\ & symmetric & & & s_{44} + F_{55}\chi & F_{56}\chi \\ & & & & & s_{44} + F_{66}\chi \end{bmatrix}$$

$$(D.1)$$

where F_{ij} are polynomials of l, m, n, as

$$F_{11} = -(l_x^2 l_y^2 + l_x^2 l_z^2 + l_y^2 l_z^2) \tag{D.2}$$

$$F_{12} = -(m_x m_y l_x l_y + m_x m_z l_x l_z + m_y m_z l_y l_z) \tag{D.3}$$

$$F_{22} = -(m_x^2 m_y^2 + m_x^2 m_z^2 + m_y^2 m_z^2) \tag{D.4}$$

$$F_{13} = -(n_x n_y l_x l_y + n_x n_z l_x l_z + n_y n_z l_y l_z) \tag{D.5}$$

$$F_{23} = -(n_x n_y m_x m_y + n_x n_z m_x m_z + n_y n_z m_y m_z) \tag{D.6}$$

$$F_{33} = -(n_x^2 n_y^2 + n_x^2 n_z^2 + n_y^2 n_z^2) \tag{D.7}$$

Under hydrostatic external stress, the strain for a rotated grain is

$$\varepsilon^H = S' \begin{bmatrix} \sigma^H \\ \sigma^H \\ \sigma^H \\ 0 \\ 0 \\ 0 \end{bmatrix} = \sigma^H \begin{bmatrix} s_{11} + 2s_{12} + \chi(F_{11} + F_{12} + F_{13}) \\ s_{11} + 2s_{12} + \chi(F_{21} + F_{22} + F_{23}) \\ s_{11} + 2s_{12} + \chi(F_{31} + F_{32} + F_{33}) \\ 0 \\ 0 \\ 0 \end{bmatrix}. \tag{D.8}$$

Considering the orthonormality of $\boldsymbol{l}$, $\boldsymbol{m}$, and $\boldsymbol{n}$ of $\hat{\boldsymbol{e}}$,

$$\begin{aligned} F_{11} + F_{12} + F_{13} = & -[(l_x l_y + m_x m_y + n_x n_y)l_x l_y + \\ & (l_x l_z + m_x m_z + n_x n_z)l_x l_z + \\ & (l_y l_z + m_y m_z + n_y n_z)l_y l_z] \\ = & -(0 \cdot l_x l_y + 0 \cdot l_x l_z + 0 \cdot l_y l_z) \\ = & 0. \end{aligned} \tag{D.9}$$

Analogously it can be proven (see Eq.A. 2-5) that

$$F_{i1} + F_{i2} + F_{i3} = 0, \quad i = 1, ..., 6. \tag{D.10}$$

Then the strain

3

$$\varepsilon^H = \sigma^H \begin{bmatrix} s_{11} + 2s_{12} \\ s_{11} + 2s_{12} \\ s_{11} + 2s_{12} \\ 0 \\ 0 \\ 0 \end{bmatrix} \tag{D.11}$$

for cubic crystals with arbitrary orientations and does not vary under rotation. Therefore there is no strain incompatibility between two crystals that are rotated relative to one another. Hence, there is no incompatibility stress either.

REFERENCES

[1] N. E. B. Cowern. Diffusion in a single crystal within a stressed environment. *Phys. Rev. Lett.*, 99(15):1–4, 2007.

[2] Dmitrii N. Ilin, Nicolas Saintier, Jean-Marc Olive, Remi Abgrall, and Isabelle Aubert. Simulation of hydrogen diffusion affected by stress-strain heterogeneity in polycrystalline stainless steel. *Int. J. Hydrogen Energy*, 39(5):2418–2422, February 2014.

[3] Hamidreza Abdolvand. Progressive modelling and experimentation of hydrogen diffusion and precipitation in anisotropic polycrystals. *Int. J. Plast.*, 116:39–61, May 2019.

[4] Pavel Lejček and Siegfried Hofmann. Thermodynamics and structural aspects of grain boundary segregation. *Crit. Rev. Solid State Mater. Sci.*, 20(1):1–85, 1995.

[5] Xiao Zhou and Jun Song. Effect of local stress on hydrogen segregation at grain boundaries in metals. *Mater. Lett.*, 196:123–127, June 2017.

[6] F. Fischer, G. Schmitz, and S. M. Eich. A systematic study of grain boundary segregation and grain boundary formation energy using a new copper–nickel embedded-atom potential. *Acta Mater.*, 176:220–231, September 2019.

[7] J. Chen and S. J. Fensin. Associating damage nucleation and distribution with grain boundary characteristics in Ta. *Scr. Mater.*, 187:329–334, October 2020.

[8] N. J. Teng and T. H. Lin. Elastic anisotropy effect of crystals on polycrystal fatigue crack initiation. *J. Eng. Mater. Technol.*, 117(4):470–477, 1995.

[9] H. Vehoff, A. Nykyforchyn, and R. Metz. Fatigue crack nucleation at interfaces. *Mater. Sci. Eng. A*, 387-389(1-2 SPEC. ISS.):546–551, 2004.

[10] Michael D. Sangid, Hans J. Maier, and Huseyin Sehitoglu. The role of grain boundaries on fatigue crack initiation - an energy approach. *Int. J. Plast.*, 27(5):801–821, 2011.

[11] L. L. Li, P. Zhang, Z. J. Zhang, and Z. F. Zhang. Effect of crystallographic orientation and grain boundary character on fatigue cracking behaviors of coaxial copper bicrystals. *Acta Mater.*, 61(2):425–438, 2013.

[12] Zhefeng Zhang, Linlin Li, Zhenjun Zhang, and Peng Zhang. Twin boundary: Controllable interface to fatigue cracking. *J. Mater. Sci. Technol.*, 33(7):603–606, 2017.

[13] Xiaoqing Song, Yongxin Wang, Jing Zhang, Yanli Lu, Yifan Wang, and Zheng Chen. The formation of intragranular stress concentration in plastic deformed Ni-base superalloy: Governing factors and process. *Mater. Sci. Eng. A*, 806:140820, 2021.

[14] W. W. Sun, H. Fang, N. H. van Dijk, S. van der Zwaag, and C. R. Hutchinson. Linking surface precipitation in Fe-Au alloys to its self-healing potential during creep loading. *Metall. Mater. Trans. B*, 48(5):2109–2114, 2017.

[15] J. D. Hu, F. Z. Xuan, C. J. Liu, and B. Chen. Modelling of cavity nucleation under creep-fatigue interaction. *Mech. Mater.*, 156(January):103799, 2021.

[16] Elaine A. West, Michael D. McMurtrey, Zhijie Jiao, and Gary S. Was. Role of localized deformation in irradiation-assisted stress corrosion cracking initiation. *Metall. Mater. Trans. A*, 43(1):136–146, 2012.

[17] D. An, T.A. Griffiths, P. Konijnenberg, S. Mandal, Z. Wang, and S. Zaefferer. Correlating the five parameter grain boundary character distribution and the intergranular corrosion behaviour of a stainless steel using 3D orientation microscopy based on mechanical polishing serial sectioning. *Acta Mater.*, 156:297–309, September 2018.

[18] Zilong Zhang, Shuang Xia, Qin Bai, Tingguang Liu, Hui Li, Bangxin Zhou, Linjun Wang, and Wujiang Ma. Effects of 3-D grain boundary geometrical angles and the net normal stress on intergranular stress corrosion cracking initiation in a 316 stainless steel. *Mater. Sci. Eng. A*, 765:138277, 2019.

[19] Tomoyuki Fujii, Tatsuro Sawada, Keiichiro Tohgo, and Yoshinobu Shimamura. Mechanical criterion for nucleation of intergranular stress corrosion cracking in austenitic stainless steel. *Forces Mech.*, 3:100013, September 2021.

[20] G Reisner, EA Werner, and FD Fischer. Micromechanical modeling of martensitic transformation in random microstructures. *Int. J. Solids Struct.*, 35(19):2457–2473, 1998.

[21] Amer Malik, Gustav Amberg, Annika Borgenstam, and John Ågren. Effect of external loading on the martensitic transformation–a phase field study. *Acta Mater.*, 61(20):7868–7880, 2013.

[22] P Sedmák, J Pilch, L Heller, J Kopeček, J Wright, P Sedlák, M Frost, and P Šittner. Grain-resolved analysis of localized deformation in nickel-titanium wire under tensile load. *Science*, 353(6299):559–562, 2016.

[23] David M Saylor, Bassem S El-Dasher, Brent L Adams, and Gregory S Rohrer. Measuring the five-parameter grain-boundary distribution from observations of planar sections. *Metall. Mater. Trans. A*, 35:1981–1989, 2004.

[24] Kouichi Maruyama. Effect of plastic strain incompatibility on 0.1% proof stresses of zinc bicrystals. *Trans. Jpn. Inst. Met.*, 22(No.10):723–732, 1981.

[25] Li Chingshen and T. Bretheau. The role of grain boundary compatibility in fatigue cracking of aluminum bicrystals. *Acta Metall.*, 37(10):2645–2650, 1989.

[26] T. Richeton and S. Berbenni. Effects of heterogeneous elasticity coupled to plasticity on stresses and lattice rotations in bicrystals: A field dislocation mechanics viewpoint. *Eur. J. Mech. A Solids*, 37:231–247, 2013.

[27] T. Richeton, I. Tiba, S. Berbenni, and O. Bouaziz. Analytical expressions of incompatibility stresses at $\Sigma 3 < 111 >$ twin boundaries and consequences on single-slip promotion parallel to twin plane. *Philos. Mag.*, 95(1):12–31, 2015.

[28] S. El Shawish and T. Mede. Grain boundary stresses in elastic materials. *Eur. J. Mech. A Solids*, 99:104940, May 2023.

[29] Masayuki Kamaya, Yoshihiro Kawamura, and Takayuki Kitamura. Three-dimensional local stress analysis on grain boundaries in polycrystalline material. *Int. J. Solids Struct.*, 44(10):3267–3277, 2007.

[30] J Hure, S El Shawish, L Cizelj, and B Tanguy. Intergranular stress distributions in polycrystalline aggregates of irradiated stainless steel. *J. Nucl. Mater.*, 476:231–242, 2016.

[31] Sheng Zhang, Leyun Wang, Gaoming Zhu, Martin Diehl, Alireza Maldar, Xiaoqing Shang, and Xiaoqin Zeng. Predicting grain boundary damage by machine learning. *Int. J. Plast.*, 150(December 2021):103186, 2022.

[32] S. H Choi, J. C Brem, F Barlat, and K. H Oh. Macroscopic anisotropy in AA5019A sheets. *Acta Mater.*, 48(8):1853–1863, May 2000.

[33] P. K. C. Venkatsurya, R. D. K. Misra, M. D. Mulholland, M. Manohar, and J. E. Hartmann. The impact of microstructure on yield strength anisotropy in linepipe steels. *Metall. Mater. Trans. A*, 45(5):2335–2342, May 2014.

[34] Zuoyong Zhang and Chuang Deng. Hydrostatic pressure-induced transition in grain boundary segregation tendency in nanocrystalline metals. *Scr. Mater.*, 234:115576, September 2023.

[35] A. G. Every and A. K. McCurdy. Second and higher order elastic constants, Landolt-Börnstein - Group III Volume 29A, 1992.

[36] JJ Gilman and BW Roberts. Elastic constants of TiC and TiB_2. *J. Appl. Phys.*, 32(7):1405–1405, 1961.

[37] MS Doraiswami. Elastic constants of magnetite, pyrite and chromite. *Proc. Indian Acad. Sci. Sect. A*, 25(5):413, 1947.

[38] Roger Chang and Lloyd J Graham. Low-temperature elastic properties of ZrC and TiC. *J. Appl. Phys.*, 37(10):3778–3783, 1966.

[39] HJ McSkimin, A Jayaraman, and P Andreatch Jr. Elastic moduli of GaAs at moderate pressures and the evaluation of compression to 250 kbar. *J. Appl. Phys.*, 38(5):2362–2364, 1967.

[40] RE MacFarlane, JA Rayne, and CK Jones. Temperature dependence of elastic moduli of iridium. *Phys. Lett.*, 20(3):234–235, 1966.

[41] Edward Schreiber. Elastic moduli of single-crystal spinel at 25 ^{o}C and to 2 kbar. *J. Appl. Phys.*, 38(6):2508–2511, 1967.

[42] Maarten De Jong, Wei Chen, Thomas Angsten, Anubhav Jain, Randy Notestine, Anthony Gamst, Marcel Sluiter, Chaitanya Krishna Ande, Sybrand Van Der Zwaag, Jose J Plata, et al. Charting the complete elastic properties of inorganic crystalline compounds. *Sci. data*, 2(1):1–13, 2015.

[43] Hassel Ledbetter, Hirotsugu Ogi, Satoshi Kai, Sudook Kim, and Masahiko Hirao. Elastic constants of body-centered-cubic titanium monocrystals. *J. Appl. Phys.*, 95(9):4642–4644, 2004.

[44] Jürgen Neuhaus, Michael Leitner, Karl Nicolaus, Winfried Petry, Bernard Hennion, and Arno Hiess. Role of vibrational entropy in the stabilization of the high-temperature phases of iron. *Phys. Rev. B*, 89(18):184302, 2014.

[45] PA Smith and Charles S Smith. Pressure derivatives of the elastic constants of potassium. *J. Phys. Chem. Solids*, 26(2):279–289, 1965.

[46] A Heiming, W Petry, J Trampenau, M Alba, Chr Herzig, HR Schober, and G Vogl. Phonon dispersion of the bcc phase of group-IV metals. ii. bcc zirconium, a model case of dynamical precursors of martensitic transitions. *Phys. Rev. B*, 43(13):10948, 1991.

[47] Harry C Nash and Charles S Smith. Single-crystal elastic constants of lithium. *J. Phys. Chem. Solids*, 9(2):113–118, 1959.

[48] Xiaoqing Song, Yongxin Wang, Jing Zhang, Yanli Lu, Yifan Wang, and Zheng Chen. The formation of intragranular stress concentration in plastic deformed Ni-base superalloy: Governing factors and process. *Mater. Sci. Eng. A*, 806:140820, March 2021.

[49] Y. Purohit, S. Jang, D. L. Irving, C. W. Padgett, R. O. Scattergood, and D. W. Brenner. Atomistic modeling of the segregation of lead impurities to a grain boundary in an aluminum bicrystalline solid. *Mater. Sci. Eng. A*, 493(1):97–100, October 2008.

[50] Kaidi Li, Bin Tang, Mengqi Zhang, Liguo Zhao, Xudong Liu, Jiangkun Fan, and Jinshan Li. A hydrogen diffusion model considering grain boundary characters based on crystal plasticity framework. *Int. J. Plast.*, 169:103740, October 2023.

[51] Sathiskumar Jothi, T. N. Croft, and S. G. R. Brown. Influence of grain boundary misorientation on hydrogen embrittlement in bi-crystal nickel. *Int. J. Hydrogen Energy*, 39(35):20671–20688, December 2014.

[52] D. Raabe, M. Herbig, S. Sandlöbes, Y. Li, D. Tytko, M. Kuzmina, D. Ponge, and P. P. Choi. Grain boundary segregation engineering in metallic alloys: A pathway to the design of interfaces. *Curr. Opin. Solid. State. Mater. Sci.*, 18(4):253–261, August 2014.

[53] Shivakumar I. Ranganathan and Martin Ostoja-Starzewski. Universal elastic anisotropy index. *Phys. Rev. Lett.*, 101(5):3–6, 2008.

4

Anisotropy on plasticity for pearlite: a molecular dynamics study informed by the periodic bicrystal model

4.1 Abstract

Cold-drawn pearlite wire is widely used in industry due to its exceptional high strength. Understanding the deformation mechanisms during the cold-drawing process of pearlite, particularly the deformation and decomposition of cementite, is of great significance. In this study, a bicrystal model tailored to lamellar structures is developed to calculate the elastic properties and stress concentration of pearlite. By analyzing slip activation in both ferrite and cementite, along with the yield strength, we reveal the significant influence of loading direction on pearlite deformability. Notably, the yield strength varies from 9.5 GPa to 17.0 GPa. Under specific loading conditions, plastic deformation is observed to initiate in cementite, challenging the conventional assumption that slip bands always originate in ferrite. Furthermore, factors that influence the plastic deformation of pearlite are discussed. A successive strengthening mechanism is proposed to explain the excellent deformability and high strength of pearlite after extensive deformation.

This work introduces a novel method for directional loading of lamellar structures. The surprising finding that plastic deformation, without fracture, can initiate in cementite, might offer directions for developing other structural materials with extreme tensile strength and deformability.

4.2 Introduction

Pearlite is a eutectoid steel microstructure with a lamellar morphology composed of ductile ferrite (α-phase) and brittle cementite (θ-phase). For pearlite obtained from the eutectoid transformation, the volume ratio of the two phases, V_α/V_θ, is approximately 8. After heavy cold-drawing deformation, pearlite can reach strengths up to 7 GPa, approaching the theoretical strength of steel [1]. During the cold drawing process, the inter-lamellar spacing decreases [2], dislocation density increases, and cementite lamellae gradually decompose. Supersaturated carbon atoms released from cementite dissolve into the ferrite lattice, causing significant lattice distortion [3]. This synergistic combination of dislocation strengthening, solid solution strengthening, and grain refinement is regarded as the primary mechanism behind the ultrahigh strength of pearlite [4, 5]. Understanding the structural evolution of pearlite and the critical role of cementite decomposition during drawing is crucial for optimizing its engineering performance.

Bulk cementite is generally considered a brittle ceramic with low fracture toughness [6, 7]. Its plastic deformation has been observed in limited scenarios, such as nano-indentation [8], compression [9], and multi-pass sliding wear [10]. The dislocation patterns in cementite were characterized in several early studies [11, 12]. The plasticity of cementite is sensitive to temperature [9, 11]. Terashima et al. showed that under compression, 2% plastic deformation was achievable at 573 K,

while brittle fracture dominated at room temperature [9].

In pearlite, where cementite is embedded in ferrite, its deformation behavior becomes more complex. Zhang et al. [2] observed cementite lamellae rotating, thinning, and fracturing during drawing of pearlite. The slip bands in cementite were found to be parallel to ferrite slip planes, suggesting slip initiation in ferrite followed by transfer to cementite. Zhou et al. [13] reported a transition in cementite from single crystalline to nanocrystalline and, eventually, to an amorphous state during pearlite deformation. Atom probe tomography has provided quantitative measurements of carbon concentrations in pearlite before and after deformation [14, 15], revealing that the main mechanisms for cementite decomposition are dislocation-assisted carbon diffusion [15] and carbon segregation at sub-grain boundaries in ferrite [14].

To observe the dynamic deformation process, synchrotron diffraction has been used to study stress-partitioning between ferrite and cementite [16, 17]. Digital image correlation revealed significant strain heterogeneity in pearlite, with strain concentration in specific colonies [10, 18, 19]. Tanaka et al. [20] identified room-temperature plastic deformation in cementite lamellae aligned parallel to the tensile direction.

Experimental studies of cementite deformation are challenging due to the small scales and large deformations involved. Molecular dynamics (MD) simulations provide a powerful complementary approach to probe the dynamic features of slip behavior in ferrite and cementite, offering insights into the deformation mechanisms of pearlite. Since interatomic potentials with special attention on cementite mechanical properties were developed [21, 22] and the interfacial structures between ferrite and cementite with several orientation relations (ORs) have been systematically explored [23], MD simulations are expected to qualitatively correspond to the deformation process of pearlite. Guziewski et al. [24] investigated the effects of supercell size, volume fraction, and loading direction on pearlite yield strength and flow stress using a bicrystal model. Their study revealed that dislocation loops initiate at the α-θ interface. In a subsequent study, the plastic deformation and yield strength of pearlite under various ORs were systematically explored [25]. The slip activities in cementite were attributed to slip transmission from ferrite and the geometric relationships between slip systems in the two phases and loading directions were highlighted. Yu et al. [26] studied the tensile behavior of inclined pearlite lamellae and reported structural transformations in ferrite and cleavage cracks in cementite near the interface. Shimokawa et al. [27] found that interfacial dislocations significantly influence the pearlite deformation mechanisms. Using knowledge of the stress field induced by interfacial dislocations and applying Schmid factor analysis, they examined slip activation at the interface. In addition, MD simulations have been used to investigate fatigue [28] and nano-indentation

deformation [29] in pearlite.

MD simulations of pearlite are often complemented by analytical models to calculate stress and strain states in each phase. For example, Guziewski et al. [24, 25] used composite theory, based on iso-strain or iso-stress assumption, to estimate the elastic properties of pearlite. Shimokawa et al. [27] considered the strain compatibility at the interface using directional Poisson ratios for the two phases. However, these methods [24, 25, 27] have two major drawbacks. First, the elastic tensors for the two phases are simplified into Young's moduli and Poisson ratios, which is insufficient for the consideration of the interface compatibility. It can be inferred from the near-full elastic tensor of pearlite [30]. Second, the iso-strain and iso-stress assumptions are established based on specific loading directions and are not generally applicable.

Initially, an analytical approach to calculate stress partitioning between phases was developed [31] and then further applied to periodic twin boundaries [32]. In this study, a similar analytical model is applied to investigate the stress and strain states in pearlite under complex loading conditions (Section 4.3). For the Bagaryatskii OR, the analysis highlights the critical influence of loading direction on the magnitude of nominal Schmid factors for slip systems in both cementite and ferrite.

Previous MD studies on the deformation of pearlite have been limited to a few specific orientations, and therefore do not sufficiently capture the general deformation behavior of pearlite. By defining non-orthogonal supercells, we explored the deformation process of pearlite under multiple loading directions for the first time, as detailed in Section 4.4. Simulation results, including the yield strength, slip behaviors in ferrite and cementite, and the corresponding nominal Schmid factors for active slip systems, are presented in Section 4.5. Finally, in Section 4.6, we discuss the key factors influencing the plasticity of pearlite and provide insights into its deformation mechanisms.

4.3 ANALYTICAL MODEL FOR PEARLITE MECHANICAL PROPERTIES

4.3.1 BICRYSTAL MODEL FOR PERIODIC COMPOSITE

As the elastic properties of ferrite (α) and cementite(θ) differ, the two phases respond distinctly when pearlite is subjected to loading. To maintain deformation compatibility, an additional stress field arises at the interface, known as the incompatibility stress [33]. The bicrystal model representing pearlite is shown in Fig. 4.1. The volume fractions of cementite and ferrite are V_θ and V_α, respectively. The interface plane is set parallel to the XOZ plane. The following constraints apply to the model [34].

1. The two phases are rigidly glued to each other. No relative motion is allowed at the interface.

2. All the interfaces are parallel and infinitely extended in the XOZ plane.

3. For each phase, there is a linear relation between stress and strain.
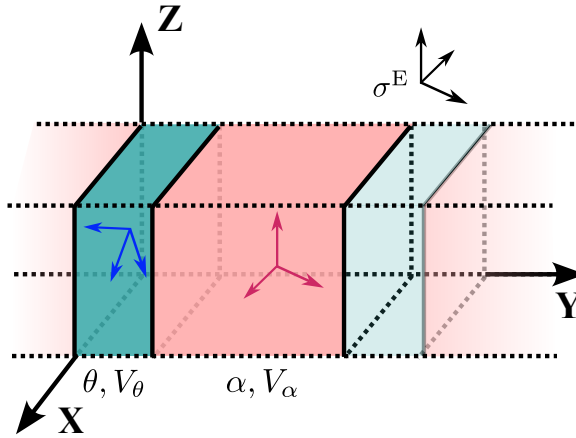
Figure 4.1: Schematic representation of the bicrystal model for pearlite with a layered periodic structure. Ferrite (α) and cementite (θ) layers are infinitely extended in the XOZ plane, with volume fraction of V_α and V_θ. The interface is perpendicular to the Y-axis. The external stress σ^E can be of any type. For the Bagaryatskii OR, the crystallographic orientations of the two phases are given in Table. 4.2.

With Voigt notation (xx $\to$ 1, yy $\to$ 2, zz $\to$ 3, yz $\to$ 4, xz $\to$ 5, xy $\to$ 6) with the engineering convention ($\varepsilon_4 = 2\varepsilon_{xy}$), the constitutive equation of linear elastic material is

$$
\begin{bmatrix} \varepsilon_1 \\ \varepsilon_2 \\ \varepsilon_3 \\ \varepsilon_4 \\ \varepsilon_5 \\ \varepsilon_6 \end{bmatrix} = \begin{bmatrix} s_{11} & s_{12} & s_{13} & s_{14} & s_{15} & s_{16} \\ s_{12} & s_{22} & s_{23} & s_{24} & s_{25} & s_{26} \\ s_{13} & s_{23} & s_{33} & s_{34} & s_{35} & s_{36} \\ s_{14} & s_{24} & s_{34} & s_{44} & s_{45} & s_{46} \\ s_{15} & s_{25} & s_{35} & s_{45} & s_{55} & s_{56} \\ s_{16} & s_{26} & s_{36} & s_{46} & s_{56} & s_{66} \end{bmatrix} \begin{bmatrix} \sigma_1 \\ \sigma_2 \\ \sigma_3 \\ \sigma_4 \\ \sigma_5 \\ \sigma_6 \end{bmatrix}
\tag{4.1}
$$

According to the first constraint listed above, strain components inside the interface plane should be continuous,

$$
\varepsilon_i^\theta - \varepsilon_i^\alpha = 0, \quad i,j = 1,3,5.
\tag{4.2}
$$

The tractions on the GB must be continuous, and the difference at the GB must vanish,

$$
\sigma_i^\theta - \sigma_i^\alpha = 0, \quad i = 2,4,6.
\tag{4.3}
$$

When under an arbitrary far-field external stress σ^E, global stress equilibrium requires

$$\frac{1}{V} \int_V \sigma_i dV = \sigma_i^E, \tag{4.4}$$

where σ^E is the applied external stress [31]. For pearlite,

$$\sigma_i^E = V^\theta \sigma_i^\theta + V^\alpha \sigma_i^\alpha. \tag{4.5}$$

For arbitrary ORs and volume fractions of the two phases, the above equations holds. In this study the Bagaryatskii OR [35]is adopted, as $[010]_\theta \| [111]_\alpha$, $[100]_\theta \| [1\bar{1}0]_\alpha$, and $(001)_\theta \| (\bar{1}\bar{1}2)_\alpha$.

The modified embedded atom method (MEAM) potential for Fe-C system developed by Liyanage et al. [22] was applied because it gives a good representation of both ferrite and cementite. Additionally, it has been used widely for simulating pearlite deformation [23, 36, 37].

We evaluated the performance of the MEAM potential in predicting the generalized stacking fault energy (GSFE) and the core structure of screw dislocations, and compared the results with available DFT data. The details are presented in Appendix E. It was found that, while the MEAM potential correctly captures the trend of the GSFE for the {112} and {110} slip systems, it exhibits significant inaccuracies in describing the core structure of screw dislocations. Similar limitations in the Peierls potential predicted by this MEAM potential have also been reported in the literature [38]. To clarify the impact of these inaccuracies in screw dislocation modeling on the simulation results, we additionally trained an Atomic Cluster Expansion (ACE) potential using the dataset provided in [39]. This machine-learning-based potential offers greater flexibility and accuracy while maintaining reasonable computational efficiency. Appendix F presents the training details of the ACE potential and demonstrates its excellent accuracy in reproducing the screw dislocation core structure, GSFE, and Peierls potential. Tensile simulations of the pearlite model along the 0° and 45° loading directions were repeated using the ACE potential. The results show a pronounced difference in both yield strength and dislocation activation at the interface depending on the loading direction, consistent with the trends observed using the MEAM potential. These findings confirm the reliability of the conclusions originally obtained with the MEAM potential.

The elastic tensor components for the two phases are shown in Table 4.1. For cementite the MEAM potential aims to reproduce the elastic tensor values of Jiang et al. [40], but as Table 4.1 shows, the MEAM values are representative for a wide spectrum of DFT results.

The compliance matrix S was determined through the strain response of the pearlite bicrystal model under the six independent unit stress states (σ_1 to σ_6). The stiffness matrix C is obtained by inverting S.

4

	Modulus (GPa)	C_{11}	C_{22}	C_{33}	C_{23}	C_{13}	C_{12}	C_{44}	C_{55}	C_{66}
Ferrite	MEAM [22]		213			143			119	
	Experiment [41]		243			138			122	
	Experiment [42]		240			136			121	
	PW91[a] [43]		277			147			96	
Cementite	MEAM [22]	326	303	249	135	119	163	72	27	98
	PBE[b] [44]	316	385	341	157	167	162	131	13	131
	PBE[a] [40]	322	388	345	156	162	164	134	15	134
	PBE[b] [40]	325	395	347	158	163	169	135	18	134
	PBE[b] [45]	319	393	340	144	149	141	114	-60	145
	PBE[b] [46]	323	388	344	155	160	145	135	18	132
	PW91[b] [47]	298	375	339	161	172	144	30	13	132
	PBE[b] [48]	300	383	344	162	162	156	135	28	134
	PBE[c] [48]	299	315	321	136	175	131	138	24	142
	PBE[d] [48]	309	354	340	146	171	137	131	33	129

[a] energy-strain method
[b] stress-strain method
[c] including quantum-harmonic corrections at 0 K
[d] including quantum-harmonic corrections at 400 K

Table 4.1: Elastic tensor components for ferrite and cementite (with $a < b < c$) at 0 K, except where noted otherwise. In DFT calculations two GGA implementations were used: PW91 [49] and PBE [50]. For cementite calculations are listed that include internal relaxations. Such relaxations are essential for accurate results [51].

4.3.2 Orientation-dependence of nominal Schmid factors

The Schmid factor m quantifies the effectiveness of a loading direction for activating a specific slip system. In its classical formulation, m is defined on purely geometric considerations in a homogeneous material under uniaxial stress conditions: $m = \cos\phi\cos\lambda$, where ϕ is the angle between the slip plane normal and the loading direction, and λ is the angle between the slip direction and the loading direction. This definition inherently limits m to values ≤ 0.5, with the maximum achieved when $\phi = \lambda = 45^{\circ}$. However, this formulation becomes inapplicable for describing slip system activation in non-homogeneous materials, and under non-uniaxial stress states, which are common in heterogeneous materials.

In pearlite, the presence of α-θ interfaces introduces significant incompatibility, as revealed by the bicrystal model. Even under macroscopic uniaxial loading of pearlite, the local stress states σ^{local} in α and θ deviate from uniaxial. To properly characterize slip system activation in these complex stress states, we introduce the nominal Schmid factor m_{n}, defined as:

$$m_{\text{n}} = \frac{\tau^{\text{local}}}{\sigma^{\text{uniaxial}}}, \tag{4.6}$$

where the local resolved shear stress τ^{local} is calculated through the full stress tensor formulation:

$$\tau^{\text{local}} = \mathbf{m} \cdot \boldsymbol{\sigma}^{\text{local}} \cdot \mathbf{n} = \sum_{i,j} \sigma_{ij}^{\text{local}} m_i \, n_j, \tag{4.7}$$

with $\boldsymbol{\sigma}^{\text{local}}$ being the local stress tensor, and $\mathbf{m}$ and $\mathbf{n}$ are unit vectors describing the slip direction and the normal to the slip plane, respectively [52]. This stress-based formulation is mathematically equivalent to the normalized resolved shear stress approach employed by Tiba et al. [53] in their study of nickel bicrystals (see Table 3), where grain boundary incompatibility stresses were similarly incorporated. The key advantage of m_{n} is its ability to account for both the local stress concentration effects and the crystallographic orientation of slip systems. Similar extensions of the Schmid factor have been proposed in the literature to address complex stress states [54, 55].

For ferrite, 24 $\{110\}\langle111\rangle$ and $\{112\}\langle111\rangle$ slip systems are considered. For cementite, all slip systems suggested by experiments are considered [8, 10, 12]: (100)[001], (100)[010], (010)[001], (010)[100], (001)[010], (001)[100], and (001)[110].

For a given σ^{uniaxial} along a certain direction, the highest m_{n} among all available slip systems indicates the maximum resolved shear stress for possible slip activity. Fig. 4.2 illustrates the highest m_{n} for slip systems in α (a) and θ (b) under uniaxial stress applied along various directions. The loading directions are projected on the

XOZ stereographic plane. The volume ratio between ferrite and cementite is set as $V_\alpha/V_\theta = 8$.

For α, which exhibits high crystallographic symmetry and multiple slip systems, the highest m_n ranges from 0.32 to 0.502. In contrast, the θ phase, due to its lower symmetry and fewer slip systems, shows a much wider range of the highest m_n values (0 to 1.02), with strong orientation dependence. Notably, the maximum values of highest m_n among all loading directions for both phases exceed the traditional Schmid factor limit of 0.5. The observed increase of m_n originates from two factors:

1. Definition: while m depends solely on the geometric factor ($\cos\phi\cos\lambda$) under uniaxial stress, m_n incorporates the complete local stress state as $\tau^{\mathrm{local}}/\sigma^{\mathrm{uniaxial}}$. The stress-based formulation naturally accounts for stress concentration effects. As a result, m_n is not constrained by the geometric limit of 0.5 and can exceed 1 in regions of significant stress concentration. E.g. when applying uniaxial loading to long, parallel fibers, the least compliant fibers will carry most of the load.

2. Strong incompatibility stress. The exceptionally high resolved shear stress for slip systems in θ originates from the incompatibility stress at the α-θ interface. Previous studies on nickel bicrystals under uniaxial compression reported m_n values up to 0.63 (Table 3 [53]), attributed to incompatibility stresses at the grain boundary. In pearlite, the larger volume fraction difference ($V_\alpha/V_\theta = 8$), and the stronger elastic contrast between α and θ compared to the nickel bicrystal amplify the incompatibility stress, especially in θ. The concentration of the incompatibility stress in the minority phase increases m_n values up to 1.02. Furthermore, in [53], the experimentally observed slip system activations agreed well with the calculated m_n. This indicates that m_n is a proper metric for slip activation in heterogeneous materials.

Fig. 4.2 also illustrates the loading directions used in the MD study of the mechanical behavior of pearlite. Previous MD simulations involving the plasticity of pearlite [24, 26–28, 56] focused on loading directions with low m_n in cementite, as indicated by the diamond symbols in the stereographic projection. In this work, we focus on loading directions marked by the brown stars. The choice of these directions is based on two considerations:

1. The range of m_n in cementite for these directions is between 0 and 0.95, providing a representative overview of the deformation behavior of pearlite.

2. Experimental observations indicate that during processes such as rolling or drawing, pearlite tends to align with the loading direction [57, 58]. As a result,

loading in the interface plane (here the XOZ plane) closely approximates the actual loading conditions in these scenarios.

To compare with previous work, loading directions marked by blue and red diamonds are included in this study also.
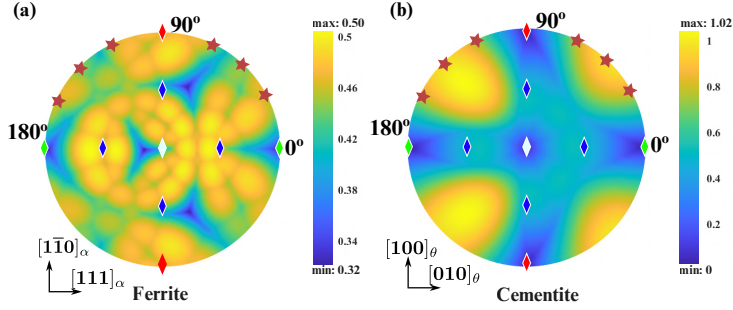

Figure 4.2: Highest nominal Schmid factors m_n in (a) ferrite and (b) cementite for a pearlite structure under uniaxial stress applied along various directions. The loading directions are represented on the XOZ stereographic projection. The value of the highest m_n varies from 0.32 to 0.50 for ferrite and 0 to 1.02 for cementite. Diamond markers indicate the specific directions studied in previous MD simulations: green [24, 25, 56, 59], red [24, 25, 27, 28, 56, 59], blue [26], white [24, 25, 37]. This study focuses on loading within the XOZ plane, highlighted by the brown stars, green diamonds and red diamonds, corresponding to loading in the $(11\bar{2})_\alpha$ and $(001)_\theta$ planes.

4.3.3 Influence of the volume ratio

As shown explicitly in Eq. 4.5, the volume fraction of the two phases significantly influences the partitioning of incompatibility stress across the interface. Here we use the ratio between hydrostatic stress $\sigma^h = (\sigma_1 + \sigma_2 + \sigma_3)/3$ and the external stress $\sigma^E = \sigma_2 \ (\sigma_i = 0 \ \forall \ i = 1, 3 - 6)$ to show the magnitude of stress concentration. Fig. 4.3(a) illustrates the effect of V^α/V^θ on σ^h/σ^E in the two phases. Without incompatibility stress at the interface, $\sigma^h/\sigma^E = 1/3$, corresponding to the horizontal dashed grey line. The magnitude of the additional stress field in each phase is inversely proportional to its volume fraction, which means phases with small volume fractions bear high additional stresses. For pearlite with $V^\alpha/V^\theta = 8$, σ^h/σ^E in cementite approaches 0.52, showing a 57% increase over the value without incompatibility stress. Fig. 4.3(b) and (c) depict the highest m_n for each loading direction in α and θ, respectively. The loading direction corresponds to the arc shown in Fig. 4.2(b), with the angle measured relative to the X-axis. All slip systems listed in the previous section are considered. For both phases, a decrease in V^θ/V^α leads generally to an increase in the m_n. Supercells with V^θ/V^α of 4 and 8 show rather similar stress levels and m_n. Therefore in the MD simulations we adopt supercells with $V^\theta/V^\alpha = 4$ to conserve computational resources.
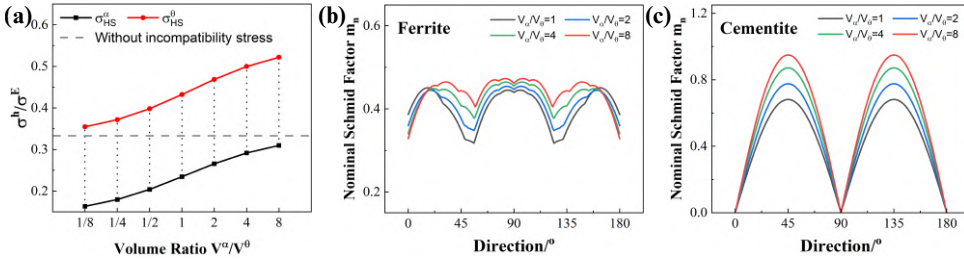
Figure 4.3: Influence of the volume ratio of ferrite and cementite on the stress partition in the two phase. (a) Hydrostatic stress in α and θ under unit σ_1^E. Hydrostatic stress for a unit normal stress is $1/3$, as shown with the dashed gray line. (b) and (c) show the highest nominal Schmid factor m_n for each loading direction within the XOZ plane in ferrite and cementite, respectively. The angle for the loading direction is with respect to X-axis, shown in Fig. 4.2(b). All slip systems listed in the previous section are considered.

4.4 Molecular dynamics simulation of pearlite

The elastic analysis in the previous section has clarified the relationship between the elastic properties of pearlite and the activation of dislocations in both phases under different loading directions. In the following, molecular dynamics simulations are conducted to validate these conclusions and to further investigate the influence of interface structure. Here the simulations aim to examine the influence of loading direction on yield strength, arising from the initial dislocation structure at the interface and the redistribution of stress between the two phases, a factor largely neglected in reported simulations. To isolate these effects, all models use a perfect lattice free of extraneous dislocations and vacancies.

With the MEAM potential provided in [22], the lattice parameter for BCC iron is $a^\alpha = 2.851$ Å. For Fe_3C, using the convention $a < b < c$, $a^\theta = 4.470$ Å, $b^\theta = 5.088$ Å, and $c^\theta = 6.670$ Å. To model pearlite using the Bagaryatskii OR with a periodic supercell, the supercell needs to be periodic for both α and θ simultaneously. Labeling the edges of the supercell as XYZ, the XOZ plane is chosen parallel with the α-θ interface which is coherent with the analytical model introduced in Section 4.3.

To create a pearlite supercell with minimum strain for both α and θ, the supercell edge length along X and Z needs to be an integer times a periodic vector for each of the two phases. Supercell dimensions that make for a near perfect match between both phases are shown in Table 4.2. The mismatch strain ε_i^m is estimated as

$$\varepsilon_i^m = 2(L_i^\theta - L_i^\alpha)/(L_i^\theta + L_i^\alpha),\tag{4.8}$$

where $i = X, Z$. Note that the mismatch strain is a different concept than the misfit strain. Using the elastic constants, the stresses induced by the mismatch strain in

both phases are estimated to be less than 0.5 GPa, which is significantly smaller than the yield strength presented later.

   Initiation of plastic deformation occurs independently in pearlite layers. Periodic boundary conditions may cause unrealistic results during MD simulations through artificial images when slip in one layer affects the slip behavior in other layers. Here we employ a pearlite supercell with two α-θ layers and four interfaces, as shown in Fig. 4.4(a) to reduce such artifacts.

Phase	item	X $[010]_\theta\|[111]_\alpha$	Y $[001]_\theta\|[\bar{1}\bar{1}2]_\alpha$	Z $[100]_\theta\|[1\bar{1}0]_\alpha$
Cementite	Unit cell(Å)	$b^\theta = 5.088$	$c^\theta = 6.670$	$a^\theta = 4.470$
	Supercell	$L_X^\theta = 32 \times 5.088 = 162.816$	$L_Y^\theta = 7.6 \times 6.670 = 50.692$	$L_Z^\theta = 18 \times 4.470 = 80.46$
Ferrite	unit cell(Å)	$a^\alpha \times \frac{\sqrt{3}}{2} = 2.469$	$a^\alpha \times \sqrt{6} = 6.983$	$a^\alpha \times \sqrt{2} = 4.032$
	Supercell	$L_X^\alpha = 66 \times 2.469 = 162.954$	$L_Y^\alpha = 30 \times 6.983 = 209.490$	$L_Z^\alpha = 20 \times 4.032 = 80.640$
Pearlite	Mismatch strain,Eq. 4.8	-0.08%	N/A	-0.22%
	Relaxed Supercell(Å)	$L_X = 163.03$	$L_Y = 515.73$	$L_Z = 80.64$

Table 4.2: The dimensions of the pearlite supercell in the Bagaryatskii crystal orientation and the mismatch strains on the interface, using MEAM interatomic potential by Liyanage et al. [22].

   During MD simulations, uniaxial loading is performed most conveniently along directions corresponding to supercell edges or perpendicular to supercell faces. Thus, to investigate the effect of loading direction on plastic deformation in pearlite, equivalent supercells with various edges were constructed, see Fig. 4.4(b), with distinct orientations along the longer edge in the XOZ plane, see Fig. 4.4(c). The cell lengths of the original cubic cell are $L_X = 163.03$ Å and $L_Z = 80.64$ Å. The angles between loading direction and $[010]_\theta\|[111]_\alpha$ were calculated as

$$\phi = tan^{-1}\frac{i \cdot L_Z}{L_X} \tag{4.9}$$

for loading along the slanted supercell edge and for loading perpendicular to the slanted supercell edge as

$$\phi = 90^o + tan^{-1}\frac{i \cdot L_Z}{L_X}, \tag{4.10}$$

where $i = -1, 0, 1, 2$. This gives angles of 0°, 26°, 45°, 64°, 90°, 116°, 135°, 154° (rounded) in the various equivalent supercells. In the following sections, these angles are used to denote uniaxial tensile straining simulations along the corresponding directions.

   Considering the symmetry of the pearlite in directions perpendicular to its stacking direction, ferrite exhibits mirror symmetry with respect to the $(1\bar{1}0)_\alpha$, while cementite features a $(001)_\theta$ mirror plane and a $(100)_\theta$ glide plane. When considering elasticity in continuum mechanics, a mirror symmetry appears with $(100)_\theta$ because cementite has an orthorhombic lattice. Therefore Bagaryatskii pearlite in our supercell exhibits mirror symmetry about the XOY plane in continuum
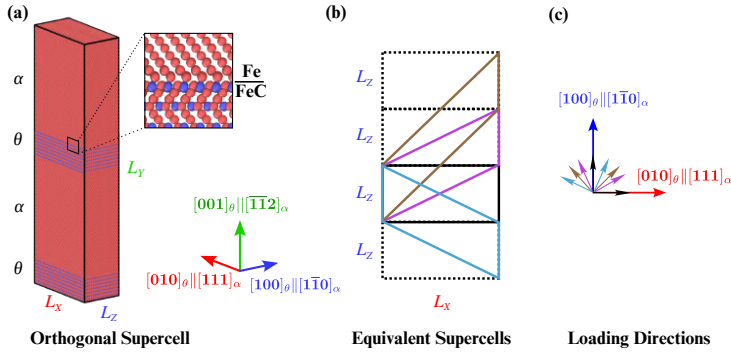
Figure 4.4: (a) Two-layer pearlite supercell with Bagaryatskii OR used for MD simulations. In the original supercell, X (Z) corresponds to $[010]_\theta \| [111]_\alpha$ ($\|[100]_\theta \| [1\bar{1}0]_\alpha$). The $\alpha - \theta$ interface is FeC-Fe which was reported to have the lowest interfacial energy [24]. FeC-Fe means that at the cementite side the nearest layer at the interface is FeC and next nearest layer is Fe. Equivalent supercells are defined by replacing the horizontal supercell edge with the slanted vectors (in color), as shown in (b). (c) displays the loading directions within the XOZ plane, both along and perpendicular to the slanted supercell edges. Directions are colored according to the corresponding equivalent supercells shown in (b). The red arrow corresponds to the $0°$ loading angle.

elasticity. When discussing the atomic-scale structure of interfaces, this mirror symmetry does not exist.

The α-θ interface structure for the Bagaryatskii OR was systematically examined by Guziewski et al. [24]. The FeC-Fe interface, see Fig. 4.4(a), which means the interfacial chemistry is FeC on the side of cementite, was found to be energetically favorable. Here, we implemented this interface structure by selectively removing several atom layers in the cementite, resulting in a non-integer unit cell replication count in cementite along the stacking direction, as shown in Table 4.2.

Following relaxation at 300 K for 20 ps with a Nose-Hoover thermostat, uniaxial strain was applied along one side of the supercell, as depicted in Fig. 4.4(c). During tensile testing, normal stresses in directions orthogonal to the applied strain were maintained at zero and the temperature was kept at 300 K. A strain rate of $1 \times 10^9 s^{-1}$ was employed, consistent with previous studies [27, 60]. For each load direction, three independent simulations were performed with different random initial velocities to ensure consistency.

It should be noted that shear strains are constrained to zero during tensile simulations for the following reasons:

1. Due to the low symmetry of pearlite, the simulation box under uniaxial stress naturally develops shear strain. This complicates the determination of slip plane indices and resolved shear stresses and obfuscates analysis.

2. Previous MD studies on pearlite employed orthogonal simulation boxes,

thereby eliminating shear strains. Adopting the same constraint allows for comparison with previous studies.

For each tensile direction (direction "x"), we constrain the three shear strains to zero and set the normal stresses in the two directions perpendicular to the loading direction to zero. With Voigt notation (loading direction "x", stacking direction "y"), the stress and strain components for current loading condition are calculated:

$$\sigma = C^p \cdot \varepsilon, \tag{4.11}$$

where $\sigma = [\sigma_1, 0, 0, \sigma_4, \sigma_5, \sigma_6]$, $\varepsilon = [\varepsilon_1, \varepsilon_2, \varepsilon_3, 0, 0, 0]$, and C^p is the elastic matrix for pearlite (as described in Section 4.3). For $V^\theta / V^\alpha = 4$, using the elastic tensor components for ferrite and cementite shown in Table 4.1 (MEAM), the pearlite elastic tensor (in GPa) under 0° loading direction is given as,

$$
C^p = \begin{bmatrix}
319 & 98 & 102 & 0 & 0 & -1 \\
 & 283 & 119 & 0 & 0 & -31 \\
 & & 299 & 0 & 0 & 33 \\
 & & & 62 & 21 & 0 \\
 & symmetric & & & 64 & 0 \\
 & & & & & 64
\end{bmatrix}. \tag{4.12}
$$

For other loading directions C^p must be rotated. It should be remarked that the pearlite supercell has an orthorhombic shape, but not orthorhombic symmetry due to the absence of mirror planes perpendicular to X and Y. For $\sigma_1 = 1$ GPa along various directions, the resulting stress and strain components of the supercells are listed in Table 4.3. The stress components are expressed in a local Cartesian coordinate system, where σ_1 aligns with the loading direction and the local y-axis is aligned with the global Y-axis. In particular, the shear stress can reach 19% of the tensile stress in the loading direction. In previous MD studies on pearlite, the additional shear stresses arising from the low symmetry of pearlite are overlooked [24, 25, 28, 56]. This oversight leads to an incomplete understanding of the stress state and its influence on the deformation mechanisms.

It should be noted that molecular dynamics (MD) simulations are inherently limited in both temporal and spatial scales. In typical pearlite, the lamellar spacing is in range 100–500 nm [61]. Due to computational constraints and the large number of simulations required in this study, the thickness of a single pearlite lamella (comprising one ferrite layer and one cementite layer) was set to 25 nm, which is smaller than that found in real microstructures. Nevertheless, the model preserves the correct orientation relationship, interface structure, and the stress redistribution arising from the elastic difference between the two phases.

	0°	26°	45°	64°	90°	116°	135°	154°
σ_4 (GPa)	0	0.09	0.06	-0.10	-0.19	-0.10	0.06	0.09
σ_5 (GPa)	0	-0.14	-0.03	0.10	0	-0.10	0.03	0.14
σ_6 (GPa)	0	0.05	0.18	0.17	0	-0.17	-0.18	-0.05
$\varepsilon_1 \times 10^3$	3.7	4.5	5.5	4.9	4.2	4.9	5.5	4.5
$\varepsilon_2 \times 10^3$	-0.9	-1.0	-1.2	-1.4	-1.5	-1.4	-1.2	-1.0
$\varepsilon_3 \times 10^3$	-0.9	-1.7	-2.4	-1.7	-0.9	-1.7	-2.4	-1.7

Table 4.3: Stress and strain components applied on supercells induced by $\sigma_1 = 1$ GPa loading along various directions. The stress and strain components are given in the local coordinate system, where σ_1 is along the (local) loading direction and the local y-axis is aligned with the global Y-axis.

The unit cell model for cementite was obtained from the Materials Project database (mp-510623) [62]. The construction of the supercell was carried out using Atomsk [63]. MD simulations were performed with the Large-scale Atomic/Molecular Massively Parallel Simulator (LAMMPS) [64], and the results were analyzed and visualized using OVITO 3.7.4 [65].

4.5 Results

4.5.1 Tensile behavior for pearlite

Fig.4.5 presents the stress-strain curves for tensile deformation along eight different loading directions. For all directions, the initial response is nearly linear, with stress increasing proportionally with strain. Both the tensile modulus and maximum stress exhibit significant variation across these loading directions. As in prior work [25, 27] we identify the maximum stress as the yield point. After yielding, the stress quickly drops to around 5 GPa and stabilizes at this level, except in 135° supercell, where stress decreases to a negative value post-yield. Utilizing the BCC Defect Analysis (BDA) algorithm [66], we attribute this anomalous negative stress to the formation of deformation twins within the ferrite phase in the 135° supercell. A detailed analysis of this phenomenon, however, lies beyond the scope of the present study. Tensile MD simulations are repeated three times, shown in black, red and blue, in order to verify reproducibility of the results.

The key features of these simulations are summarized in Fig. 4.6. Since the loading condition is not uniaxial, the so-called tensile modulus, defined as σ_1/ε_1, does not (exactly) correspond to the Young's modulus. In Fig. 4.6(a) the red squares and error bars represent the mean and standard deviation of the tensile modulus, measured at 1% strain, from three independent simulations as function of the loading direction. It shows that the modulus is highest at 0°(or equivalently 180°), reaching 274 GPa, while it is lowest at approximately 45° and 135°, dropping to about 190 GPa, 69% of the maximum value. The black solid line represents the tensile modulus calculated using the bicrystal model (Section 4.3) with a volume
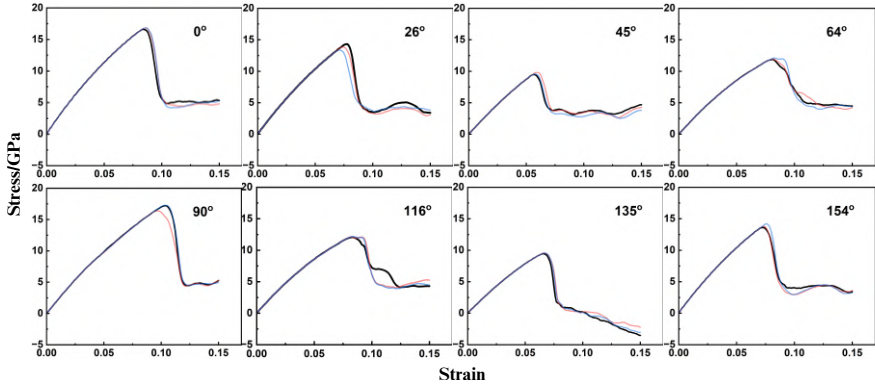
Figure 4.5: Stress-strain curves for tensile deformation along eight different loading directions, with the specific direction labeled in each plot. Red and blue lines represent two replicates using different random seeds for initial velocity generation.

ratio of 4:1. The close agreement between the black line and the simulated values demonstrates the validity of the bicrystal model. The red solid line shows the calculated modulus for a volume ratio of 8:1, which corresponds to actual pearlite. The 8:1 ratio exhibits slightly larger fluctuations than the 4:1 case but the tensile modulus variation with loading direction is almost identical.

By taking the highest stress value in the near-linear phase of the tensile process as the yield strength, Fig. 4.6 (b) illustrates the variation in yield strength across different loading directions. The yield strengths show a dramatic variation as function of loading direction, ranging from 9.5 GPa to 16.7 GPa. The yield strength reaches a maximum of 16.7 GPa at 0° and 90°. Interestingly, these directions correspond to the most extensively studied cases, and the 0° and 90° yield strengths are close to each other, which aligns well with previous reports [24, 56]. Conversely, the minimum yield strength occurs at 45° and 135°—directions that were not considered in prior studies. Generally plastic deformation modes with lower yield strengths are assumed to be activated earlier during homogeneous deformation. Therefore, previous MD studies on the tensile behavior of pearlite appear to have overlooked the most probable deformation modes.

Compared with laboratory deformation rates, MD necessarily employs unrealistically high strain rates. For thermally activated events such as dislocation nucleation and glide, transition-state theory [67] gives

$$\nu = \nu_0 \exp\left[-\frac{\Delta G(\tau, T)}{k_B T}\right],$$

where ν and ν_0 are the event frequency and the attempt frequency, respectively, and $\Delta G(\tau, T)$ is the activation free-energy barrier that depends on the resolved
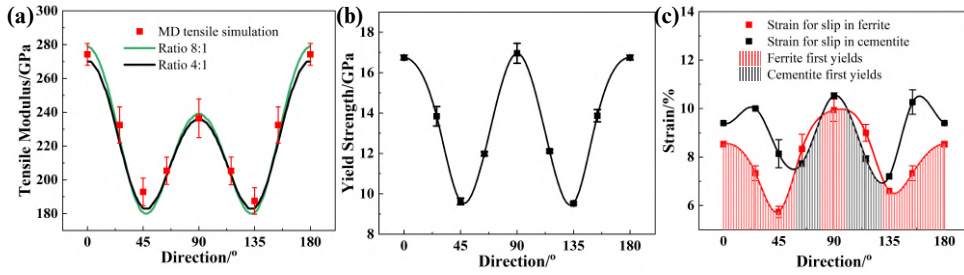
Figure 4.6: (a) Tensile modulus and (b) yield strength for tensile deformation along eight different directions, as obtained from MD simulations. The tensile moduli predicted by the bicrystal model are also included in (a) for comparison. Error bars indicate the standard deviation from three independent simulations. (c) Strain at which slip initiates, marked by squares, in cementite (black) and ferrite (red). Regions where plastic deformation occurs first in ferrite (cementite) are highlighted with red (black) shading. Lines provide guides to the eye.

4

shear stress τ and temperature T. At a fixed T, achieving a lower macroscopic strain rate requires a lower event rate. This corresponds to a larger effective barrier and hence a lower driving stress. Once $\Delta G(\tau)$ is known (e.g., from nudged elastic band (NEB) method [68, 69]), the stress response can be mapped quantitatively across strain-rate regimes.

Empirically, the rate sensitivity is often expressed as a power law [70],

$$\sigma = \sigma_0 \left(\frac{\dot{\varepsilon}}{\dot{\varepsilon}_0} \right)^m,$$

where m is the strain-rate sensitivity. Using polycrystalline Cu as a reference, MD data fitted for uniaxial tension give $m \approx 0.09$ [71]. Assuming, as a first-order estimate, that pearlite exhibits a comparable m, rescaling our MD results from $\dot{\varepsilon} = 10^9 \, \text{s}^{-1}$ to a representative experimental rate $\dot{\varepsilon} \approx 10^{-3} \, \text{s}^{-1}$ reduces the flow stress by a factor $(10^{-12})^{0.09} \approx 1/12$. Thus, the experimental-rate yield strengths inferred from our simulations would be on the order of 0.8–$1.4 \, \text{GPa}$.

These values still exceed many reported measurements [72], likely because our models are nearly defect-free and feature relatively fine pearlite interlamellar spacings—both of which raise the strength relative to typical bulk microstructures.

Fig. 4.6 (c) shows the overall strain at which plastic deformation initiates in ferrite (red squares) and cementite (black squares), determined from observations of slip bands in the supercells. For ferrite, plastic deformation occurs latest under tensile loading along 0° and 90°, and earliest near 45° and 135°. Notably, in the 45° direction, plastic deformation begins at a strain of less than 6%. For cementite, plastic deformation is delayed the longest at 26° and 154° (above 10% strain), while it occurs earliest at 135° with a strain of 7.2%. Interestingly, for loading directions

at 64º and 116º, plastic deformation in cementite occurs earlier than in ferrite—an observation not previously reported in MD simulations of pearlite deformation.

The tensile moduli along various directions are depicted in Fig. 4.6(a) shows a symmetry with respect to $(1\bar{1}0)_\alpha \| (100)_\theta$ plane. The strain corresponding to plasticity initiation shown in Fig. 4.6(c) does not exhibit such symmetry as explained in Section 4.3.2 based on the analysis of pearlite symmetry. In Fig. 4.6(b), the yield strength for various loading directions also seems to show such symmetry. It should be accidental, as the strain corresponding to the same yield strength and the plastic behavior within the two phases are not always consistent. Moreover, Fig.4.5 shows that the stress strain curves for 26º and 154º, 45º and 135º, and 64º and 116º are similar but not identical.

4.5.2 Interfacial dislocation structure

Fig. 4.7 highlights the high-energy atoms near the interface (low energy atoms are made transparent for clarity), revealing the dislocation network formed due to lattice misfit. A topological model was employed in prior work [73], in which the structural continuity across the ferrite–cementite interface was analyzed based on the atomic positions of Fe atoms. Dislocation patterns were systematically determined for five common ORs, including the Bagaryatsky OR adopted in this study. Notably, the dislocation network predicted for B-OR is in full agreement with the dislocation configuration observed in the present simulations, as compared in Table 4.4.

	Burgers vector $[b_x, b_z]$ (Å)		Line orientation (deg.)		Line spacing (Å)	
	b_1	b_2	Angle 1	Angle 2	d_1	d_2
[73]	[0.00, 4.20]	[-2.47, 0.00]	0.00	90.00	40.32	81.48
This work	[0.00, 4.03]	[-2.47, 0.00]	0.00	90.00	40.32	81.52

Table 4.4: Burgers vectors, dislocation line orientations, and spacings for ferrite-cementite interface with the Bagaryatsky orientation relationship.

It is worth noting that, although many theoretical and atomistic simulation studies have adopted this orientation relationship and the corresponding interfacial dislocation network as a basis, to the best of our knowledge, there is currently no direct experimental observation that unambiguously confirms the specific dislocation network associated with the Bagaryatsky OR. However, the Bagaryatsky OR itself has been firmly established by numerous experimental characterizations, such as [74]. For the Isaichev orientation, TEM studies have reported interfacial dislocations arising from lattice mismatch (see Ref. [75]), demonstrating that such dislocation structures can indeed occur at this type of interface. Therefore, even though direct experimental evidence for the Bagaryatsky-OR-related dislocation

network is lacking, the conclusions of this work remain strongly supported and experimentally relevant.

The interfacial dislocations consist of two types of edge dislocations. The first type has dislocation lines parallel to $[010]_\theta \| [111]_\alpha$, with a Burgers vector $\mathbf{b}_1 = [110]_\alpha$ and a dislocation spacing p_1 of 40.3 Å. The second dislocation lines parallel to $[100]_\theta \| [1\bar{1}0]_\alpha$, with a Burgers vector $\mathbf{b}_2 = 1/2[111]_\alpha$ and a dislocation spacing p_2 of 81.5 Å. The pattern is identical to previous studies on the interface structure in pearlite with the Bagaryatskii OR [24, 27]. The interfacial dislocation structure is the same for all equivalent supercells.
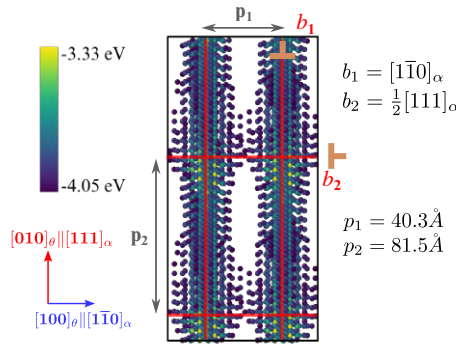

Figure 4.7: Atoms with relatively high potential energy after relaxation are shown in the figure. The misfit dislocation pattern at ferrite/cementite interface is marked with red lines. The Burger's vectors and spacings of the two dislocations are labeled on the figure.

4.5.3 Plasticity in ferrite

During the tensile simulation, the atomic configuration was recorded every 0.2% strain. The shear strain for each atom is calculated with initial configurations as references. Atoms with shear strains greater than 20% are considered to be the atoms that undergo plastic deformation. The planes formed by these atoms are regarded as slip planes, which are surrounded by dislocation lines (based on Dislocation Extraction Algorithm [76]). In the tensile simulations along various directions, five slip planes in ferrite at the initial stage of plasticity are observed, as shown in Figs. 4.8 (a-e). In these figures atoms belonging to the θ phase are colored gray. In the α phase only atoms with shear strain more than 20% are shown. The blue (white) atoms have a (non) BCC nearest neighbor shell according to common neighbor analysis. The schematic figure at upper right corner of each figure shows the position of the intersection lines of the slip plane at the interface (blue line) in relation to the misfit dislocation network (red line).

The nominal Schmid factors m_{n} of each slip system under various loading

	Angle 1	Angle 2	0°	26°	45°	64°	90°	116°	135°	154°
Unit	Degree		Dimensionless							
$(110)[\bar{1}11]$	90	0	<u>0.287</u>	**0.496**	<u>0.403</u>	0.237	0.058	0.112	0.077	0.066
$(110)[1\bar{1}1]$	90	0	<u>0.287</u>	0.066	0.077	0.112	0.058	0.237	0.403	**0.496**
$(1\bar{1}0)[111]$	0	90	0	0.381	**0.420**	<u>0.402</u>	0	<u>0.402</u>	**0.420**	0.381
$(121)[1\bar{1}1]$	73	17	**0.338**	0.076	0.167	0.306	0.310	0.128	0.352	<u>0.468</u>
$(211)[\bar{1}11]$	73	17	**0.338**	<u>0.468</u>	0.352	0.128	0.310	0.306	0.167	0.076
$(101)[\bar{1}11]$	59	31	0.298	0.315	0.207	0.015	0.479	**0.418**	0.212	0.066
$(011)[1\bar{1}1]$	59	31	0.298	0.066	0.212	**0.418**	0.479	0.015	0.207	0.315
$(1\bar{1}2)[1\bar{1}1]$	39	51	0.178	0.039	0.201	0.417	**0.519**	0.155	0.007	0.078
$(1\bar{1}2)[\bar{1}11]$	39	51	0.178	0.078	0.007	0.155	**0.519**	0.417	0.201	0.039

Table 4.5: Nominal Schmid factors m_n for slip systems which are observed in MD simulations at the initial stage of plasticity in ferrite. Angle 1 and 2 are the angles between the intersection of each slip plane with the two types of misfit dislocation lines on the interface. For each loading direction, the maximal m_n is highlighted in bold, and the actually activated slip planes are marked by underlining. The influence of incompatibility stress at the interface is taken into account.

conditions were calculated using the model presented in Section 4.3, as summarized in Table 4.5. The actual relative external stress for each loading mode is shown in Table 4.3. For each loading direction, the highest m_n is highlighted in bold, and slip systems observed in the simulations are underlined. Angle 1 and angle 2 denote the angles between the intersection lines of slip planes with the interface and the initial interfacial dislocation lines $\mathbf{b}_1$ and $\mathbf{b}_2$, respectively. The activation of slip systems in ferrite has been experimentally studied [77] with micro-tensile tests. It was found that $\{110\} < 111 >$ and $\{112\} < 111 >$ have similar critical resolved shear stresses (CRSS) [77]. Therefore slip systems with high m_n are considered more likely to be activated in ferrite.

The $(110)_\alpha$ and $(1\bar{1}0)_\alpha$ slip planes are of particular interest. Their intersection lines at the interface are parallel to the initial dislocation network with Burgers vectors $\mathbf{b}_1$ and $\mathbf{b}_2$. In addition, due to the pearlite structural symmetry discussed in Section 4.4, the m_n for slip planes in the table show a certain symmetry with respect to the row of 90°. E.g. the m_n for loading angles $90° + \beta°$ for the $(110)[\bar{1}11]$ slip system are equal to the m_n for loading angles $90° - \beta°$ for the $(110)[1\bar{1}1]$ slip system.

For loading along 0° ($[010]_\theta \| [111]_\alpha$), the slip planes are $(110)_\alpha$ and $(121)_\alpha$. The m_n are relatively low, therefore external stress required for slip activation is high. For the 26° supercell, the m_n for the two planes are getting higher, leading to a drop in the yield strength. When loaded along 45°, both $(110)_\alpha$ and $(1\bar{1}0)_\alpha$ planes exhibit high m_n. However, surprisingly, slip occurs on the $(110)_\alpha$ plane only. Under 135° loading both the $(110)_\alpha$ and the $(1\bar{1}0)_\alpha$ planes have the same m_n as under 45° loading. Nevertheless, under 135° loading slip occurs extensively on the $(1\bar{1}0)_\alpha$ plane rather than on the $(110)_\alpha$ plane. This surprisingly distinct yielding behavior
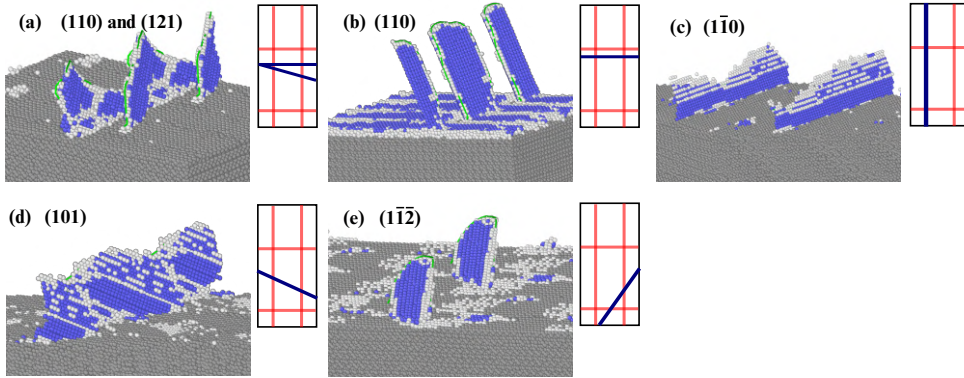
Figure 4.8: Four types of slip plane found in ferrite. (a) A combination of (110) and (121) planes; (b) (110) plane; (c) $(1\bar{1}0)$ plane, and (d) $(1\bar{1}2)$ plane. The OR between observed slip plane-interface intersection (blue lines) and the misfit dislocations at the interface (red lines) are shown in each subplot.

under 45° and 135° is evident by the red symbols in Fig. 4.6(c).

Considering the symmetry of pearlite discussed in Section 4.4, the onset of yielding and its progression is dependent on the symmetry properties of the whole supercell and on the atomic-scale structure.

For 64°, $(1\bar{1}0)_\alpha$ is the main slip surface although it has a lower m_n than $(011)_\alpha$. Slip on $(011)_\alpha$ is observed also, which has a higher m_n but a larger angle to the initial dislocation. When loading along 90° ($[100]_\theta\|[1\bar{1}0]_\alpha$), the m_n on both $(110)_\alpha$ and $(\bar{1}10)_\alpha$ slip surfaces are close to 0. $(1\bar{1}2)_\alpha$ and $(1\bar{1}2)_\alpha$ slip planes, which have the highest m_n, are activated. The cases of 116° and 154° supercells are consistent with the cases of 64° and 26° supercells, respectively.

A few key features of slip activity in ferrite are identified by combining observations of slip planes with m_n calculations:

1. Consistency with previous studies: Shimokawa et al. [27] and Zhang et al. [56] reported that under tensile loading along $[100]_\theta\|[1\bar{1}0]_\alpha$, the $\{112\} < 111 >$ slip system is activated, while for loading along $[010]_\theta\|[111]_\alpha$, the $\{110\} < 111 >$ slip system dominates deformation. The slip planes observed in this study align well with these earlier findings, validating the current modeling approach.

2. Significance of nominal Schmid factor: For different loading directions, the slip systems with the highest m_n are generally activated. However, for the 45° case, the slip system with the second-highest m_n is activated instead.

3. Alignment with initial dislocation network: Slip planes with intersection lines parallel to the initial dislocation at the interface, such as (110) and

	0°	26°	45°	64°	90°	116°	135°	154°
Slip plane 1	(110)	(110)	(110)	$(1\bar{1}0)$	$(1\bar{1}2)$	$(1\bar{1}0)$	$(1\bar{1}0)$	(110)
CRSS (GPa)	4.81	6.86	3.88	4.82*	8.80	4.87*	4.00	6.88
Slip plane 2	(121)	(211)		(011)		(101)		(121)
CRSS (GPa)	5.66	6.47		5.00*		5.06*		6.49

Table 4.6: Critical resolved shear stress for slip planes in ferrite calculated according to Eq. 4.13. Numbers marked with an asterisk correspond to the plastic deformation initiating in cementite, see Fig. 4.6(c).

$(1\bar{1}0)$, exhibit higher activity. For every loading direction studied, at least one active slip plane aligns with the initial dislocation. An exception is in the 90° case, where the m_n for the (110) and $(1\bar{1}0)$ slip planes are nearly zero. Then, slip occurs on $(1\bar{1}2)$ and $(1\bar{1}2)$ planes. For the 0°, 64°, and 116° loading directions, (110) and $(1\bar{1}0)$ slip planes are observed, while other slip systems with slightly higher m_n remain inactive.

From the tensile simulation, CRSS for slip systems in ferrite are calculated using

$$\sigma^{\text{CRSS}} = \sigma^{\text{yield}} \cdot m_n, \tag{4.13}$$

where σ^{yield} is the yield strength shown in Fig. 4.6(b) and m_n is shown in Table. 4.5. The CRSS values for all activated slip systems in ferrite are provided in Table 4.6. In general, the CRSS for $\{110\}_\alpha$ and $\{112\}_\alpha$ planes are comparable, as observed for loading directions of 0°, 26°, and 154°, consistent with experimental observations [77]. However, a notable exception is the $(1\bar{1}2)_\alpha$ plane under 90° loading, which exhibits a significantly higher CRSS of 8.80 GPa compared to other $\{112\}_\alpha$ planes. This highlights the critical influence of slip system alignment with interface dislocations in reducing the CRSS. For the $(110)_\alpha$ plane, the CRSS varies from 3.88 GPa (45° loading) to 6.88 GPa (154° loading). This variation arises from changes in the local atomic environment induced by significant, loading direction dependent, elastic deformation before slip initiation. It should be noted that the elastic strain exceeds 6% before yielding.

4.5.4 Plasticity in cementite

As shown in Fig. 4.9, the deformation of cementite, while straining pearlite supercells, can be categorized in three types,

1. slip bands in cementite appear after significant plastic deformation in ferrite. E.g., Fig. 4.9(a) shows slip bands in the 0° supercell under 10% tensile strain, where a certain alignment between the slip planes in cementite and ferrite is observed. Slip transmission across the interface driven by strong plasticity in ferrite is reported previously as well [27, 28].
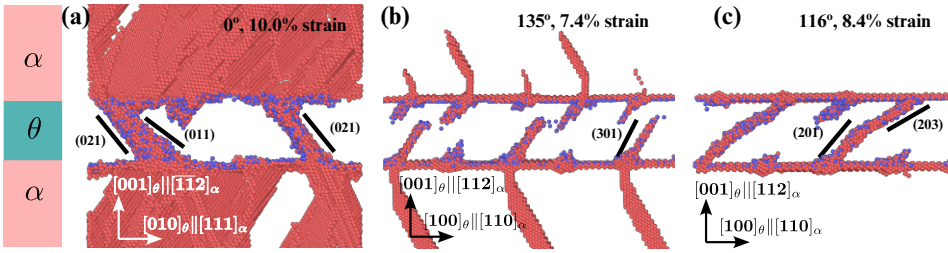
Figure 4.9: Three types of slip planes observed in cementite. (a) Type I: slip systems in cementite are activated after significant plastic deformation in ferrite. (b) Type II: slip planes in ferrite and cementite are activated synchronously, exhibiting identical slip traces at the interface. (c) Type III: slip occurs first in cementite. The classifications for various loading conditions are listed in Table 4.7. Fe (C) atoms with a shear strain of more than 20% are colored in red (blue) while atoms with less than 20% shear strain are not shown. The perspectives of the three figures correspond to the directions along $[100]_\theta$ and twice $[010]_\theta$. Animations corresponding to the three types of plastic deformation are provided in Supplement 1.

Loading condition	0°	26°	45°	64°	90°	116°	135°	154°
Slip plane	(021)	(021)	(021)	(20$\bar{1}$)	(20$\bar{1}$)	(201)	(201)	(011)
	(011)	(031)	(031)	(10$\bar{1}$)	(10$\bar{1}$)	(101)	(301)	(032)
	(0$\bar{2}$1)				(101)			
Corresponding Strain (%)	9.4	10.0	8.1	7.7	10.5	7.9	7.2	10.3
Relation to Slip in ferrite	I	I	I	II, III	I	III	II	I
CRSS (GPa)				4.1		4.2	5.8	

Table 4.7: Slip planes observed during the initial stage of plastic deformation in cementite under various loading conditions. The strain values required to activate these slip planes, averaged over three independent simulations, are listed also. For loading directions where slip occurs in cementite first, the CRSS is calculated according to Eq. 4.13.

2. slip bands in cementite are activated shortly after plastic deformation begins in ferrite, as shown in Fig. 4.9(b). Strong correspondence of slip planes at two sides of the interface is observed.

3. slip bands in cementite appear before plastic deformation in ferrite occurs, as shown in Fig. 4.9(c).

The slip planes observed during the initial stage of cementite plastic deformation under various loading conditions and their corresponding strain values are summarized in Table 4.7.

The cementite slip bands can be classified into two types according to their intersection lines at the $\theta - \alpha$ interface.

1. $(0kl)_\theta$ slip bands with an intersection line of $[100]_\theta \| [1\bar{1}0]_\alpha$ at the interface.

2. $(h0l)_\theta$ slip bands with an intersection line of $[010]_\theta \| [111]_\alpha$ at the interface.

Slip planes in ferrite and slip bands in cementite are observed to form matching pairs: for supercells where the $(110)_\alpha$ slip plane is activated in ferrite, cementite exhibits $(0kl)_\theta$ slip bands, while when the $(1\bar{1}0)_\alpha$ slip plane is active in ferrite, cementite displays $(h0l)_\theta$ slip bands. The specific slip plane that occurs in ferrite as a function of the loading angle is given in Table 4.5.

Computational works, such as those by Karkina et al. [78, 79], have shown that the stacking fault energy for different slip systems in cementite varies a lot. For example, the energy for stable stacking faults in $(103)_\theta$ is 0.28 $J \cdot m^{-2}$ while for $(102)_\theta$ the value is 0.87 $J \cdot m^{-2}$ [79]. Although the interatomic potential used previously [79] differs from the one applied in this work, here too, there is strong variation in the difficulty of initiating slip on various slip planes within cementite. Therefore, m_n for various slip systems in cementite are not a good indicator for the propensity of slip activation. Previous experiments [11, 12] have suggested $[100]_\theta$ ($[010]_\theta$) is the slip direction for $(011)_\theta$ ($(101)_\theta$) slip planes. In this study, we adopt these directions for the $(0kl)_\theta$ and $(h0l)_\theta$ slip planes. This choice can be rationalized by the fact that slip systems with shorter Burgers vectors generally exhibit lower energy barriers during slip. Consequently, m_n for these slip systems are close to zero for the 0º and 90º loading cases but reach relatively high values for the 45º and 135º cases, as illustrated in Fig. 4.2(b).

To illustrate the influence of interfaces and incompatibility stresses on the activation of slip systems in cementite, we directly compare the deformation behavior of the cementite phase within pearlite with that of pure cementite under the same loading direction, as shown in Fig. 4.10. The tensile direction is 116º, corresponding to Type III deformation mode of pearlite in Fig. 4.9, in which slip occurs first in cementite. The slip planes were identified as atoms with shear strain greater than 0.2. Fig. 4.10(a) and (b) show the slip planes of cementite in pearlite and bulk cementite, respectively. In (a), slip occurs at a strain of 8.4%, while in (b), the value is 13.4%. For bulk cementite, the slip planes are $(201)_\theta$ and $(\bar{2}01)_\theta$, which can be inferred as the most favorable slip planes under this loading condition. Multiple slip planes are formed simultaneously. In contrast, for cementite within pearlite, slip occurs on the $(201)_\theta$ and $(203)_\theta$ planes. Compared to bulk cementite, on one hand, the slip planes in pearlite originate from interfacial dislocations and are fewer in number; on the other hand, they include both the (201) plane, consistent with bulk cementite, and the $(203)_\theta$ plane, which forms to maintain compatibility with interfacial dislocations.

Fig. 4.10(c) shows the stress-strain curves for pearlite and cementite under the same loading condition. Three independent simulations for bulk cementite were performed with different random initial velocities to ensure consistency. For ferrite and cementite in pearlite, the stresses are represented by red and blue dots, respectively, obtained by averaging the stresses of atoms located at least 5 Å away

from the interface in each phase. Key observations include:

1. The stress required for slip in cementite within pearlite is 13.8 GPa, whereas for bulk cementite it is approximately 40% higher at 19.3 GPa.

2. In pearlite deformation, the two phases bear different stress levels. Ferrite, with a lower tensile modulus, exhibits lower stress (red dots), while cementite exhibits higher stress (blue dots). Even after substantial elastic deformation when the two phases are no longer in the linear elastic regime, the cementite still bears the higher tensile stress.

3. The model shown in Section 4.3 predicts the stresses in the two phases during deformation, as shown by the two dashed lines. At low strains, the predicted values agree well with the MD simulation. At higher strains, although the material remains in the elastic regime, the stress-strain relationship becomes non-linear, and the MD stress levels are lower than the predicted values.

4. Compared to bulk cementite, cementite within pearlite exhibits higher stress at the same strain, as predicted by the analytical model, which shows the influence of incompatibility stresses. The contribution of incompatibility stresses exists throughout the elastic regime. When the overall strain exceeds 6%, the stress in cementite within pearlite becomes lower than that in bulk cementite due to interface sliding.

In brief, the lower slip stress in cementite within pearlite at this loading direction is attributed to three factors: the higher tensile modulus of cementite relative to ferrite, stress concentration caused by interfacial incompatibility stresses, and the facilitation of slip by interfacial dislocations. For the case of loading along 116°, Fig. 4.10(c) demonstrates that the dislocations near the interface initiate slip in cementite at lower stresses than in bulk cementite.

[80] performed *in situ* tensile observations on pearlite with two different lamellar spacings and found that, in coarse-lamellar pearlite (lamellar spacing ∼ 400 nm), the cementite fractured in a brittle manner, whereas in fine-lamellar pearlite (spacing ∼ 90 nm) the cementite exhibited appreciable plasticity (e.g., necking and the formation of small fragments). This contrast was attributed to the stability of voids within the cementite lamellae. The observation is consistent with our finding that plastic deformation initiates in the cementite phase for current models.
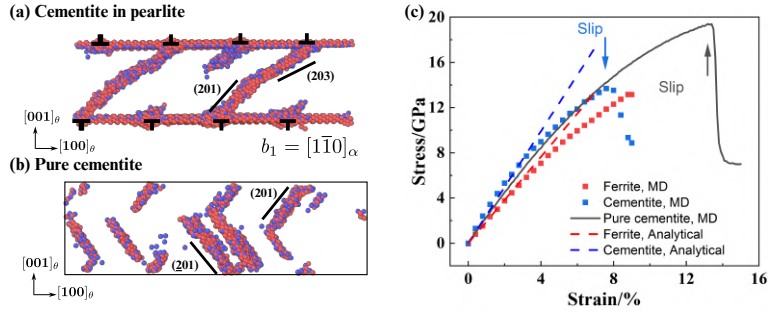
Figure 4.10: Comparison of tensile deformation in cementite embedded in pearlite and pure cementite. (a) Slip bands in cementite as part of pearlite, loaded along the 116° direction at an overall strain of 8.4%. (b) Slip bands in bulk cementite under same loading direction as (a), at a strain of 13.4%. (c) Stress-strain curves for the two supercells. For ferrite and cementite in pearlite, the stresses are represented by red and blue dots, respectively, while the black line represents the stress-strain relation in bulk cementite. The stress is obtained by averaging the σ_1 atomic stress component of atoms located at least 5 Å away from the interface in each phase. The theoretical stresses in the two phases, calculated using the analytical model in Section 4.3, are shown as dashed lines.

4.6 Discussion

4.6.1 Factors influence the plasticity in pearlite

In this paper, the effect of the loading direction on the deformation behavior of pearlite is demonstrated using equivalent supercells with carefully designed periodicities. The analytical model in Section 4.3 gives insight in the elastic properties of pearlite and considers the nominal Schmid factors m_n in both the ferrite and cementite constituents. On the basis of m_n, the onset of plastic deformation can be guessed, however, our MD simulations reveal that such a description is oversimplified. There are various factors affecting the deformation of pearlite.

1. Nominal Schmid factors m_n. m_n aligns closely with the activation of slip systems. For ferrite, the Schmid factor provides a quantitative prediction of the activated slip planes, as found previously also [25]. For cementite, the magnitude of m_n qualitatively explains the influence of the loading direction on slip activation. For loading directions with high m_n in cementite (e.g., 45° and 135°), slip planes in cementite are activated at strains of 8.1% and 7.2%, respectively. In contrast, for directions with low m_n in cementite (e.g., 0° and 90°), slip activation occurs at strains of 9.4% and 10.5%, respectively, showing a significant increase.

2. Interfacial dislocations. The initial interfacial dislocation structure reduces the critical resolved shear stress (CRSS), enabling slip planes parallel to the interfacial dislocation lines to activate earlier, here: $(110)_\alpha$ and $(1\bar{1}0)_\alpha$. The

CRSS for ferrite slip can be estimated by dividing the yield strength by m_n of the activated slip system. For the $(1\bar{1}2)_\alpha$ plane, which has a 39° angle with interfacial dislocations, the CRSS is 8.8 GPa. For the $(110)_\alpha$ slip plane along the dislocation line, the CRSS is only 4.8 GPa, 45% less than for $(1\bar{1}2)_\alpha$. When loading at 0°, the initial slip occurs on the $(110)_\alpha$ plane. This plane aligns with the interfacial dislocation $\mathbf{b}_2$. The $(121)_\alpha$ plane, which has a higher m_n but is not as well aligned with interfacial dislocations, slips subsequently. For cementite, the $[010]_\theta$ and $[100]_\theta$ directions are aligned with the interfacial dislocation lines. Therefore the intersection lines of $(0kl)_\theta$ and $(h0l)_\theta$ planes on the interface is parallel to the interfacial dislocation. It can be expected that this specific orientation facilitates a lower energy barrier for slip activation in cementite.

3. Loading direction. The loading direction significantly influences the m_n. In pure ferrite, the abundance of slip systems results in relatively low m_n anisotropy. However, in pearlite, the interfacial dislocations reduce the CRSS for $(110)_\alpha$ and $(1\bar{1}0)_\alpha$ planes, introducing pronounced anisotropy in ferrite slip activation. For cementite, the limited number of slip systems causes substantial anisotropy in m_n, as shown in Fig. 4.2(b).

4. Volume ratio of the two phases. While phase volume fractions do not directly alter the geometric relationship between interface structure and slip systems, they strongly affect the distribution of incompatibility stresses at the interface. The stress partitioning is inversely proportional to the phase volume fraction, leading to significant stress concentrations in the phase with smaller volume, as shown in Fig. 4.3(a). In pearlite with a ferrite-to-cementite volume ratio of 8 : 1, this amplifies the anisotropy of slip activation in cementite.

5. Temperature. During the tensile simulations, the temperature was maintained at 300 K using a Nose-Hoover thermostat. This temperature is significantly higher than that used in previous MD simulations [24, 25, 27]. Given that the plasticity of cementite is highly temperature-sensitive [9], this elevated temperature may explain the occurrence of slip bands in this work. From a practical perspective, the actual wire drawing process of pearlite involves large plastic deformation, which results in substantial heat accumulation. Takahashi et al. [81] demonstrated that reducing the drawing speed to mitigate thermal effects can suppress the decomposition of cementite. Therefore, the temperature setting in MD simulations warrants careful consideration in order to accurately represent realistic thermal conditions during pearlite processing.

4.6.2 Insights into the anisotropy of plastic deformation

The current analysis shows a significant dependence of the plasticity of pearlite on the loading direction, which arises from factors such as the lamellar structure, initial dislocations at interfaces, and the geometric relationship between the loading direction and slip systems. We hypothesize that the deformation mechanism of pearlite proceeds as follows:

In the earliest stages of deformation, ferrite with favorably oriented slip systems deforms first and undergoes work hardening through dislocation multiplication. The plastic deformation is highly localized, as observed in experiments [18, 20, 82]. This explains the relatively low yield strength of pearlite, as shown in pearlite tensile tests [82].

Subsequently, cementite in geometrically favorable orientations begins to slip with the assistance of interfacial dislocations. This challenges the view that cementite plasticity is caused only by dislocation pile-up in ferrite at the interface [24, 25, 28, 59]. By examining a wider range of loading directions, we find that the tensile stress needed for slip behavior in cementite can be less than 10 GPa, which is much lower than previous studies, for example, 12-19 GPa from first principles calculation [46] and 15-20 GPa from MD simulation [24]. The loading direction selected in previous studies [24, 27, 28, 56, 59] corresponds to a relatively low m_n in cementite, as shown in Fig.4.2, which explains the high external stresses that are required for activation of slips in cementite in these works. The predicted early onset of cementite slip suggests that cementite fragmentation and amorphization observed in experiments [13, 82] could occur at the initial stages of pearlite drawing. Interfacial dislocations also emit dislocations into the ferrite. The geometrically connected slip planes on both sides of the interface facilitate the relocation of carbon atoms from cementite to ferrite [15, 83]. This carbon relocation enhances the work-hardening rate in ferrite, which in turn maintains the load-carrying capacity of the material and prevents necking instability during severe plastic deformation.

For cementite with geometrically unfavorable orientation, dislocations originating in the adjacent ferrite accumulate at the interfaces and eventually penetrate into the cementite, as described previously [24, 25, 28, 59]. This process represents a secondary strengthening mechanism that becomes active as deformation continues. As the thickness of cementite layer decreases, stress concentration within the cementite becomes more pronounced, as discussed in Section 4.3.1. This mechanism further promotes cementite decomposition and enhances solid-solute strengthening in ferrite.

Several key characteristics of pearlite are crucial for achieving exceptional work-hardening rate increases as a function of strain.

1. The presence of (semi-)coherent interfaces ensures interfacial strength and

facilitates slip transfer.

2. The low volume fraction and the very fine lamellar distribution of the brittle phase allow it to undergo slip without crack formation when embedded in a deformable phase.

3. The brittle phase can decompose, releasing a large number of interstitial solute atoms, leading to strengthening through the coupling of dislocations and solute atoms during deformation.

4. The significant variation in yield strength among domains with different stacking orientations contributes to the ability to achieve large plastic deformation before failure.

Many eutectic and eutectoid alloys have finely layered microstructures, resembling pearlite, suggesting that there may be other alloys where high strength and plasticity can be achieved [84–87]. For example, Chen et al. [88] applied heavy drawing to a eutectic high-entropy alloy wire with a FCC-B2 structure. After severe deformation, the wire showed excellent strength while maintaining good ductility.

Previous studies have emphasized the importance of ψ, the angle between the loading direction and the pearlite stacking direction, in analyzing pearlite deformation [18, 57, 89]. For example, Toshihiko et al. investigated the relationship between the strain within a pearlite colony and ψ [89]. However, this work demonstrates that even when the loading direction lies within the plane of the α-θ interface, the mechanical properties and deformation mechanisms of pearlite exhibit significant variation, as shown in Fig. 4.6. For a general ψ, the pearlitic orientations corresponding to a specific angle form a conical surface in three-dimensional space. In Fig. 4.2, points on circles centered at the origin of the XOZ stereographic projection represent the same ψ. m_n (indicated by color) vary widely across these orientations. This variation highlights the inadequacy of classification methods based solely on the angle between the loading direction and the stacking direction. Moreover, in real materials, plastic deformation is governed by regions that yield first, making deformation modes with lower yield strengths more relevant. Therefore, for structurally anisotropic materials like pearlite, a careful selection of loading directions is crucial to ensure representative results in simulations and micro-mechanical experiments.

4.7 CONCLUSION

In this study, molecular dynamics simulations combined with an analytical model are employed to investigate the deformation behavior of pearlite. For the Bagaryatskii orientation relationship, we find that the loading directions chosen in previous

studies do not adequately represent the actual deformation mechanism of pearlite. To allow a wide range of loading directions in atomically identical supercells, tensile simulations are conducted using equivalent supercells with carefully designed periodicities. As during wire-drawing lamellae are observed to align with the drawing direction, various loading directions perpendicular to the stacking direction were examined. The main conclusions are as follows.

1. Pearlite exhibits significant anisotropy in plastic deformation capacity. Even when the loading direction is within the interface plane, the yield strength varies greatly with the angle between the loading direction and the $[010]_\theta$ direction, ranging from a minimum of 9.5 GPa at 45° and 135° to a maximum of 17.0 GPa at 0° and 90°.

2. In certain loading directions, slip bands in cementite activate before ferrite, challenging the conventional assumption that deformation always starts in ferrite and then transfers to cementite. A sequence of strengthening mechanisms—initial work hardening in ferrite, slip in favorably oriented cementite, and slip transfer into unfavorably oriented cementite—coupled with interfacial effects and carbon dissolution, results in work hardening over a wide range of strain, explaining the remarkable plastic deformation and exceptional tensile strength.

3. During early-stage deformation, slip systems in both phases align with initial interfacial dislocations. Slip activation in ferrite is according to the nominal Schmid factor m_n. At specific loading directions, and during later stages of deformation, slip initiation in cementite occurs. This is promoted by the low cementite volume fraction and by high temperature.

The approach presented here is applicable to other lamellar alloy systems. By leveraging the structural and processing insights from pearlite, it is anticipated that other materials with superior deformability and high strength can be developed.

Appendix E Validation of MEAM Potential on GSFE and Screw Dislocation Core

Figure E.1 (a) shows the generalized stacking fault energy (GSFE) and (b) the differential displacement map for the core structure of screw dislocations in BCC Fe using the MEAM potential [22]. For the GSFE curves, the potential correctly predicts the trend $\gamma_{112} > \gamma_{110}$. However, for screw dislocations, the potential produces a split-core structure, which is inconsistent with DFT results [90]. The discrepancy is known to be an artifact of many empirical potentials [38].
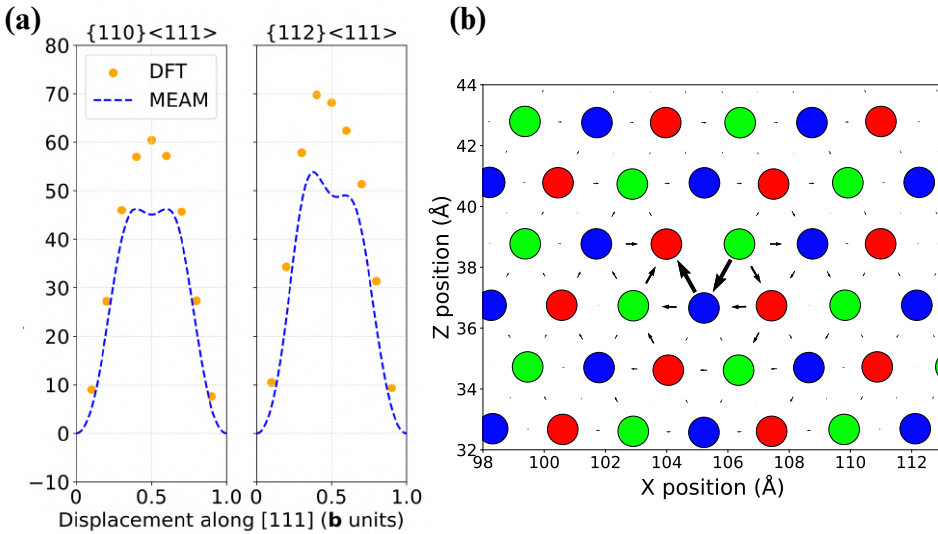
Figure E.1: (a) Generalized stacking fault energy curves for the $\{110\}\langle 111 \rangle$ and $\{112\}\langle 111 \rangle$ slip systems. DFT data are taken from [91]. (b) Differential displacement map of the screw dislocation core structure predicted by the MEAM potential. Atom colors indicate their positions along the y-axis (normal to the page): atoms with smaller Y-coordinates (closer to the observer) are shown in blue, while those with larger Y-coordinates (farther away) are shown in red.

Appendix F ACE Potential Training and Comparison with MEAM in Tensile Simulations

An ACE potential was trained using the dataset provided in [39], which contains 32,000 configurations. The cutoff distance was set to 6.5 Å. The parameters for the embedding function were set to [1, 1, 1, 0.5, 1, 0.75, 1, 0.25, 1, 0.125, 1, 0.375, 1, 0.875, 1, 0.625]; therefore, 600 functions with 5475 parameters were used. The ratio between the weights for force and energy was 0.01. A BFGS optimizer was applied for 2000 cycles. The root mean square error (RMSE) for the training set is 3.43 meV/atom for energy and 75.14 meV/Å for force.

The computational efficiency of three Fe−C interatomic potentials are benchmarked: MEAM [22], NNP [39], and the ACE potential developed here, using a 600,000-atom system on a CPU (AMD EPYC 9654 with 192 cores). The relative efficiency is approximately NNP : ACE : MEAM = 1 : 12 : 125, which is consistent with the performance trends reported in [92].

Tables 4.8 and 4.9 present the basic properties of BCC Fe and θ-Fe$_3$C computed using density functional theory (DFT), the NNP [39], and the ACE potential. It can be seen that the ACE potential accurately describes lattice parameters, elastic constants, surface energies, and vacancy formation energy.

Table 4.8: Comparison of basic properties of BCC Fe between DFT, NNP, and ACE.

	Lattice constant (Å)	Elastic constants (GPa)			Surface energy (Jm^{-2})				E_v (eV)
		C_{11}	C_{12}	C_{44}	(100)	(110)	(111)	(112)	
DFT	2.830	297	151	105	2.488	2.449	2.691	2.575	2.223
NNP	2.828	270	135	92	2.479	2.426	2.667	2.590	2.183
ACE	2.832	262	135	89	2.472	2.395	2.724	2.588	2.144
ACE Relative Error(%)	0.1	-11.8	-10.6	-15.2	-0.6	-2.2	1.2	0.5	-3.6

Table 4.9: Comparison of lattice constants and elastic constants of Fe$_3$C between DFT, NNP, and ACE.

Method	Lattice constant (Å)			Elastic constants (GPa)								
	a	b	c	C_{11}	C_{22}	C_{33}	C_{12}	C_{13}	C_{23}	C_{44}	C_{55}	C_{66}
DFT	4.48	5.04	6.72	322	388	345	164	162	156	134	15	134
NNP	4.47	5.02	6.74	310	365	341	153	177	172	115	14	122
ACE	4.48	5.07	6.70	323	372	366	166	177	192	127	24	126
ACE Relative Error(%)	0.0	0.6	−0.3	0.3	−4.1	6.1	1.2	9.3	23.1	−5.2	60.0	−6.0

The ACE potential also accurately reproduces key dislocation-related properties in BCC Fe, such as the screw dislocation core structure, the Peierls potential, and
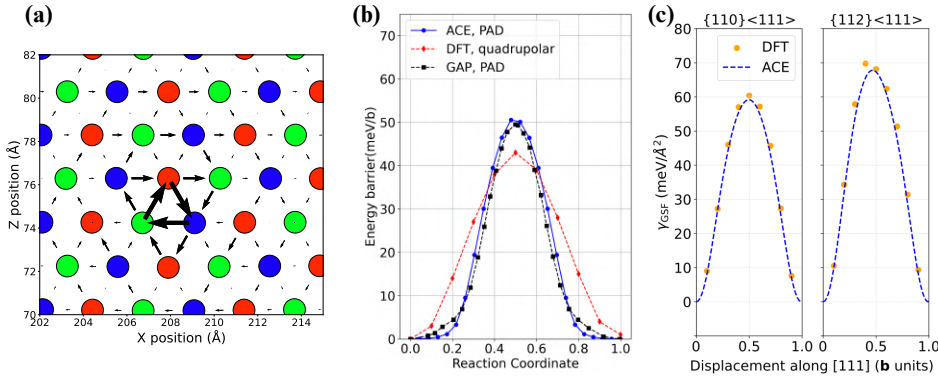
Figure F.1: Characteristics of dislocations in BCC Fe as described by the ACE potential. (a) Differential displacement map of a screw dislocation. The atoms are colored according to their positions along the Y-axis: atoms with smaller Y coordinates (closer to the observer) are shown in blue, while those with larger Y coordinates (farther away) are shown in red. (b) Peierls potential at 0 K under zero applied stress. (c) Generalized stacking fault energy (GSFE) curves for the {112}⟨111⟩ and {110}⟨111⟩ slip systems.

generalized stacking fault energy (GSFE), as shown in Fig. F.1. A comparison with DFT data [68, 90, 91] confirms the high accuracy of the ACE potential in describing these features.

The performance of the ACE potential in predicting the phonon spectrum of BCC Fe and the GSFE of θ-Fe$_3$C is further examined, shown in Fig. F.2. The phonon spectra were computed with Phonopy [93]. The GSFE for the (100), (010), and (001) planes of θ-Fe$_3$C was modeled using deformed supercells (for details see [94]), with a sampling step of 10% of the reaction coordinate (i.e., 100 configurations constructed for each plane). The RMSE of the predictions from the three potentials was calculated over all configurations. All DFT calculations are preformed with the same setting as that in [39]. It can be seen that the ACE potential captures phonon characteristics with satisfactory accuracy, and its error in GSFE prediction is much lower than that of the MEAM potential, while comparable to, or even lower than, that of the NNP.

Using this potential, the tensile simulations along the 0° and 45° directions of the pearlite model were repeated. Figure F.3 presents a comparison between the ACE and MEAM potentials in terms of dislocation nucleation (visualized via atoms with shear strain larger than 0.2) and stress–strain curves. The ACE potential predicts the same sequence of slip activation and exhibits a similar trend in the dependence of yield strength on the loading direction.

(a)

(b)
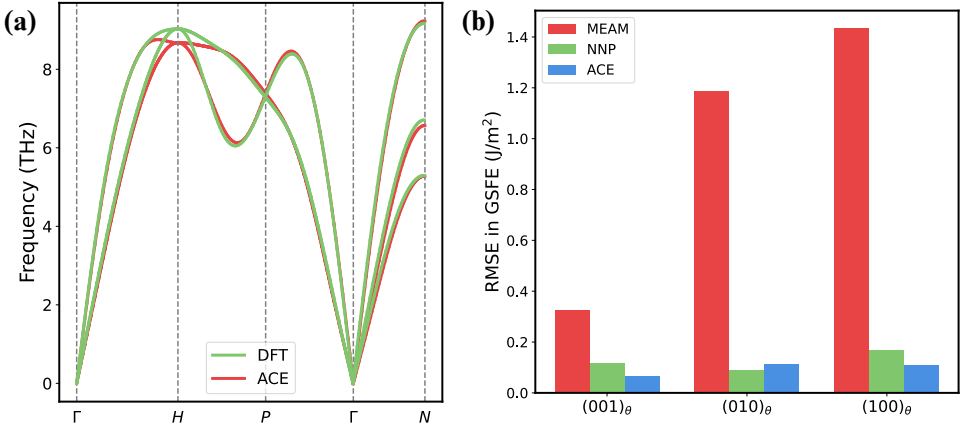
Figure F.2: Performance of the three potentials on (a) phonon spectrum for BCC iron; (b) generalized stacking fault energy for (100), (010), and (001) planes of cementite. The RMSE are evaluated on 100 configurations.
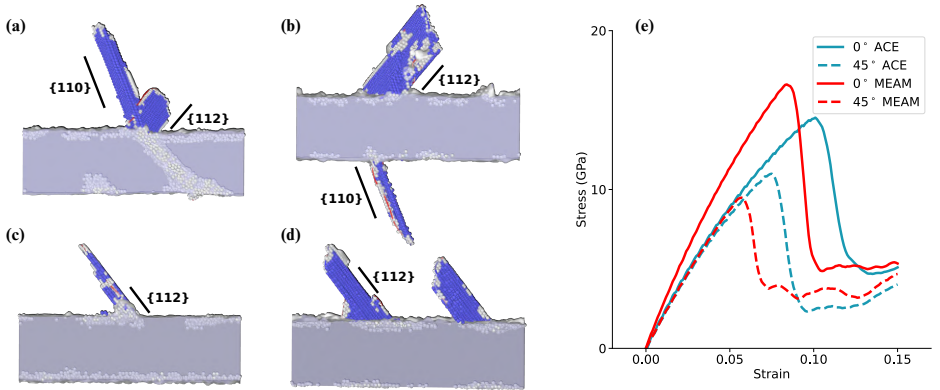

Figure F.3: Results of tensile simulations repeated with ACE potential, in comparison with MEAM potential. (a-d) Slip bands in ferrite at the initiation of plasticity. (e) Stress-strain curves during tensile simulations.

References

[1] Yujiao Li, Dierk Raabe, Michael Herbig, Pyuck-Pa Choi, Shoji Goto, Aleksander Kostka, Hiroshi Yarita, Christine Borchers, and Reiner Kirchheim. Segregation stabilizes nanocrystalline bulk steel with near theoretical strength. *Physical review letters*, 113(10):106104, 2014.

[2] Xiaodan Zhang, Andrew Godfrey, Niels Hansen, Xiaoxu Huang, Wei Liu, and Qing Liu. Evolution of cementite morphology in pearlitic steel wire during wet wire drawing. *Materials characterization*, 61(1):65–72, 2010.

[3] Soundes Djaziri, Yujiao Li, Gh. Ali Nematollahi, Blazej Grabowski, Shoji Goto, Christoph Kirchlechner, Aleksander Kostka, Stephen Doyle, Jörg Neugebauer, Dierk Raabe, and Gerhard Dehm. Deformation-induced martensite: A new paradigm for exceptional steels. *Advanced Materials*, 28(35):7753–7757, 2016.

[4] Xiaodan Zhang, Andy Godfrey, Xiaoxu Huang, Niels Hansen, and Qing Liu. Microstructure and strengthening mechanisms in cold-drawn pearlitic steel wire. *Acta Materialia*, 59(9):3422–3430, 2011.

[5] Christine Borchers and Reiner Kirchheim. Cold-drawn pearlitic steel wires. *Progress in Materials Science*, 82:405–444, 2016.

[6] John Jairo Coronado and Sara Aida Rodríguez. Cementite characterization with chromium and vanadium contents using indentation technique. *Journal of Iron and Steel Research International*, 22(4):366–370, 2015.

[7] A Fernández-Vicente, Massimo Pellizzari, and JL Arias. Feasibility of laser surface treatment of pearlitic and bainitic ductile irons for hot rolls. *Journal of Materials Processing Technology*, 212(5):989–1002, 2012.

[8] Jon Alkorta and Javier Gil Sevillano. Assessment of elastic anisotropy and incipient plasticity in Fe_3C by nanoindentation. *Journal of Materials Research*, 27(1):45–52, 2012.

[9] T Terashima, Y Tomota, M Isaka, T Suzuki, M Umemoto, and Y Todaka. Strength and deformation behavior of bulky cementite synthesized by mechanical milling and plasma-sintering. *Scripta materialia*, 54(11):1925–1929, 2006.

[10] Hanna Tsybenko, Chunhua Tian, Julia Rau, Benjamin Breitbach, Paul Schreiber, Christian Greiner, Gerhard Dehm, and Steffen Brinckmann. Deformation and phase transformation in polycrystalline cementite (Fe_3C) during single-and multi-pass sliding wear. *Acta Materialia*, 227:117694, 2022.

[11] Akihisa Inoue, Tsugio Ogura, and Tsuyoshi Masumoto. Deformation and fracture behaviours of cementite. *Transactions of the Japan Institute of Metals*, 17(10):663–672, 1976.

[12] A Inoue, T Ogura, and T Masumoto. Burgers vectors of dislocations in cementite crystal. *Scripta Metallurgica*, 11(1):1–5, 1977.

[13] YT Zhou, XH Shao, SJ Zheng, and XL Ma. Structure evolution of the Fe_3C/Fe interface mediated by cementite decomposition in cold-deformed pearlitic steel wires. *Journal of Materials Science & Technology*, 101:28–36, 2022.

[14] YJ Li, P Choi, Christine Borchers, S Westerkamp, S Goto, Dierk Raabe, and Reiner Kirchheim. Atomic-scale mechanisms of deformation-induced cementite decomposition in pearlite. *Acta Materialia*, 59(10):3965–3977, 2011.

[15] P-Y Tung, Xuyang Zhou, David Mayweg, Lutz Morsdorf, and Michael Herbig. Under-stoichiometric cementite in decomposing binary Fe-C pearlite exposed to rolling contact fatigue. *Acta Materialia*, 216:117144, 2021.

[16] A Kanie, Y Tomota, S Torii, and T Kamiyama. Elastic strains of cementite in a pearlite steel during tensile deformation measured by neutron diffraction. *ISIJ international*, 44(11):1952–1956, 2004.

[17] E Gadalińska, A Baczmański, Chedly Braham, G Gonzalez, H Sidhom, S Wroński, T Buslaps, and K Wierzbanowski. Stress localisation in lamellar cementite and ferrite during elastoplastic deformation of pearlitic steel studied using diffraction and modelling. *International Journal of Plasticity*, 127:102651, 2020.

[18] Yuto Yajima, Norimitsu Koga, and Chihiro Watanabe. Influential factors on the deformability of colonies in pearlitic steel. *Materials Characterization*, 177:111197, 2021.

[19] Pablo B Paiva Leão, João R Barros Neto, Samuel Filgueiras Rodrigues, Ladislav Novotnỳ, Jorge Luiz Cardoso, Luis Flavio Gaspar Herculano, Tiago Nunes Lima, Antonio J Ramirez, and Hamilton Ferreira G de Abreu. In-situ tensile-shear test in SEM and DIC analysis of two pearlitic steel microstructures: undeformed-coarse and deformed-refined. *Journal of Materials Research and Technology*, 24:9441–9461, 2023.

[20] Masaki Tanaka, Yusuke Yoshimi, Kenji Higashida, Tomotsugu Shimokawa, and Tetsuya Ohashi. A multiscale approach for the deformation mechanism in

pearlite microstructure: Experimental measurements of strain distribution using a novel technique of precision markers. *Materials Science and Engineering: A*, 590:37–43, 2014.

[21] Krister OE Henriksson and Kai Nordlund. Simulations of cementite: An analytical potential for the Fe-C system. *Physical Review B—Condensed Matter and Materials Physics*, 79(14):144107, 2009.

[22] Laalitha SI Liyanage, Seong-Gon Kim, Jeff Houze, Sungho Kim, Mark A Tschopp, Michael I Baskes, and Mark F Horstemeyer. Structural, elastic, and thermal properties of cementite (Fe_3C) calculated using a modified embedded atom method. *Physical Review B*, 89(9):094102, 2014.

[23] Matthew Guziewski, Shawn P Coleman, and Christopher R Weinberger. Interface energetics and structure of the pearlitic microstructure in steels: An atomistic and continuum investigation. *Acta Materialia*, 155:1–11, 2018.

[24] Matthew Guziewski, Shawn P Coleman, and Christopher R Weinberger. Atomistic investigation into the mechanical properties of the ferrite-cementite interface: The Bagaryatskii orientation. *Acta Materialia*, 144:656–665, 2018.

[25] Matthew Guziewski, Shawn P Coleman, and Christopher R Weinberger. Atomistic investigation into interfacial effects on the plastic response and deformation mechanisms of the pearlitic microstructure. *Acta Materialia*, 180:287–300, 2019.

[26] Manjiang Yu and Fangli Duan. Atomistic investigation of deformation behavior of lamellar pearlite with inclined orientation. *International Journal of Plasticity*, 177:103988, 2024.

[27] Tomotsugu Shimokawa, Tomoaki Niiyama, Masashi Okabe, and Jun Sawakoshi. Interfacial-dislocation-controlled deformation and fracture in nanolayered composites: Toward higher ductility of drawn pearlite. *Acta Materialia*, 164:602–617, 2019.

[28] Lun-Wei Liang, Yun-Jiang Wang, Yan Chen, Hai-Ying Wang, and Lan-Hong Dai. Dislocation nucleation and evolution at the ferrite-cementite interface under cyclic loadings. *Acta Materialia*, 186:267–277, 2020.

[29] Hadi Ghaffarian, Ali Karimi Taheri, Seunghwa Ryu, and Keonwook Kang. Nanoindentation study of cementite size and temperature effects in nanocomposite pearlite: A molecular dynamics simulation. *Current Applied Physics*, 16(9):1015–1025, 2016.

4

[30] I Watanabe, D Setoyama, N Nagasako, N Iwata, and K Nakanishi. Multiscale prediction of mechanical behavior of ferrite–pearlite steel with numerical material testing. *International journal for numerical methods in engineering*, 89(7):829–845, 2012.

[31] T. Richeton and S. Berbenni. Effects of heterogeneous elasticity coupled to plasticity on stresses and lattice rotations in bicrystals: A field dislocation mechanics viewpoint. *European Journal of Mechanics, A/Solids*, 37:231–247, 2013.

[32] T. Richeton, I. Tiba, S. Berbenni, and O. Bouaziz. Analytical expressions of incompatibility stresses at $\Sigma 3 < 111 >$ twin boundaries and consequences on single-slip promotion parallel to twin plane. *Philosophical Magazine*, 95(1):12–31, 2015.

[33] Kai Liu and Marcel H.F. Sluiter. Incompatibility stress at inclined grain boundaries for cubic crystals under hydrostatic stress and uniaxial stress. *Materialia*, 34:102071, 2024.

[34] Kai Liu and Marcel H.F. Sluiter. Stresses at grain boundaries: The maximum incompatibility stress in an infinitely extended elastic bicrystal under uniaxial loading. *Scripta Materialia*, 234:115570, 2023.

[35] Yu A Bagaryatskii. The probable mechanism of the martensite decomposition (H. Brutcher Technical Translations). *Doklady Akademii Nauk SSSR*, 73:1161–1164, 1950.

[36] Wei Guo, Yifei Meng, Xie Zhang, Vikram Bedekar, Hongbin Bei, Scott Hyde, Qianying Guo, Gregory B Thompson, Rajiv Shivpuri, Jian-Min Zuo, et al. Extremely hard amorphous-crystalline hybrid steel surface produced by deformation induced cementite amorphization. *Acta Materialia*, 152:107–118, 2018.

[37] Jun Wang, Ziwei Ma, Gan Ding, Rong Yang, Songlin Cai, Lanhong Dai, Minqiang Jiang, and Chunsheng Lu. Energy dissipation in pearlitic steel under impact loading. *Acta Materialia*, 284:120599, 2025.

[38] Arnaud Allera, Fabienne Ribeiro, Michel Perez, and David Rodney. Carbon-induced strengthening of bcc iron at the atomic scale. *Physical Review Materials*, 6(1):013608, 2022.

[39] Fan-Shun Meng, Shuhei Shinzato, Shihao Zhang, Kazuki Matsubara, Jun-Ping Du, Peijun Yu, Wen-Tong Geng, and Shigenobu Ogata. A highly transferable

and efficient machine learning interatomic potentials study of α-fe−c binary system. *Acta Materialia*, 281:120408, 2024.

[40] C. Jiang, S. G. Srinivasan, A. Caro, and S. A. Maloy. Structural, elastic, and electronic properties of Fe_3C from first principles. *Journal of Applied Physics*, 103(4):043502, 02 2008.

[41] J. A. Rayne and B. S. Chandrasekhar. Elastic constants of iron from 4.2 to 300 K. *Phys. Rev.*, 122:1714–1716, Jun 1961.

[42] John J Adams, DS Agosta, RG Leisure, and H Ledbetter. Elastic constants of monocrystal iron from 3 to 500 K. *Journal of applied physics*, 100(11), 2006.

[43] Michael Müller, Paul Erhart, and Karsten Albe. Analytic bond-order potential for bcc and fcc iron—comparison with established embedded-atom method potentials. *Journal of Physics: Condensed Matter*, 19(32):326220, jul 2007.

[44] M. Nikolussi, S.L. Shang, T. Gressmann, A. Leineweber, E.J. Mittemeijer, Y. Wang, and Z.-K. Liu. Extreme elastic anisotropy of cementite, Fe_3C: First-principles calculations and experimental evidence. *Scripta Materialia*, 59(8):814–817, 2008.

[45] Z.Q. Lv, F.C. Zhang, S.H. Sun, Z.H. Wang, P. Jiang, W.H. Zhang, and W.T. Fu. First-principles study on the mechanical, electronic and magnetic properties of Fe_3C. *Computational Materials Science*, 44(2):690–694, 2008.

[46] N. Garvik, Ph. Carrez, and P. Cordier. First-principles study of the ideal strength of Fe_3C cementite. *Materials Science and Engineering: A*, 572:25–29, 2013.

[47] G. Ghosh. A first-principles study of cementite (Fe_3C) and its alloyed counterparts: Elastic constants, elastic anisotropies, and isotropic elastic moduli. *AIP Advances*, 5(8):087102, 08 2015.

[48] L. Mauger, J. E. Herriman, O. Hellman, S. J. Tracy, M. S. Lucas, J. A. Muñoz, Yuming Xiao, J. Li, and B. Fultz. Phonons and elasticity of cementite through the Curie temperature. *Phys. Rev. B*, 95:024308, Jan 2017.

[49] John P Perdew and Yue Wang. Accurate and simple analytic representation of the electron-gas correlation energy. *Physical Review B*, 45(23):244–249, 1992.

[50] J. P. Perdew, K. Burke, and M. Ernzerhof. Generalized gradient approximation made simple. *Physical Review Letters*, 77:3865–3868, October 1996.

4

4

[51] M.H.F. Sluiter, M. Weinert, and Y. Kawazoe. Determination of the elastic tensor in low-symmetry structures. *Europhysics Letters*, 43(2):183, jul 1998.

[52] Franz Roters, Philip Eisenlohr, Thomas R Bieler, and Dierk Raabe. *Crystal plasticity finite element methods: in materials science and engineering*. John Wiley & Sons, 2011.

[53] Idriss Tiba, T Richeton, Christian Motz, Horst Vehoff, and Stéphane Berbenni. Incompatibility stresses at grain boundaries in Ni bicrystalline micropillars analyzed by an anisotropic model and slip activity. *Acta Materialia*, 83:227–238, 2015.

[54] Shuai-Feng Chen, Hong-Wu Song, Shi-Hong Zhang, Ming Cheng, Ce Zheng, and Myoung-Gyu Lee. An effective Schmid factor in consideration of combined normal and shear stresses for slip/twin variant selection of Mg-3Al-1Zn alloy. *Scripta Materialia*, 167:51–55, 2019.

[55] Dabiao Xia, Xiang Chen, Guangsheng Huang, Bin Jiang, Aitao Tang, Hong Yang, Serge Gavras, Yuanding Huang, Norbert Hort, and Fusheng Pan. Calculation of Schmid factor in Mg alloys: Influence of stress state. *Scripta Materialia*, 171:31–35, 2019.

[56] Haichao Zhang, Yinli Chen, and Yanhui Sun. Molecular dynamics simulation study on impact of interface chemistry on pearlite mechanical response. *Materials Research Express*, 10(9):096514, 2023.

[57] A Durgaprasad, S Giri, S Lenka, S Kundu, S Mishra, S Chandra, RD Doherty, and I Samajdar. Defining a relationship between pearlite morphology and ferrite crystallographic orientation. *Acta Materialia*, 129:278–289, 2017.

[58] Feng Fang, Lichu Zhou, Xianjun Hu, Xuefeng Zhou, Yiyou Tu, Zonghan Xie, and Jianqing Jiang. Microstructure and mechanical properties of cold-drawn pearlitic wires affect by inherited texture. *Materials & design*, 79:60–67, 2015.

[59] Hadi Ghaffarian, Ali K Taheri, Keonwook Kang, and Seunghwa Ryu. Molecular dynamics simulation study on the effect of the loading direction on the deformation mechanism of pearlite. *Multiscale Science and Engineering*, 1:47–55, 2019.

[60] Tomotsugu Shimokawa, Takumi Oto, and Tomoaki Niiyama. Molecular dynamics simulation of the effect of cementite decomposition on yield phenomena in pearlite microstructure. *ISIJ International*, 62(2):343–352, 2022.

[61] N Ridley. A review of the data on the interlamellar spacing of pearlite. *Metallurgical and Materials Transactions A*, 15(6):1019–1036, 1984.

[62] Anubhav Jain, Shyue Ping Ong, Geoffroy Hautier, Wei Chen, William Davidson Richards, Stephen Dacek, Shreyas Cholia, Dan Gunter, David Skinner, Gerbrand Ceder, et al. Commentary: The materials project: A materials genome approach to accelerating materials innovation. *APL materials*, 1(1), 2013.

[63] Pierre Hirel. Atomsk: A tool for manipulating and converting atomic data files. *Computer Physics Communications*, 197:212–219, 2015.

[64] A. P. Thompson, H. M. Aktulga, R. Berger, D. S. Bolintineanu, W. M. Brown, P. S. Crozier, P. J. in 't Veld, A. Kohlmeyer, S. G. Moore, T. D. Nguyen, R. Shan, M. J. Stevens, J. Tranchida, C. Trott, and S. J. Plimpton. LAMMPS - a flexible simulation tool for particle-based materials modeling at the atomic, meso, and continuum scales. *Comp. Phys. Comm.*, 271:108171, 2022.

[65] Alexander Stukowski. Visualization and analysis of atomistic simulation data with OVITO-the open visualization tool. *Modelling and Simulation in Materials Science and Engineering*, 18(1), JAN 2010.

[66] Johannes J Möller and Erik Bitzek. BDA: A novel method for identifying defects in body-centered cubic crystals. *MethodsX*, 3:279–288, 2016.

[67] Peter Hänggi, Peter Talkner, and Michal Borkovec. Reaction-rate theory: fifty years after kramers. *Reviews of modern physics*, 62(2):251, 1990.

[68] Francesco Maresca, Daniele Dragoni, Gábor Csányi, Nicola Marzari, and William A Curtin. Screw dislocation structure and mobility in body centered cubic fe predicted by a gaussian approximation potential. *npj Computational Materials*, 4(1):69, 2018.

[69] Lei Zhang. *Multiscale modeling of fracture in bcc metals*. Phd thesis, University of Groningen, Groningen, the Netherlands, 2024.

[70] Ting Zhu and Ju Li. Ultra-strength materials. *Progress in Materials Science*, 55(7):710–757, 2010.

[71] Ali Rida, M Micoulaut, Emmanuelle Rouhaud, and Ali Makke. Understanding the strain rate sensitivity of nanocrystalline copper using molecular dynamics simulations. *Computational Materials Science*, 172:109294, 2020.

4

[72] HKDH Bhadeshia and AR Chintha. Critical assessment 41: the strength of undeformed pearlite. *Materials Science and Technology*, 38(16):1291–1299, 2022.

[73] Jaemin Kim, Keonwook Kang, and Seunghwa Ryu. Characterization of the misfit dislocations at the ferrite/cementite interface in pearlitic steel: An atomistic simulation study. *International Journal of Plasticity*, 83:302–312, 2016.

[74] Hongcai Wang, Xie Zhang, Dingshun Yan, Christoph Somsen, and Gunther Eggeler. Interface dominated cooperative nanoprecipitation in interstitial alloys. *Nature Communications*, 9(1):4017, 2018.

[75] YT Zhou, SJ Zheng, YX Jiang, TZ Zhao, YJ Wang, and XL Ma. Atomic structure of the fe/fe3c interface with the isaichev orientation in pearlite. *Philosophical Magazine*, 97(27):2375–2386, 2017.

[76] Alexander Stukowski, Vasily V Bulatov, and Athanasios Arsenlis. Automated identification and indexing of dislocations in crystal interfaces. *Modelling and Simulation in Materials Science and Engineering*, 20(8):085007, 2012.

[77] Chaowei Du, F Maresca, Marc GD Geers, and Johan PM Hoefnagels. Ferrite slip system activation investigated by uniaxial micro-tensile tests and simulations. *Acta Materialia*, 146:314–327, 2018.

[78] LE Kar'kina, IN Kar'kin, and AR Kuznetsov. Atomistic simulation of stacking faults in (001),(010), and (100) planes of cementite. *The Physics of Metals and Metallography*, 115:85–97, 2014.

[79] LE Karkina, IN Karkin, IG Kabanova, and AR Kuznetsov. Crystallographic analysis of slip transfer mechanisms across the ferrite/cementite interface in carbon steels with fine lamellar structure. *Journal of Applied Crystallography*, 48(1):97–106, 2015.

[80] DA Porter, KE Easterling, and GDW Smith. Dynamic studies of the tensile deformation and fracture of pearlite. *Acta metallurgica*, 26(9):1405–1422, 1978.

[81] Jun Takahashi, Makoto Kosaka, Kazuto Kawakami, and Toshimi Tarui. Change in carbon state by low-temperature aging in heavily drawn pearlitic steel wires. *Acta Materialia*, 60(1):387–395, 2012.

[82] Yonggang Zhao, Yuanbiao Tan, Xuanming Ji, Zijie Xiang, Yue He, and Song Xiang. In situ study of cementite deformation and its fracture mechanism in pearlitic steels. *Materials Science and Engineering: A*, 731:93–101, 2018.

[83] Gh Ali Nematollahi, Blazej Grabowski, Dierk Raabe, and Jörg Neugebauer. Multiscale description of carbon-supersaturated ferrite in severely drawn pearlitic wires. *Acta Materialia*, 111:321–334, 2016.

[84] Soodabeh Azadehranjbar, Bingqiang Wei, Dongyue Xie, Kaisheng Ming, Jian Wang, and Jeffrey E Shield. Strength and plasticity of lamellar vs. fibrous eutectic Mg–Al nanocomposites: An in-situ microcompression study. *Acta Materialia*, 206:116624, 2021.

[85] Haoxiu Chen, Lizhong Lang, Xiao Shang, Soumya S Dash, Yixiao He, Graham King, and Yu Zou. Anisotropic co-deformation behavior of nanolamellar structures in additively manufactured eutectic high-entropy alloys. *Acta Materialia*, 271:119885, 2024.

[86] Pengfei Zhang, Yanjun Zhou, Yahui Liu, Shaolin Li, Kexing Song, Jun Cao, Baoan Wu, Xin Li, Hanjiang Wu, Jihua Gu, et al. Strengthening mechanism of ultra-high strength Cu–20Ag alloy wire induced by cumulative strain. *Materials Science and Engineering: A*, 855:143957, 2022.

[87] Yifei Huang, Chuanchu Su, Haojie Lu, Yu Wang, Yanhu Wang, and Xizhang Chen. CoFeNi twisted wire+ Al wire arc additive manufacturing of AlCoFeNi eutectic and near-eutectic high-entropy alloys. *Journal of Materials Research and Technology*, 2024.

[88] Jin-Xi Chen, Tong Li, Yan Chen, Fu-Hua Cao, Hai-Ying Wang, and Lan-Hong Dai. Ultra-strong heavy-drawn eutectic high-entropy alloy wire. *Acta materialia*, 243:118515, 2023.

[89] Toshihiko Teshima, Makoto Kosaka, Kohsaku Ushioda, Norimitsu Koga, and Nobuo Nakada. Local cementite cracking induced by heterogeneous plastic deformation in lamellar pearlite. *Materials Science and Engineering: A*, 679:223–229, 2017.

[90] Lisa Ventelon, François Willaime, Emmanuel Clouet, and David Rodney. Ab initio investigation of the peierls potential of screw dislocations in bcc fe and w. *Acta Materialia*, 61(11):3973–3985, 2013.

[91] Lisa Ventelon and F Willaime. Generalized stacking-faults and screw-dislocation core-structure in bcc iron: a comparison between ab initio calculations and empirical potentials. *Philosophical Magazine*, 90(7-8):1063–1074, 2010.

[92] Lei Zhang, Gábor Csányi, Erik van der Giessen, and Francesco Maresca. Efficiency, accuracy, and transferability of machine learning potentials: Application to dislocations and cracks in iron. *Acta Materialia*, 270:119788, 2024.

[93] Atsushi Togo, Laurent Chaput, Terumasa Tadano, and Isao Tanaka. Implementation strategies in phonopy and phono3py. *J. Phys. Condens. Matter*, 35(35):353001, 2023.

[94] Yong-Jie Hu, Aditya Sundar, Shigenobu Ogata, and Liang Qi. Screening of generalized stacking fault energies, surface energies and intrinsic ductile potency of refractory multicomponent alloys. *Acta Materialia*, 210:116800, 2021.

4

5

Microstructural and Mechanical Anisotropy in Pressure-Assisted Sintered Copper Nanoparticles

5.1 Abstract

The mechanical strength of sintered nanoparticles (NPs) limits their application in advanced electronics packaging. In this study, we explore the anisotropy in the microstructure and mechanical properties of sintered copper (Cu) NPs by combining experimental techniques with molecular dynamics (MD) simulations. We establish a clear relationship between processing conditions, microstructural evolution, and resulting properties of pressure-assisted sintered Cu NPs. Our findings reveal that pressure-assisted sintering induces significant anisotropy in the microstructure, as evidenced by variations in areal relative density and the orientation distribution of necks formed during sintering. Specifically, along the direction of applied stress, the microstructure exhibits reduced variation in areal relative density and a higher prevalence of necks with favorable orientations. The resulting anisotropic mechanical properties, with significantly higher strength along the pressure direction compared to other directions, are demonstrated through micro-cantilever bending tests and tensile simulations. This anisotropy is further explained by the combined effects of strain localization (influenced by areal relative density) and the failure modes of necks (determined by their orientation relative to the loading direction). This work provides valuable insights into the analysis of sintered NPs microstructures and offers guidance for optimizing the sintering process.

Keywords: Sintered Cu nanoparticles, Micro-cantilever bending tests, anisotropy, 3D reconstruction, Molecular dynamics simulation

5.2 Introduction

Wide band gap (WBG) materials like silicon carbide (SiC) and gallium nitride (GaN) have been widely used in power modules owing to their excellent electric and thermal properties and performance [1–3], especially when operated at high breakdown voltages and high temperatures ($< 200\ ^oC$). Traditional interconnect bonding materials like Sn- or Pb-based solder alloys face limitations in power devices due to the low melting point, limited thermal conductivity and insufficient creep resistance [4–7]. In recent years, sintered silver (Ag) and copper (Cu) nanoparticles (NPs) interconnects are proposed as an alternative to solder alloys in the die-attachment of WBG semiconductors because of their low sintering temperature, high melting temperature and high electrical and thermal conductivity [8–12].

Despite these advantages, the anisotropy of the microstructure and mechanical properties of sintered Cu NPs poses a critical challenge for the bonding quality and long-term reliability of joints. NPs sintering is characterized by low sintering temperatures (less than $300\ ^oC$), short sintering times, and the assistance of uniaxial compressive stress [13]. This process, while efficient, inherently induces anisotropy in the sintered microstructure. Many experiments have highlighted the anisotropy

in micrometer-sized particles, such as alumina and Cu, when sintered with uniaxial compressive stress [14–16]. The sintered bodies exhibit greater shrinkage in the direction of the applied stress. At the microscale, this anisotropy originates from the evolution and orientation change of the pores [14]. The aspect ratio of the pores increases after sintering, and the orientation of the long axis tends to align parallel to the stress direction [17, 18]. Additionally, the constraints imposed by the substrate on particle merging affect the shape of the pores [19]. For Cu NPs, the sintered microstructure is highly porous, and the anisotropy is even more pronounced under these conditions. From a bonding quality perspective, this anisotropy can lead to uneven stress distribution within the joint, particularly during thermal cycling or mechanical loading [16], potentially compromising the structural integrity. Furthermore, from a reliability viewpoint, local variations in mechanical properties can influence crack initiation and propagation pathways [20], significantly affecting the long-term performance. These concerns are especially critical for SiC devices, which often operate under extreme conditions, including high temperatures and power densities. Addressing the anisotropy in the microstructure and mechanical properties of sintered Cu NPs is therefore essential. Given the sintering conditions for NPs, the resulting microstructure after sintering is highly porous, and severe anisotropy is expected [15].

The high porosity and small feature sizes of sintered NPs pose challenges for mechanical property testing and microstructure characterization. Scanning electron microscopy (SEM) and transmission electron microscopy (TEM) are widely used for microstructure observation, such as examining pore shapes and necks formed during sintering. Zuo et al. [21] studied the microstructure evolution of Cu NPs during pressureless sintering. The grain growth and grain boundary movement were clearly observed using TEM at elevated temperature. Since the spatial features of particle packing and pore distribution strongly influence the electrical, thermal, and elastic properties of sintered NPs, three-dimensional (3D) characterization of the microstructure is crucial. Two methods for 3D reconstruction have been reported: focused ion beam combined with scanning electron microscopy (FIB-SEM) [22–24], and synchrotron X-ray computed tomography [25, 26]. Through 3D reconstruction, the inter-particle necks can be identified, and the evolution of the microstructure can be described using metrics such as pore numbers [23], mean intercept length [24], and particle shape [25]. Areal relative density curves have also been proposed to illustrate variations in local microstructure [22, 27].

The mechanical properties of sintered NPs are typically measured with micropillar compression tests [28] and micro-cantilever bending tests [29–31]. Chen et al. [29] studied the effect of micro-cantilever size (20, 10 and 5 μm in width) on fracture toughness of sintered Ag NPs by micro-cantilever bending tests, revealing that fracture toughness decreases as specimen size decreases. Recently, we

studied the effect of depth of pre-crack on the fracture toughness of sintered Cu NPs by micro-cantilever bending tests [31]. Results show that microscopic fracture toughness presents a limited relationship with notch depth.

Due to difficulties in experiments, simulation methods spanning multiple length and time scales are applied to investigate various aspects of NPs sintering. Discrete element modelling (DEM) primarily focuses on the particle packing [19] and neck formation during sintering [32]. Specifically, Wonisch et al. [33] analyzed the anisotropic microstructure of sintered micro-sized particles induced by external stress using both experiments and DEM, identifying the size of contact areas in different directions as a crucial factor. The grain growth and evolution of pores during sintering process are also studied using phase field simulation in both two-dimensional (2D) [34] and 3D [35, 36] models. The relationship between microstructure and properties is modeled using finite element method (FEM) [37, 38] and phase field methods [39]. The porous structure for the simulation are from SEM images [37] and stochastic modeling [38, 39].

Molecular dynamics (MD) simulations have been used to study the NPs sintering process and subsequent mechanical tests. Two-particle models are extensively utilized to examine atom diffusion and neck formation during sintering [40–42]. Multi-particle sintering has also been explored with MD [43–45]. Guo et al. simulated the densification process of a high-entropy alloy to show the influence of initial particle packing [44]. The accuracy and effectiveness of the multiple particles sintering model were verified using a phase-field model. This method was also applied to investigate the influence of initial particle morphology on the sintering of gold NPs [45]. Due to the limited timescale of MD simulations, the contributions of diffusion mechanisms, such as surface diffusion and bulk diffusion, are underestimated, and densification in these simulations is mainly caused by plastic flow under stress. However, MD simulations are expected to yield physically meaningful results considering the short sintering time and low temperature characteristic of NP sintering. Additionally, Zuo et al. [21] demonstrated that without external stress, grain growth and grain boundary mobility are insignificant at 220ºC.

This paper aims to elucidate the relationship between sintering methods and microstructural anisotropy, as well as the anisotropy of mechanical properties, through a combination of experiments and simulations. Section 2 details the experimental and simulation methods. In Section 3, the microstructure of sintered Cu NPs from FIB-SEM reconstruction, precession electron diffraction and MD simulations are analyzed based on areal relative density and neck formation during sintering. The origin of microstructural anisotropy is discussed. In Section 4, the strength of sintered NPs is measured by micro-cantilever bending tests and tensile simulations, and the anisotropic strength of sintered Cu NPs is connected with their microstructure.

5.3 Experimental and simulation procedure

5.3.1 Cu nanoparticles and sintered sample preparation

The Cu paste used in this study was prepared by a reductive pretreatment method [46]. Fig. 5.1(a) presents an SEM image of the Cu NPs, showing them as quasi-spherical and uniformly distributed with an average size (diameter) of 150 nm [Fig. 5.1(b)]. Energy dispersive spectroscopy (EDS) was conducted on the cross-section, confirming the sintered Cu NPs is almost pure with minimal oxidation, as shown in Fig. 5.1(c). A die-attach structure (Cu dummy die, sintered Cu NPs layer, and Cu substrate) was prepared using pressure-assisted sintering technology. As illustrated in Fig. 5.1(d), the Cu paste was firstly transferred onto the Cu substrate with a stencil thickness of 100 μm using a screen printer and a flat scraper. Second, the substrate was heated to 120°C for 5 minutes to evaporate the organic solvent after removing the stencil. Then, the Cu dummy dies were attached to the substrates using a vacuum pick-up pen. Pressure-assisted sintering was conducted in a nitrogen atmosphere (Applied Microengineering Ltd., UK). The Cu paste was sintered for 10 minutes at 250°C under 25 MPa uniaxial stress in a reducing atmosphere (5% H_2/N_2). Finally, the sintered sample [Fig. 5.1(e)] was removed from the furnace after cooling down. The schematic diagram of the die-attach structure in power electronics is shown in Fig. 5.1(f).

5.3.2 FIB-SEM tomography

FIB-SEM tomography, an SEM-based technique, enables advanced characterization and improved understanding of 2D results. Here, we used FIB-SEM tomography to characterize the void distribution in sintered Cu NPs. The methodology involved using a dual-beam FEI Helios G4 CX FIB-SEM system for imaging and slicing to reconstruct 3D structures. Before ion milling, a platinum protective layer, approximately 1 μm thick, was deposited on the region of interest to prevent damage during ion milling. Subsequently, fiducial markers were strategically placed on the samples, allowing for real-time drift correction between successive milling operations. To facilitate FIB-SEM tomography, the sample was tilted at 52°, enabling milling perpendicular to the surface. Additionally, a U-shaped trench was milled alongside the area of interest to create space for redepositing material removed during tomography. The FIB slicing was conducted at an accelerating voltage of 30 kV and 40 pA, and SEM images were taken at 10 kV using an SE detector. The Auto Slice and View software (ASV4) was utilized to automate the tomography process by estimating the next slice position based on the top view image.
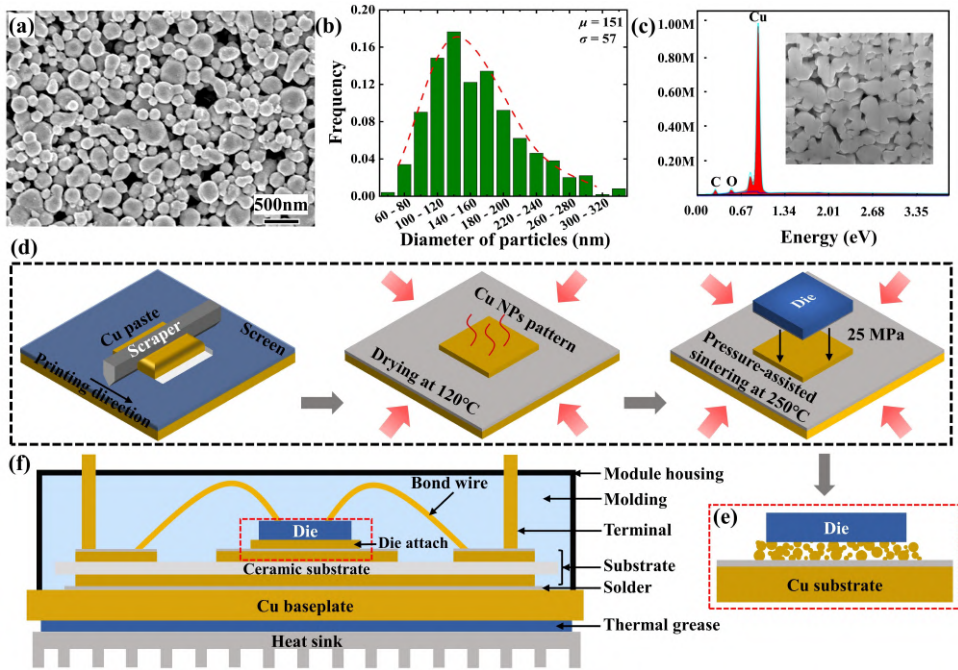
Figure 5.1: (a) SEM image of the Cu NPs; (b) size (diameter) distribution; (c) EDS Spectrum of the sintered Cu NPs; (d) pressure-assisted sintering technique; (e) schematic diagram of sintered die-attach structure; (f) schematic diagram of the die-attach structure in power electronics.

5.3.3 Precession electron diffraction

To characterize the grain orientation of sintered Cu NPs, precession electron diffraction (PED) [47–54], a state-of-the-art transmission electron microscopy (TEM)-based technique was employed in this study. PED was performed using a JEM-2200FS (JEOL) transmission electron microscope (TEM) operating at 200 kV and equipped with the ASTAR system (Nanomegas) [53]. The microscope was operated in nanobeam diffraction (NBD) mode with the smallest spot size and a condenser aperture of 10 μm. The probe diameter was approximately 1 nm with a convergence angle of 2 mrad. A precession frequency of 100 Hz and a precession angle of 0.5° were applied during nanobeam scanning. This configuration reduces dynamical diffraction effects and enables reliable orientation and phase identification by integrating intensities over multiple diffraction conditions. By tilting the incident electron beam in a conical motion, PED reduces dynamical diffraction effects and enhances the reliability of orientation and phase identification. Compared to conventional techniques such as electron backscatter diffraction (EBSD) with 50-100 nm [49] and transmission Kikuchi diffraction (TKD) with 10-20 nm [54], PED offers superior resolution down to 1 nm, sensitivity to weak reflections, and the ability to

analyze thin samples, making it particularly suitable for nanocrystalline materials. These advantages establish PED as a critical tool for detailed microstructural analysis and phase fingerprinting in advanced materials research.

5.3.4 Micro-cantilever bending tests

Micro-cantilever bending test is an effective technique for probing the mechanical properties of microscale samples [55, 56]. As shown in Fig. 5.2(a), three kinds of micro-cantilevers with different orientations with respect to the direction of external pressure during sintering were fabricated, i.e. 0° (perpendicular), 45°, and 90° (parallel). For each orientation, six specimens were prepared to ensure the reliability of the data. Fig. 5.2(b) illustrates that the fabrication process involved five steps: milling a notch with a low ion current (10 pA), creating U-shaped trenches with a large beam current (20 nA), tilting and milling the base with 3 nA, rotating and repeating on the other side, and forming the micro-cantilever by undercutting. The micro-cantilever was then polished with 1 nA to ensure symmetry and cleaned with 100 pA to minimize damage. A precise marking was made on the free end to establish a well-defined loading point. Fig. 5.2(c) shows a typical SEM image of the micro-cantilever. The micro-cantilevers were fabricated at the middle position of the die-attach layer. This choice was deliberate to ensure consistency in the microstructure and minimize variations caused by non-uniformities during sintering [57]. The middle region is more representative of the average sintering degree and microstructure, as the edges may experience different thermal and pressure conditions [58]. By focusing on this central position, the influence of local non-uniformity was reduced [59], leading to more reliable and reproducible mechanical property measurements. The micro-cantilever has a pentagonal cross-section. We chose this shape for two reasons: it provides more flexibility in selecting the location compared to a rectangular shape, and the stress distribution in a pentagonal cross-section is less affected by preparation inaccuracies, leading to more reliable mechanical property measurements [60, 61].

An in-situ nanoindenter setup from Alemnis AG (Switzerland) was utilized to perform micro-cantilever bending tests in a Zeiss Ultra55 FEG SEM chamber. Before conducting the bending tests, the SEM carefully positioned the indenter tip to the fiducial mark on the top surface of the micro-cantilever, as shown in Fig. 5.2(c). The quasi-static bending test is controlled by displacement. A constant load rate of 10 nm s^{-1} was applied for all micro-cantilevers until fracture occurred. The bending load was applied with a conospherical diamond tip (radius = 1 μm). Compared with the sharp-tipped indenter, such as the Berkovich indenter, the conospherical indenter with a spherical tip exhibited minimal indentation on the surface of the micro-cantilever [62].
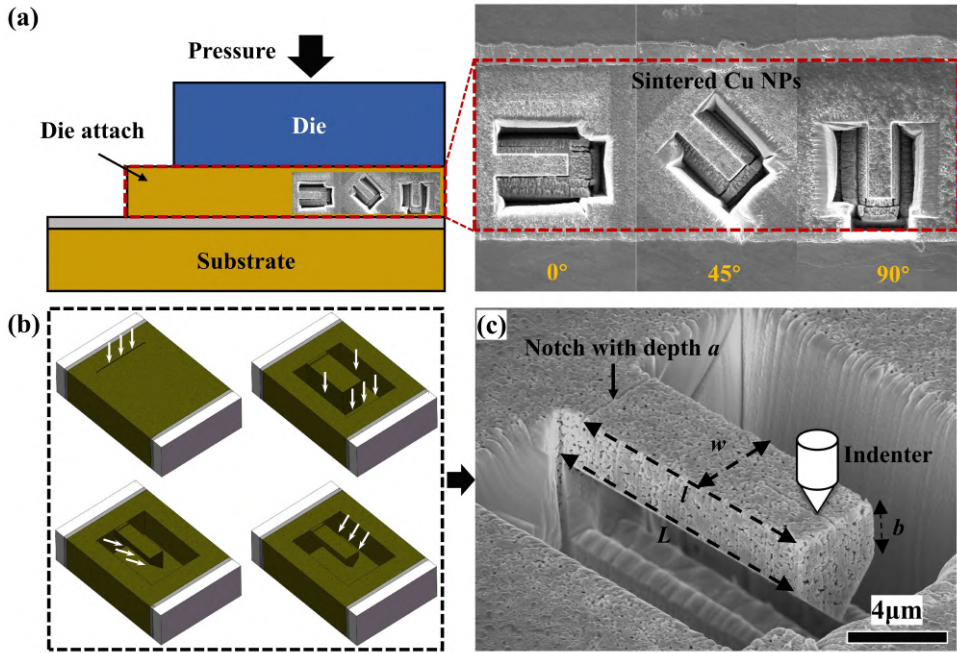
Figure 5.2: (a) Relationship of micro-cantilever orientations with pressure during sintering process; (b) FIB process for micro-cantilever fabrication; (c) SEM image of a micro-cantilever.

5.3.5 MD SIMULATIONS OF THE SINTERING PROCESS AND TENSILE TESTS

The sintering and tensile process were simulated by the MD method using Large-scale Atomic/Molecular Massively Parallel Simulator (LAMMPS) software [63]. The atomic configurations were visualized and analyzed with the Open Visualization Tool (OVITO) [64]. The Cu embedded atom method (EAM) interatomic potential proposed by Mishin et al. [65] is employed to describe the atomic interaction, which has been successfully applied in simulating various mechanical properties and microscopic phenomena in Cu, such as diffusion and grain boundary migration [66–68]. The melting point of bulk Cu within this potential is 1273 ± 30 K, which matches well with the experimentally observed value of 1358 K. The initial Cu particle model has the following characteristics: spherical shape, non-contact or point-contact interactions between particles, a total volume fraction of about 45%, random spatial orientation of each particle, and a particle size distribution that is comparable to experimental observation. To enhance computational efficiency, the particle diameter in the simulation was 3-12 nm, as shown in Fig. 5.3(b). Similar values (2-15 nm) have been used in previous MD simulations of the sintering process of Cu NPs [41]. Moreover, since Fig. 5.1(c) shows that the organic substances evaporated

during the sintering process, the influence of the organic binder in the sintering process is ignored.

The procedure for generating 3D models of Cu NPs is as follows:

1. Select a point in 3D space randomly to be the center of the Cu NPs. The particle radius is determined by a randomly generated number that follows a normal distribution

2. Validate the new particle by making sure it does not overlap with existing spheres considering the periodic boundary condition (PBC).

3. Assign a random orientation to the particle.

4. Repeat the procedure until the acceptance rate is very low.

5. Select particles randomly and expand them until they meet each other.

6. Execute energy minimization by employing the conjugate gradient (CG) algorithm.

Fig. 5.3(a) shows the resulting particle model of Cu NPs, which is color-coded with Adaptive Common Neighbor Analysis and has dimensions of roughly $450 \times 450 \times 450$ Å^3, consisting of around 240 particles and 3.6 million atoms. The initial relative density of the model is approximately 45%. Two types of external stresses (uniaxial and hydrostatic) during the sintering process are considered in MD simulation. The models sintered under uniaxial and hydrostatic stress are labeled as US and HS, respectively. The sintering method employed in US model is similar to sintering process in Section 2.1, while the HS model shares similarities with a constrained sintering method reported in [69].

The sintering process in the MD simulation includes three stages. Initially, the temperature increases to 523 K (in consistent to the experiments) with a Nose-Hoover thermostat at a speed of 2 K/ps. Subsequently, a uniaxial strain is applied to the US model, with strain rate of 1×10^9 s^{-1}. The pressure in the non-compressed direction is maintained at 0, corresponding to the sintering process in experiments which is unconstrained in the non-loading direction. The overall deformation along strain direction is 40%, according to the height changes of the powder during sintering in experiments (roughly from 1.8 μm to 1.3 μm). For the HS model, a hydrostatic stress is applied on all surfaces during the sintering process until the relative density reaches the same level as the US model. The loading rate is 0.2 MPa/ps. The sintering process finishes after approximately 800 ps. Finally, the temperature is kept at 523 K, the volume remains constant, and a relaxation period of 100 ps is applied to eliminate the additional stress caused by the high strain rate in the previous loading step. The US and HS models after sintering are shown in Figs. 5.3(c) and (d), respectively.

Due to the significant anisotropy of models after sintering on both microstructure and mechanical performance, directional terminology is introduced for convenience of description. The direction aligned with the stress direction during
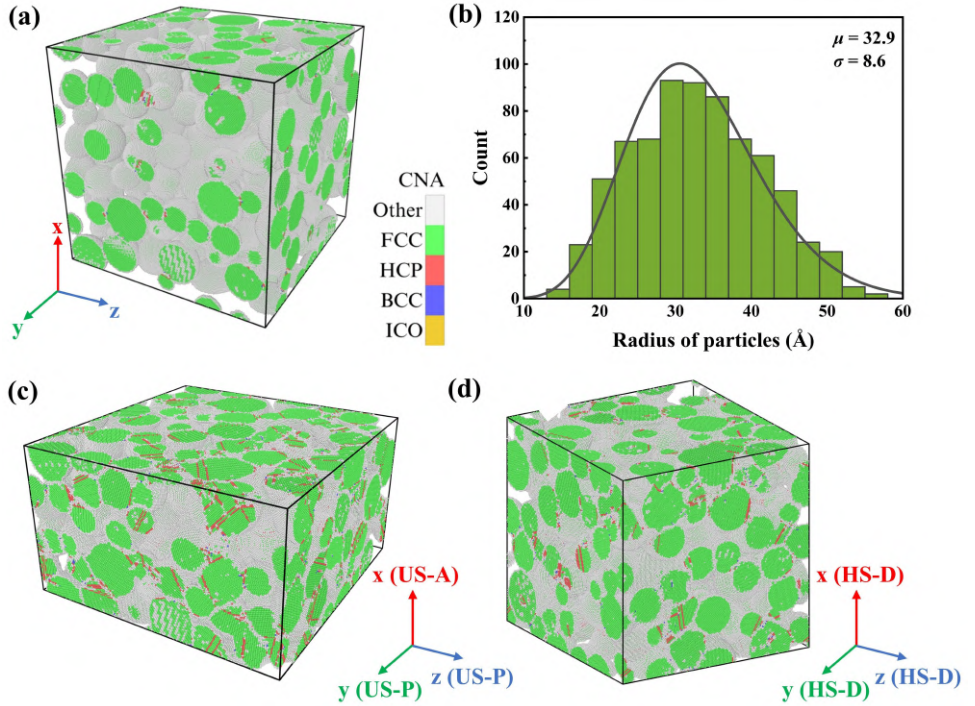
Figure 5.3: 3D Cu NPs model (a) before and after (c, d) sintering. (b) radius value distribution of Cu NPs; (c) after uniaxial stress sintering along the X-axis; (d) after hydrostatic stress sintering.

sintering is labeled as US-A, while the direction perpendicular to the stress direction during sintering is denoted as US-P, as shown in Fig. 5.3(c). Note that US-A and US-P represent the loading and observation directions. However, such distinction is not necessary for HS models, and all three orientations are labeled as HS-D, as shown in Fig. 5.3(d). Given the impact of the initial particle distribution on sintering and mechanical performance, three independent models with random initial particle packing are employed. Before simulating the tensile process, a relaxation procedure with variable box dimensions is implemented to ensure that the model has no residual internal stresses. The tensile simulation is under fully periodic boundary conditions using the NPT ensemble (constant number of particles, pressure, and temperature) and the temperature is maintained at 300 K (room temperature). The maximum tensile strain is 45% in this study, and the loading rate for the tensile simulation is set at 5×10^8 s^{-1}. This loading rate is commonly employed in literature [70]. The stress values in directions other than the tensile direction are maintained at 0.

5.4 Anisotropy in structural evolution during sintering

5.4.1 Areal relative density by FIB-SEM

Fig. 5.4(a) presents the image of the slicing and imaging area under FIB-SEM tomography. The dimension of the imaging area is around $10 \times 8 \ \mu m^2$ and the depth is around 4.5 μm. To obtain reliable and representative results, it is crucial to estimate the minimum volume size that must be reconstructed. The critical volume size, which is commonly called a representative volume element (RVE) or stochastic equivalent representative volume element (SERVE), has been extensively discussed in [71–75]. Given that the width and thickness of the micro-cantilevers are near 4 μm, the reconstructed volume of $4 \times 4 \times 4 \ \mu m^3$ is large enough to depict the real microstructure of sintered Cu NPs. 3D reconstruction was carried out by Avizo (Thermo Scientific) after serial image acquisition, which entailed alignment, image processing, and segmentation. Fig. 5.4(b) shows the image sequence generated via FIB-SEM. Once imaging is done, FIB milling can remove another layer of material using the same parameters to obtain a second image with SEM. By repeatedly performing this milling and imaging process, a 3D dataset of SEM images is created, with each image depicting a 25 nm thick section of the sintered Cu NPs. 200 images were obtained, and around 160 high-resolution images were used to finish the 3D construction. The 'thresholding' method was applied in this study [76, 77]. The optimal thresholds for the reconstruction were selected by comparing reconstructed models with the morphology of voids in SEM. Figs. 5.4(c) and (d) represent the sintered Cu NPs and the void volume, respectively.

Here, we define areal relative density as

$$D_r^{\text{areal}} = \frac{A^{\text{matter}}}{A^{\text{cross-section}}} \times 100\% \tag{5.1}$$

where A^{matter} and $A^{\text{cross-section}}$ are the area of the sintered Cu NPs domain and the cross-section, respectively. The areal relative density and its mean (μ) and standard deviation (SD, σ) of the 3D reconstructed model along different directions are measured, as shown in Fig. 5.4(e). The XY plane is perpendicular to the pressure, while the YZ and XZ planes are parallel to the pressure. For the SD of areal relative density, a significantly lower SD (0.8%) is obtained on XY cross-section, compared with 1.5% of YZ and XZ cross-sections. Meanwhile, the XY cross-section has a minimum areal relative density of 78%, which is greater than that of the YZ (73%) and XZ (74%) cross-sections. It is evident that the areal relative density of the porous structure is anisotropic. Therefore, pressure direction leads to a more uniform distribution of areal relative density, with a relatively high minimum area of cross-section compared to the other two directions.
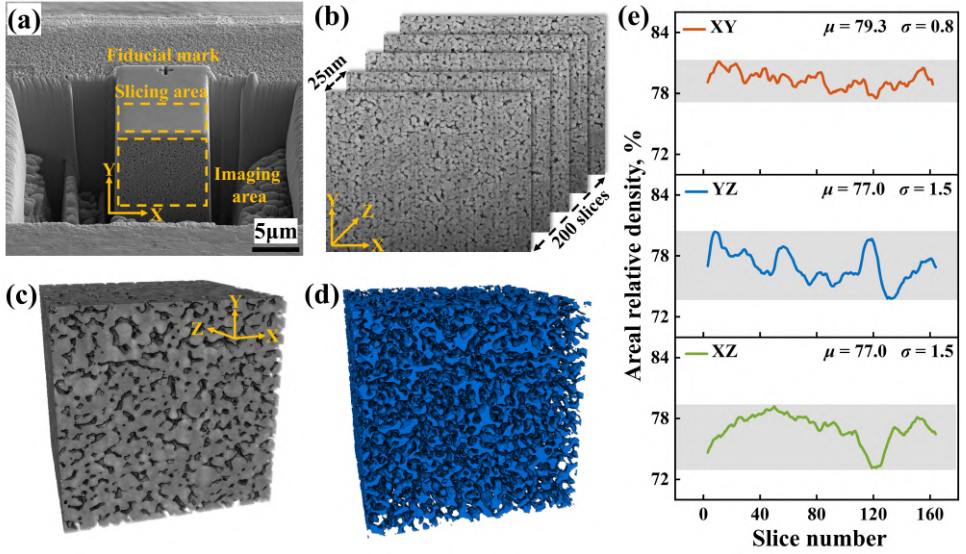
Figure 5.4: (a) FIB-SEM tomography image showing the slicing and imaging areas; (b) stacked SEM slices illustrating the consecutive slicing process; (c) sintered Cu NPs domain; (d) porous domain; (e) areal relative density in different directions

5.4.2 Areal relative density by simulation

The sintered structures obtained from the MD simulation are referred to Figs. 5.3(c) and (d). The final volumetric relative densities for models after simulated sintering is $67.4 \pm 0.7\%$ (under HS), and $68.3 \pm 1.7\%$ (under US). The density is slightly lower than that for experiments because of the limitations of MD simulations on time scales. As for the microstructure, the spherical shape of the particles is preserved after sintering and numerous sintering necks are formed. The majority of pores remain interconnected and the growth and merging of grains are not significant (as evidenced by the minimal change in grain count before and after sintering). The simulated structures are very similar to those reconstructed with FIB-SEM, as shown in Fig. 5.4(c), illustrating the reliability of this modeling approach. Since the atomic position in the model is discrete, the model is divided into slices with a thickness of 2 ∀ (about 1/30 of the average particle diameter) along the observation direction to calculate areal relative density. Within each slice, the ratio of the number of atoms to the volume of the slice is calculated, and this ratio is then scaled by the atomic density in a dense cubic Cu. Therefore, the areal relative density is defined as

$$D_r^{areal} = \frac{N^{slice} V^{atom}}{V^{slice}} \times 100\% \tag{5.2}$$

where $N^{\text{slice}} V^{\text{atom}}$ is the number of atoms inside the slice of the model. V^{slice} and V^{atom} is the volume of the slice and a single Cu atom in FCC crystal (a = 3.615 Å), respectively. Our tests show that this slice thickness can capture structural variations without being excessively sensitive, for example, to the influence of grain orientation.

To investigate the effect of the sintering method on the areal relative density distribution, we calculated the areal relative density distribution along different directions for sintered models obtained from the same particle model by different sintering methods. Fig. 5.5(a) is the schematic diagram of the view direction for measuring the areal relative density.

Figs. 5.5(b-d) show the changes of areal relative density along three directions, i.e. X, Y, and Z-axis. Each figure contains four curves corresponding to four sintering methods, i.e. under hydrostatic stress (HS) and uniaxial stress along the X-, Y-, and Z-axis (US-X, US-Y, and US-Z, respectively). Curves corresponding to US-A, which means for the model the observation direction is consistent with the direction of the stress during sintering, are with deeper color. The normalized coordinates are used as the horizontal axis due to the inconsistent dimensions of the sintered models. Three findings can be drawn from Figs. 5.5(b-d).

First, a certain degree of heritability in the location of the peaks and troughs of the curves is observed in areal relative density. That means for the same particle model sintered using different methods, when observing along the same direction, the positions of the peaks and valleys of areal relative density curves still exhibit a certain correspondence (although the relative height changes are different), showing the influence of the particle initial packing.

Second, the cross-sections in the US-A direction consistently exhibit a smaller SD and a higher minimum areal relative density value than those of cross-sections in the US-P direction for US models. That means during the sintering process, along the stress direction, the low-density regions caused by the random packing of particles are effectively filled. Surprisingly, US-A curves show lower peaks than US-P curves, indicating particles in high-density regions become more dispersed in the sintering direction. Close inspection of the atomic displacement reveals that due to higher strain and stress in the loading direction, particles require greater displacement along this axis to connect with other particles and bear the load, while along other directions particles have lower driven force for movement.

Third, the cross-sections in HS models generally show intermediate values between those of US-A and US-P for both areal relative density SD and minimum areal relative density. The deviation from the general trend, where the cross-sections of HS model exhibit a lower SD of areal relative density than US-A along the Z-direction, can be attributed to the low areal relative density of the US model compared to the HS model.
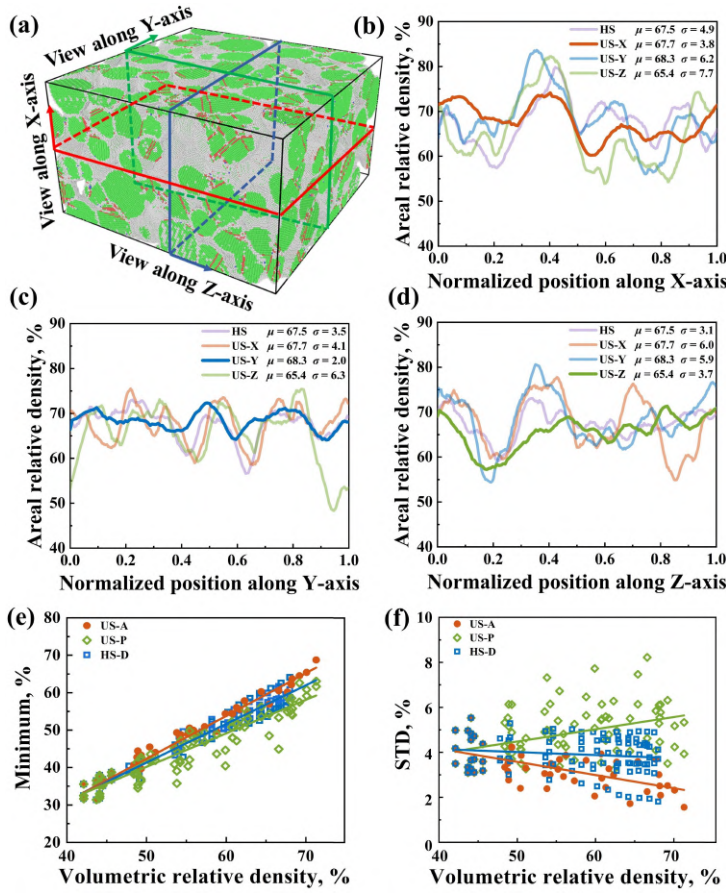
Figure 5.5: (a) Sintered model showing the orientations of cross-sections for measuring the areal relative density; (b-d) the changes of areal relative density with position along (b) X-axis, (c) Y-axis and (d) Z-axis under four different sintering conditions, namely, hydrostatic stress (HS) and uniaxial stress (US-X, US-Y, US-Z); (e) the minimum areal relative density versus volumetric relative density; (f) the SD of areal relative density versus volumetric relative density.

In order to quantitatively characterize the changes in these structures during sintering, we calculated the minimum values and SD of areal relative density of cross-sections along different directions for each model at various time points during the sintering process, as depicted in Figs. 5.5(e) and (f).

We found that as the bulk density rises during sintering, the minimum value of the areal relative density rises linearly. The slope of the fitted line for US-A in minimum areal relative density is slightly higher than that for US-P. The case of HS-D is between US-A and US-P. However, for SD of the areal relative density, the tendency is distinctly different for different sintering conditions and observation

directions. For the US-A direction, the SD decreases with the increase in bulk density. In contrast, the SD of cross-sections in the US-P direction increases with the rise in bulk density, indicating amplification of structural fluctuations along the direction perpendicular to the applied stress during the sintering process. For HS-D, SD remains nearly constant, implying that the fluctuations in the structure across different directions are at the same magnitude during sintering. Both the two properties along the US-P direction exhibit larger fluctuations than those for US-A, suggesting a more significant influence from the initial particle packing. The fluctuation range for HS-D falls between these two cases.

5.4.3 Grain orientation characterization

To investigate the effect of sintering pressure on grain orientation and void distribution, two TEM samples were fabricated from the sintered Cu NPs layer. One TEM sample was extracted perpendicular to the sintering pressure direction, aligning with the orientation of the 90° micro-cantilevers. The other one was extracted parallel to the sintering pressure direction, corresponding to the 0° micro-cantilever orientation. Precession electron diffraction (PED) was subsequently performed to characterize the grain orientation maps and void distributions of the two samples. The results are presented in Fig. 5.6. Figs. 5.6(a) and (b) depict the grain orientation maps for the perpendicular and parallel directions, respectively. The PED analysis demonstrates that the grain orientation shows no significant dependence on the applied sintering pressure. However, clear anisotropy is observed in the void morphology and particle deformation. In the perpendicular direction (Figs. 5.6(c, e)), the voids appear irregular and smaller, reflecting localized densification with minimal particle elongation. Conversely, in the parallel direction (Figs. 5.6(d, f)), the voids are larger and elongated, which can be attributed to the deformation of particles under uniaxial stress during sintering. The external pressure facilitates particle flattening and void coalescence along the loading direction, leading to an anisotropic void structure. These observations align with the findings discussed in Sections 3.1 and 3.2, where the pressure direction enhances the uniformity of areal relative density while reducing structural fluctuations. Specifically, the lower standard deviation of relative density along the pressure direction indicates a more stable and homogeneous microstructure. In contrast, the larger density fluctuations in the perpendicular direction reflect the significant influence of initial particle packing and localized void formation.

5.4.4 Formation of necks during sintering

The fusion between the particles plays an important role in the densification process. According to Ref. [78], the contact area between two particles is considered the sintering neck. In MD models, if atom A, belonging to particle P_A, is within the
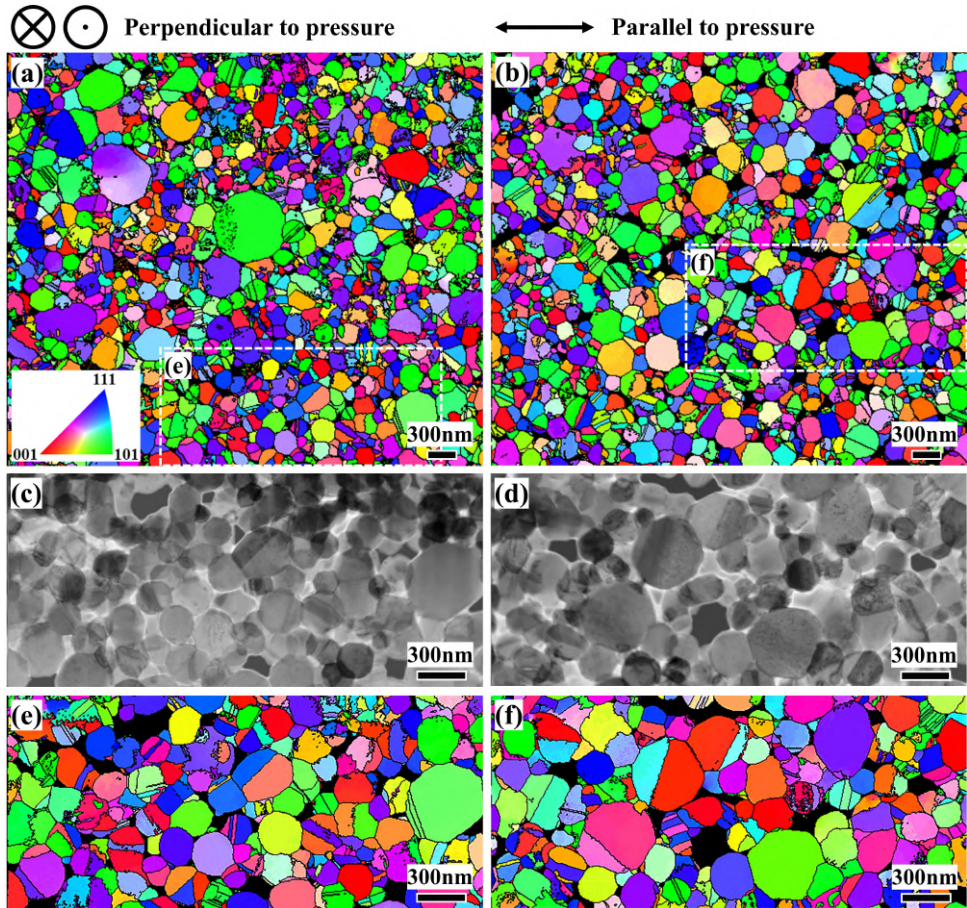
Figure 5.6: PED analysis of sintered Cu NPs under external pressure. (a) Grain orientation map of the the TEM sample aligned perpendicular to the sintering pressure, corresponding to the 90° micro-cantilevers. (b) Grain orientation map of the TEM sample aligned parallel to the sintering pressure, corresponding to the 0° micro-cantilevers. (c, d) Virtual bright-field images of the dashed regions in (a) and (b), respectively, revealing local grain morphology. (e, f) Corresponding orientation maps of the local regions shown in (c) and (d), respectively.

cutoff distance of atom B, which belongs to particle P_B, then both atom A and B are considered part of the sintering neck between P_A and P_B. The cutoff distance is set to 3.5 ∀ to ensure that all sintering necks are sufficiently large for meaningful measurement. Using this method, the shape of the necks before and after sintering under stress along the X-axis is shown in red in Figs. 5.7(a) and (b), respectively. Different particles are distinguished by different shades of gray. The shrinkage along the X-axis after sintering is about 40%. A significant rise in the number and volume of neck regions can be observed. After sintering, the fractions of atoms

that were labeled as "neck" increased from 4.6% to 14.8%. Moreover, the necks are interconnected to form a 3D network after sintering is completed, which is beyond the 2D model used in previous simulations of sintering.

To further determine the orientation of each sintering neck, the positions of the atoms for a single sintering neck are extracted, as shown in Fig. 5.7(c). We consider the neck to be a thin sheet with a significant difference between thickness and area, with the thickness direction representing the orientation of the neck. Using principal component analysis (PCA), the three orthogonal principal component (PC) vectors for the atomic positions are determined. The plane defined by PC1 and PC2 is the plane with the most dispersed atomic coordinates. PC3, which is perpendicular to this plane, is the direction with the least atomic dispersion, indicating the orientation of the sintering neck. Fig. 5.7(d) is a schematic diagram for calculating the angle θ between the neck orientation (PC3) and the X-axis. It is clear that when θ approaches 0, the neck is perpendicular to the given axis, while θ near 90° means the neck is parallel to the given axis.

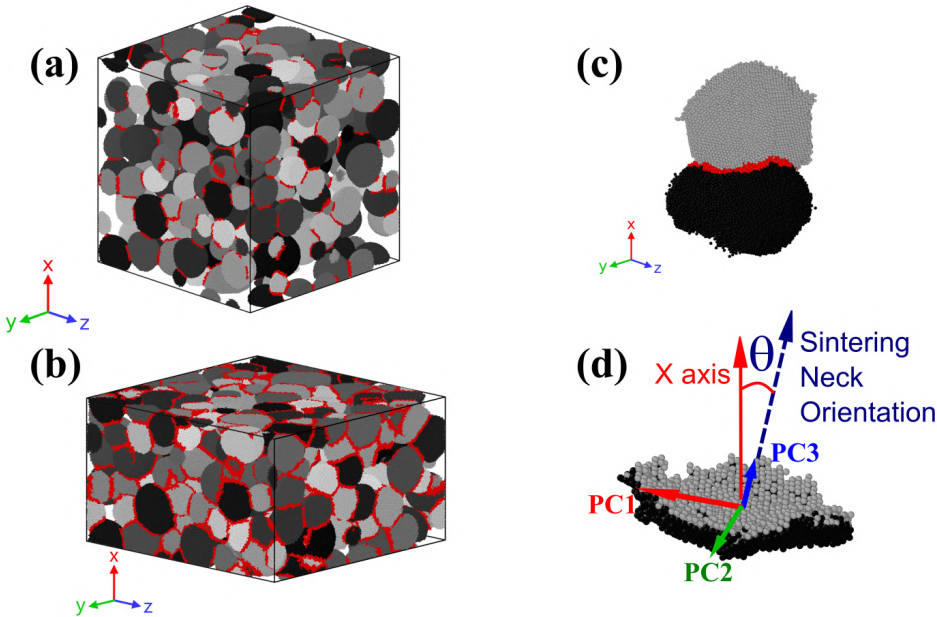Figure 5.7: Neck regions in MD simulation for (a) model before sintering and (b) model sintered under stress along X-axis. (c) A neck between two particles after sintering. (d) Principal component analysis for atoms location in a neck. The orientation is quantitatively calculated as the angle between the third principal component and X-axis.

It is important to note that, mathematically, the distribution of the angle of

a random vector in 3D space with a specific vector is not uniform. It is trivial to prove that for angle θ ranging in 0 to 90°, the probability density function $F(\theta)$ of the angle between a random vector and a fixed vector is

$$F(\theta) \propto sin(\theta). \tag{5.3}$$

Thus there is a much higher possibility for a vector to be perpendicular to a specific axis, rather than parallel to that.

A DEM study of ceramic sintering showed that the anisotropy flattening under stress has a substantial contribution to structure anisotropy [33]. Since the sintering of metal NPs is featured by low sintering temperature and short sintering time, the anisotropy induced by particle deformation is expected to be more significant. Here we use a 2D schematic to illustrate the effect of deformation caused by the uniaxial stress on the orientation of the neck formed during sintering. Fig. 5.8(a) shows two particles before sintering. θ is the angle between the normal of the initial contact surface and the stress direction. Here,

$$\tan \theta = \frac{a}{b}, \tag{5.4}$$

where a and b are the dimensions of the initial sintering neck in the parallel and perpendicular directions to the loading, respectively. After uniaxial stress-assisted sintering, the particle shape significantly contracts along the direction of the uniaxial stress with a strain of ε, while Poisson expansion occurs in the other directions, as shown in Fig. 5.8(b). The neck also grows during sintering. Then θ' can be estimated as

$$\tan \theta' = \frac{k \cdot a(1-\varepsilon)}{k \cdot b(1+\nu\varepsilon)}, \tag{5.5}$$

where k describes the uniform growth of the sintering neck dimensions in all directions, and ν is the Poisson's ratio of the bulk material. It should be noted that the strain during sintering should be smaller than the shrinkage deformation along the stress direction, as both particle deformation and densification contribute to the shrinkage. Using this method, the orientation distributions of necks considering particle deformation are calculated, as shown in Fig. 5.8(c). The black curve, which is for particles before deformation, corresponding to the distribution described by Eq. 5.3. The peak of angle distribution significantly shifts to low angle region as particle strain increases, meaning that after large deformation, necks tend to be perpendicular to the stress direction geometrically.

The orientations of the necks in the MD models sintered under stress along the X-axis are analyzed. The US-X with deformation of 40% [Figs. 5.9(a-c)] and 50% [Figs. 5.9(d-f)] contain 742 and 883 necks, respectively. The model with 50% deformation is analyzed here to better show the effect of uniaxial compression
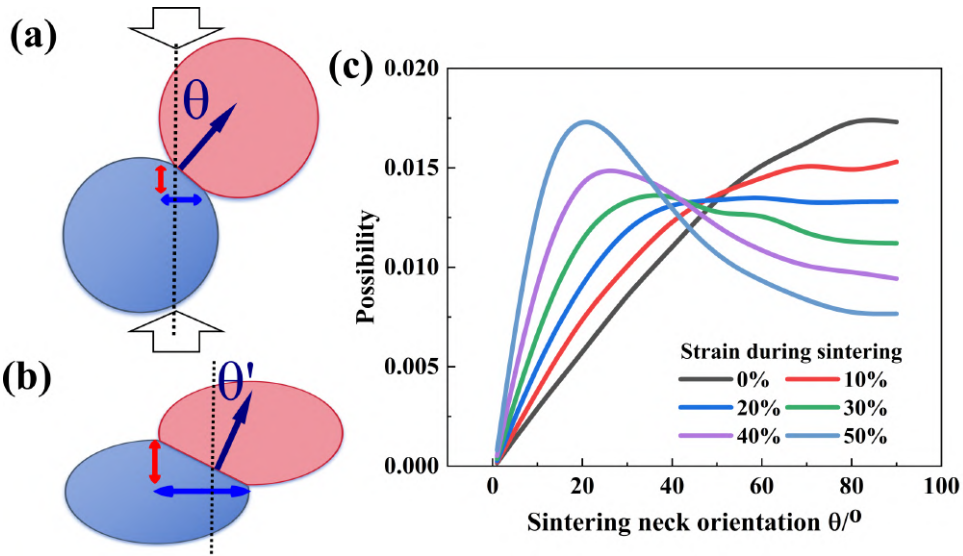
Figure 5.8: Schematic illustration of the effect of particle deformation on sintered neck orientation. (a) Two particles with initial contact before sintering. (b) A neck formed between two deformed particles. (c) Distribution of θ for particles with various strain derived from the 2D model.

during sintering on the microstructure. Figs. 5.9(a, d), (b, e), and (c, f) are for the neck orientations with respect to X-, Y-, and Z-axis, respectively. In each figure, the histogram counts the number of necks with different angles to the axis. The scatter plot shows the number of atoms contained in the necks with different orientations. The size of marks in scatter plots is also adjusted according to the number of atoms. The distribution curves for the angles between randomly oriented vectors to the axis (Eq. 5.3) are shown with a red solid line in each histogram for reference. In Figs. 5.9(a) and (d), the distribution of the neck orientations derived from Eq.5.5 are shown in blue curves. In the calculation, the strain of each particle is considered as half of the deformation along the X-axis and $\mu = 0.3$. Three points can be drawn from the figure.

1. For the orientation of necks concerning the direction of the uniaxial stress, here X-axis, the histogram shows that the number is higher between 0 and 50° than the reference line. For the orientation of the sintered neck along the Y and Z axes, the number is higher near 90°. This indicates that along the X-axis, more sintered necks are present perpendicular to the X-axis or at an angle of less than 50°, while in the other two orientations, most of the sintered necks are close to parallel to this orientation.

2. Large dots in the scatter plots corresponding to the X-axis are clustered in the angle range of 10 to 45°, while for the plots of the Y- and Z-axis, the dots
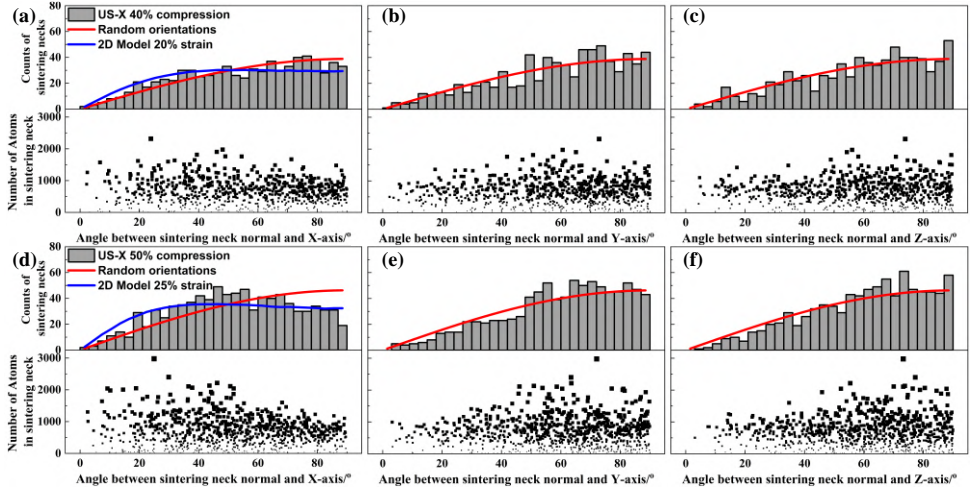
Figure 5.9: Statistics on sintering necks orientation (histograms) and size (scatter plots). (a-c) are for model with 40% deformation and (d-f) are for model with 50% deformation along X-axis during sintering. The angle shown in (a,d), (b,e), and (c,f) are between neck normals and X-, Y-, and Z-axis, respectively. Red reference curves show the angle distribution for randomly oriented vectors. Blue lines are derived from Eq. 5.5.

representing a larger number of atoms are clustered in the range of 60 to 90°. This suggests that sintered necks oriented close to perpendicular to the stress direction (here the X-axis) grow larger (compared to those parallel to the X-axis).

3. By comparing models experiencing 40% versus 50% deformation, the effect of deformation strain on the formation and growth of necks is revealed. With extra 10% compression, both the number and size of necks at an angle of 20 to 50° to the X-axis rise significantly, while there is no such tendency for the Y- and Z-axes.

The orientation of the sintered necks mainly originates from the flattening of the particle shape under uniaxial stress. In Ref. [33], the authors state that the particle flattening induced by uniaxial stress is anisotropic, with particles having a larger size and surface area perpendicular to the stress direction. The trend can be seen by comparing Fig. 5.8(a) and (b). The difference between the solid blue line and the actual distribution is mainly caused by the non-uniform strain distribution during sintering. Another reason for the distribution of neck orientations is the high body shrinkage along the direction of the sintering stress. Along the direction of the stress, the particles have more opportunities to contact each other thus more necks form.

5.5 Mechanical properties of sintered NPs and discussion

5.5.1 Micro-cantilever bending tests

Due to the limitations of FIB in preparing specimens with different orientations, the cross-section of the cantilever beam in this study is not rectangle. In our previous work, the fracture toughness of sintered Cu NPs was measured with standard micro-cantilevers as 3.2 MPa·m$^{1/2}$ [31], which aligns well with other reports [29]. Figs. 5.10(a-c) show the load-displacement curves obtained from micro-cantilever bending tests. The initial elastic loading parts matched well across specimens, but some scatter appeared at larger displacements due to slight differences in sample dimensions. The maximum load values F_{max} were retrieved from the peak points of the load-displacement curves. As depicted in Fig. 5.10(d), the maximum load and SD of 0º, 45º, and 90º micro-cantilevers are 203 ± 20 μN, 266 ± 68 μN, and 286 ± 36 μN, respectively. Since the specimens are essentially the same size, F_{max} is proportional to the fracture strength. The 90º micro-cantilevers, in which the prefabricated notch is perpendicular to the uniaxial stress during sintering, show 41% higher strength than 0º micro-cantilevers. The 45º micro-cantilevers exhibit slightly lower strength than the 90º micro-cantilevers, and the values are dispersed in a large range. The slopes of the load-displacement curves indicate the degree of densification of the specimen in the loaded direction, so we also calculated the slopes as the effective modulus. For 0º, 45º, and 90º micro-cantilevers, the modulus are 0.32 ± 0.04 μN·nm^{-1}, 0.42 ± 0.06 μN·nm^{-1}, and 0.45 ± 0.05 μN·nm^{-1}, respectively. The value for 90º micro-cantilevers is slightly higher than that for 45º micro-cantilevers, and significantly higher than that for 0º micro-cantilevers. Intuitively, we expect the mechanical property of 45º micro-cantilevers to be between those of 0º and 90º, following the rule of mixtures. The high toughness measured on 45º micro-cantilevers which is beyond expectation will be discussed in Section 4.3.

5.5.2 Toughness from MD simulation

Three independent sintering models were used for the simulations, resulting in nine MD models subjected to uniaxial stress and three models to hydrostatic stress. Tensile simulations were then conducted in the X, Y, and Z directions for the nine sintered models, generating 27 stress-strain curves. For the three models sintered under hydrostatic stress, the tensile tests produced nine stress-strain curves.

To characterize the microstructure and mechanical behavior, we use a model sintered under a stress along the X-axis as an illustrative example, shown in Fig. 5.11(c). The models under 40% tensile deformation along the X, Y, and Z axes are depicted in Figs. 5.11(a-c), respectively. Fracture is observed in the models stretched along the
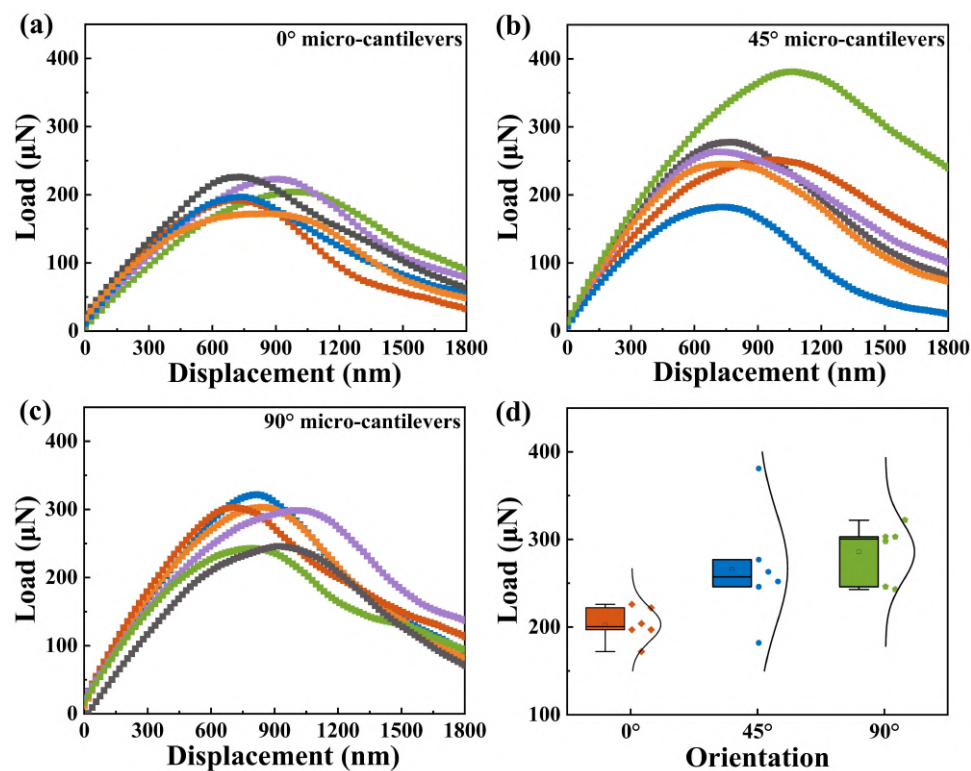
Figure 5.10: Load-displacement curves of (a) 0°; (b) 45°, (c) 90° micro-cantilevers; (d) maximum loads of micro-cantilevers with different orientations.

Y and Z axes, which is also reflected in the stress-strain curves [Fig. 5.11(d)]. The curve corresponding to tensile stress along the X-direction shows higher tensile strength than those for the Y and Z directions, matching well with experimental results. The toughness of the sintered Cu NPs models is related to the areas under
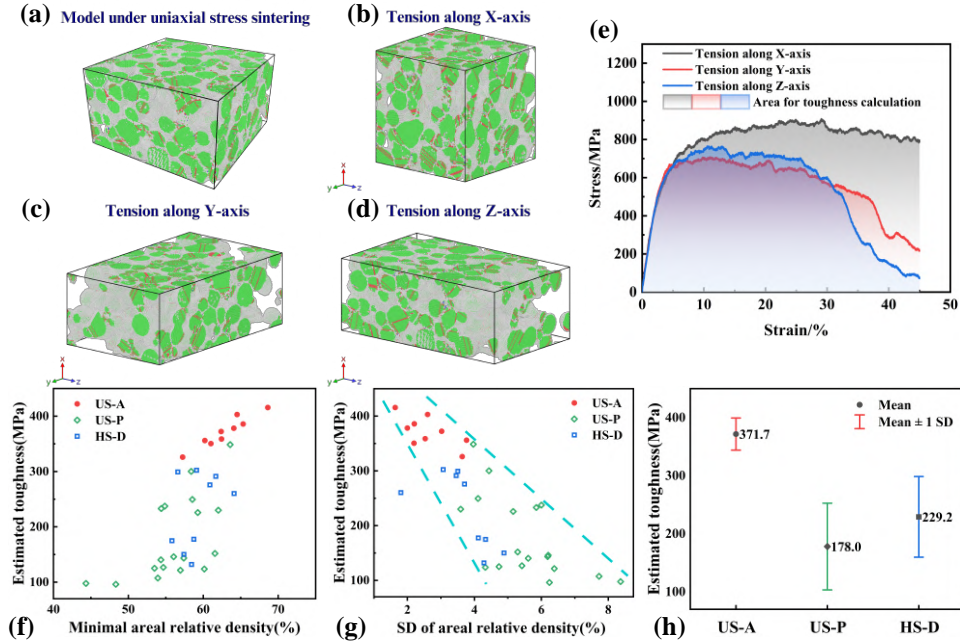

Figure 5.11: (a) Cu NPs model sintered under uniaxial stress along the X-axis. Atoms are colored according to its local structure. (b-d) Sintered model after 45% tensile deformation along (b) X-axis, (c) Y-axis and (d) Z-axis. (e) Stress-strain curves for tensile deformation along the three axes. The shaded area under each curve was used to calculate the tensile toughness. Two features describing the microstructure are connected with the estimated toughness: (f) minimum and (g) standard deviation of areal relative density. (h) Toughness for tensile along different directions. US-A(US-P) refer to the direction along(perpendicular) to the stress direction during sintering. HS-D refers to models sintered under hydrostatic stress. The dash lines in (g) are guide to eyes.

the stress-strain curves, calculated as follows:

$$G_f = \int_0^{\varepsilon_f} \sigma \, d\varepsilon, \tag{5.6}$$

where ε_f is the strain corresponding to failure and σ is the tensile stress [79]. The toughness here indicates the capacity for energy absorption during plastic deformation, not the fracture toughness. The unit for toughness is MPa or MJ·m^{-3}.

The fracture toughness estimated from the 36 stress-strain curves is connected to features of areal relative density. Fig. 5.11(f) illustrates that toughness increases

rapidly when the minimal areal relative density exceeds 60%. Even with similar minimal areal relative density, the toughness for tensile stress along the sintering direction (US-A) is much higher than that for US-P and HS-D. In Fig. 5.11(g), directions with smaller SD exhibit higher toughness. Moreover, a small SD value indicates a small variance in toughness. A direct comparison of toughness for US-A, US-P, and HS-D is shown in Fig. 5.11(h). Along the direction of sintering stress (US-A), the toughness is twice that of US-P. The toughness of HS-D is close to the average values in the three directions of the model sintered under uniaxial stress.

5.5.3 Effect of microstructural anisotropy on mechanical performance

Experimental and MD simulations reveal the anisotropy of the sintered structure in terms of surface density distribution and sintering neck orientation. The influence of the minimal areal relative density on mechanical properties is evident. Under uniform deformation, locations with small cross-sections are prone to stress concentrations, akin to the necking observed in general tensile deformation. Moreover, since Cu NPs are at the nanoscale, dislocation generation and multiplication are suppressed, and work hardening can hardly contribute to the strength of regions with high strain. Thus, strain localization at cross-sections with small areas is self-promoting, limiting mechanical performance. Long et al. [80] proved the effect of strain localization on the mechanical properties of sintered NPs.

For a homogeneous dense structure, stress concentration is bound to occur at the minimum areal relative density. For sintered Cu NPs, however, the stress distribution under uniform strain is strongly dependent on the porous structure and the position with minimal area is not necessarily the most dangerous region. The MD simulations of the tensile process of sintered Cu NPs show that fracture does not always occur at the cross-section with minimal areal relative density. SD is not sensitive to extreme values but describes the homogeneity of the material distribution for porous structures, complementing the minimal areal relative density. For structures with similar bulk relative densities, those with smaller SD have a lower possibility for strain localization and thus better mechanical properties. This conclusion is also supported by FEM [81] and phase field [82] simulations of tensile deformation of porous structures.

In other studies, it has been observed that the aspect ratio of pores increases after sintering and pores mainly align along the direction of the stress. The presence of elongated pores along the stress direction leads to smaller fluctuations in areal relative density in that direction compared to larger fluctuations in other directions. Therefore the anisotropy of pore shape reported before is consistent with the differences in directional SD of areal relative density we observed. For 3D interconnected pores, as shown by the 3D reconstruction, 2D interface obser-

vation is insufficient to fully display their characteristics. Here, we point out that SD of areal relative density is a reliable indicator for the quantitative description of 3D porous structures. Additionally, using SD as a measurement provides an alternative explanation for the size effect of porous structures [83]. For the same pore distribution, the areal relative density of smaller samples is more significantly affected by the pores, resulting in a higher SD. Multiple reports indicate that after high-temperature aging, accompanied by an increase in pore size, the mechanical properties of sintered Ag decline even if the relative density remains unchanged or increases. This is also consistent with the conclusions drawn here.

From another perspective, the anisotropy of sintered NPs can be explained by difference of failure mode. In the experiments conducted in [84], two primary failure modes were observed: tensile fracture and shear fracture. Since the necks are the weakest regions in the material, it can be inferred that the failure mode is related to the orientation of these necks. Due to the good plasticity of Cu, the fracture surfaces in the micro-cantilever bending tests did not completely separate, allowing only the observation of the fracture surfaces.

In MD simulations, these two fracture modes are also observed. For the model sintered under stress along the X-axis, the typical fracture surfaces during tensile deformation along X-axis (US-A) and Y-axis (US-P) are shown in Figs. 5.12(a) and (b), respectively. Atoms from different particles are color-coded, and the overall deformation of the model is indicated below each image. The total deformation along the tensile direction at 30% strain is marked on each particle. On the right side, the atomic structures before and after 30% deformation are shown, analyzed using CNA, with the surface amorphous layer removed for clarity. Red indicates the hexagonal closest packed (HCP) structure, corresponding to stacking faults in Cu.

In Fig. 5.12(a), the sintering neck is almost perpendicular to the tensile direction, resulting in uniform deformation across the particles (each particle contains many stacking faults), indicating tensile fracture. In Fig. 5.12(b), the sintering neck is nearly parallel to the tensile direction, resulting in significantly higher deformation in the green particle compared to the overall deformation value, while the red particle shows less deformation. At the fracture site, many atoms adhere to other particles, suggesting the fracture is by shearing at the neck.

Considering a sintering neck with an orientation angle θ and area A, as shown in Fig. 5.8, when stretched along the direction of sintering stress, its effective bearing area is $A\cos\theta$. When stretched in the vertical direction, the effective bearing area is $A\sin\theta$. Moreover, for necks with θ varying from 0 to 90º, the stress state on the neck plane changes from pure tension to pure shear, which lead to a transition in fracture mode. Thus, geometrically, sintering necks with a smaller angle between the normal and tensile direction are more advantageous. Given the
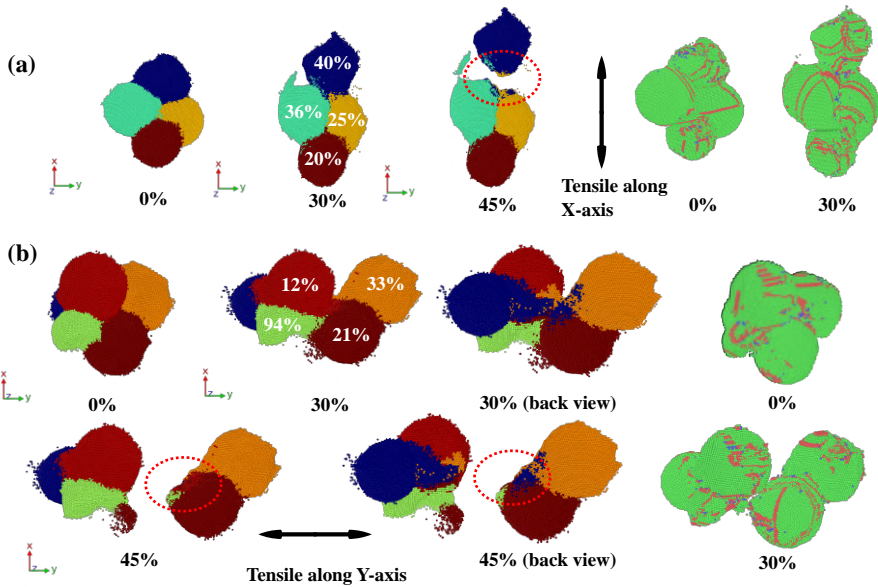
Figure 5.12: The fracture process during tensile deformation along (a) X-axis and (b) Y-axis. The model is sintered under stress along X-axis. Atoms are colored according to the particle they belong to. Left side shows the atomic structure with common neighbour analysis(CNA).

observed anisotropy in the orientation of sintering necks after sintering, θ angles of sintering necks observed along the X-axis are more likely to be smaller, leading to better mechanical performance when stretched along the X-axis.

In the micro-cantilever bending tests, the 45º specimens exhibited strength close to that of the 90º specimens. Considering that the orientation distribution of sintering necks has a peak at 45º, it can be inferred that when stretched at a 45º angle to the sintering stress direction, many necks align favorably, resulting in better performance.

Due to the complexity of the sintered particle structure, the effects of areal relative density fluctuations, sintering neck orientation, and other factors not considered (such as grain boundary types and grain orientations) are superimposed.

5.6 Conclusion

The mechanical strength of sintered NPs limits their application in advanced electronics packaging. In this work, we reveal the anisotropy in the microstructure and mechanical properties of sintered Cu NPs by combining experimental methods with MD simulations. We clearly explain the processing-microstructure-property relationship of pressure-assisted sintered Cu NPs. The main findings are as follows:

1. The evolution of the microstructure during sintering is quantitatively described by areal relative density, which shows distinct differences in each direction during stress-assisted sintering. Directions along the stress exhibit a quick decrease in the minimum and SD of areal relative density, while directions perpendicular to the stress show an increase in SD. For sintering under hydrostatic stress, changes in all directions are similar.

2. MD simulations reveal that the necks formed during sintering are anisotropic. Necks tend to attain a smaller angle between their normal and the stress direction. Additionally, necks with such favorable orientation can achieve larger sizes.

3. The anisotropy in the mechanical properties of Cu NPs sintered under uniaxial stress is demonstrated by both micro-cantilever tests and tensile simulations. Along the direction of the sintering stress, the strength (load in experiments and toughness in simulations) is significantly higher (41% in experiments and 108% in simulations) than that along the perpendicular directions.

4. The mechanical anisotropy is induced by the microstructure through two aspects: variations in areal relative density affect the tendency for strain localization, and the size and orientation of necks affect the fracture mode. Along the direction of the sintering stress, the structure is more uniform, and more necks are in favorable orientations, resulting in higher strength compared to other directions.

We expect this study to provide new insights for nanoscale experimental design and performance analysis, as well as inform the design of NPs sintering processes.

References

[1] CR Eddy Jr and DK Gaskill. Silicon carbide as a platform for power electronics. *Science*, 324(5933):1398–1400, 2009.

[2] Cyril Buttay, Dominique Planson, Bruno Allard, Dominique Bergogne, Pascal Bevilacqua, Charles Joubert, Mihai Lazar, Christian Martin, Hervé Morel, Dominique Tournier, et al. State of the art of high temperature power electronics. *Materials Science and Engineering: B*, 176(4):283–288, 2011.

[3] Yue Gao, Shuhei Takata, Chuantong Chen, Shijo Nagao, Katsuaki Suganuma, Amir Sajjad Bahman, and Francesco Iannuzzo. Reliability analysis of sintered Cu joints for SiC power devices under thermal shock condition. *Microelectronics Reliability*, 100:113456, 2019.

5

[4] AU Telang, TR Bieler, A Zamiri, and F Pourboghrat. Incremental recrystal-lization/grain growth driven by elastic strain energy release in a thermome-chanically fatigued lead-free solder joint. *Acta Materialia*, 55(7):2265–2277, 2007.

[5] Muhammad Sadiq, Maaz Khan, Abdul Mateen, Muhammad Shahzad, Kareem Akhtar, Jawad Khan, et al. Thermal aging impact on microstructure, creep and corrosion behavior of lead-free solder alloy (SAC387) use in electronics. *Microelectronics Reliability*, 122:114180, 2021.

[6] Wenwu Zhang, Penghao Zhang, Dashi Lu, Hao Pan, Xiangli Liu, Chengyan Xu, Jun Wei, Mingyu Li, and Hongjun Ji. A supersaturated Cu-Ag nanoalloy joint with ultrahigh shear strength and ultrafine nanoprecipitates for power electronic packaging. *Journal of Materials Science & Technology*, 145:56–65, 2023.

[7] Jintao Wang, Ziwen Lv, Luobin Zhang, Fangcheng Duan, Jianqiang Wang, Fuquan Li, Hongtao Chen, and Mingyu Li. Nucleation and growth of Cu_6Sn_5 during the aging process of Cu/Sn interface in electronic packaging-by in-situ TEM. *Acta Materialia*, 264:119581, 2024.

[8] MA Asoro, PJ Ferreira, and D Kovar. In situ transmission electron microscopy and scanning transmission electron microscopy studies of sintering of Ag and Pt nanoparticles. *Acta Materialia*, 81:173–183, 2014.

[9] SuYan Zhao, Xin Li, YunHui Mei, and GuoQuan Lu. Study on high temper-ature bonding reliability of sintered nano-silver joint on bare copper plate. *Microelectronics Reliability*, 55(12):2524–2531, 2015.

[10] Xu Long, Zhen Li, Xiuzhen Lu, Hongcun Guo, Chao Chang, Qianran Zhang, Abdelhafid Zehri, Wei Ke, Yao Yao, Lilei Ye, et al. Mechanical behaviour of sintered silver nanoparticles reinforced by SiC microparticles. *Materials Science and Engineering: A*, 744:406–414, 2019.

[11] Bowen Zhang, Chuantong Chen, Takuya Sekiguchi, Yang Liu, Caifu Li, and Katsuaki Suganuma. Development of anti-oxidation Ag salt paste for large-area (35×35 mm^2) Cu-Cu bonding with ultra-high bonding strength. *Journal of Materials Science & Technology*, 113:261–270, 2022.

[12] Wei Chen, Xu Liu, Dong Hu, Xi Zhu, Xuejun Fan, Guoqi Zhang, and Jiajie Fan. Unraveling the hydrogen sulfide aging mechanism on electrical-thermal–mechanical property degradation of sintered nanocopper interconnects used in power electronics packaging. *Materials & Design*, 238:112702, 2024.

[13] Sathish K Kurapati, N Mahendar Reddy, R Sujithra, Ramesh Kola, Gubbala V Ramesh, and D Saritha. Nanomaterials and nanostructures in additive manufacturing: properties, applications, and technological challenges. *Nanotechnology-Based Additive Manufacturing: Product Design, Properties and Applications*, 1:53–102, 2023.

[14] O Lame, D Bellet, M Di Michiel, and D Bouvard. Bulk observation of metal powder sintering by X-ray synchrotron microtomography. *Acta materialia*, 52(4):977–984, 2004.

[15] Ruzhong Zuo, Emil Aulbach, Rajendra K Bordia, and Jürgen Rödel. Critical evaluation of hot forging experiments: case study in alumina. *Journal of the American Ceramic Society*, 86(7):1099–1105, 2003.

[16] David J Green, Olivier Guillon, and Jürgen Rödel. Constrained sintering: A delicate balance of scales. *Journal of the European Ceramic Society*, 28(7):1451–1466, 2008.

[17] Haixia Shang, Aravind Mohanram, Eugene Olevsky, and Rajendra K Bordia. Evolution of anisotropy in hierarchical porous ceramics during sinter-forging. *Journal of the European Ceramic Society*, 36(12):2937–2945, 2016.

[18] Olivier Guillon, Ludwig Weiler, and Jürgen Rödel. Anisotropic microstructural development during the constrained sintering of dip-coated alumina thin films. *Journal of the American Ceramic Society*, 90(5):1394–1400, 2007.

[19] CL Martin and RK Bordia. The effect of a substrate on the sintering of constrained films. *Acta Materialia*, 57(2):549–558, 2009.

[20] Tiam Foo Chen and Kim Shyong Siow. Comparing the mechanical and thermal-electrical properties of sintered copper (Cu) and sintered silver (Ag) joints. *Journal of alloys and Compounds*, 866:158783, 2021.

[21] Yang Zuo, Cong Zhao, Ana Robador, Martin Wickham, and Samjid H Mannan. Quasi-in-situ observation of the grain growth and grain boundary movement in sintered Cu nanoparticle interconnects. *Acta Materialia*, 236:118135, 2022.

[22] Toni Youssef, Wafaa Rmili, Eric Woirgard, Stephane Azzopardi, Nicolas Vivet, Donatien Martineau, Régis Meuret, Guenhael Le Quilliec, and Caroline Richard. Power modules die attach: A comprehensive evolution of the nanosilver sintering physical properties versus its porosity. *Microelectronics Reliability*, 55(9-10):1997–2002, 2015.

5

[23] Bo Chen, Zhenbo Xia, and Kathy Lu. Understanding sintering characteristics of ZnO nanoparticles by FIB-SEM three-dimensional analysis. *Journal of the European Ceramic Society*, 33(13-14):2499–2507, 2013.

[24] Gaku Okuma, Ryo Miyaki, Kan Shinobe, Anna Sciazko, Takaaki Shimura, Zilin Yan, Shotaro Hara, Toshinori Ogashiwa, Naoki Shikazono, and Fumihiro Wakai. Anisotropic microstructural evolution and coarsening in free sintering and constrained sintering of metal film by using FIB-SEM tomography. *Acta Materialia*, 215:117087, 2021.

[25] Aatreya Manjulagiri Venkatesh, Didier Bouvard, Pierre Lhuissier, Julie Villanova, and Cyril Rajon. In-situ 3D X-ray investigation of ceramic powder sintering at the particle length-scale. *Ceramics International*, 50(3):4715–4728, 2024.

[26] Aatreya Manjulagiri Venkatesh, Didier Bouvard, Pierre Lhuissier, and Julie Villanova. 3D analysis of ceramic powder sintering by synchrotron X-ray nano-tomography. *Journal of the European Ceramic Society*, 43(6):2553–2563, 2023.

[27] Pascal Gadaud, Vincenzo Caccuri, Denis Bertheau, James Carr, and Xavier Milhet. Ageing sintered silver: relationship between tensile behavior, mechanical properties and the nanoporous structure evolution. *Materials Science and Engineering: A*, 669:379–386, 2016.

[28] Chuantong Chen and Katsuaki Suganuma. Microstructure and mechanical properties of sintered Ag particles with flake and spherical shape from nano to micro size. *Materials & Design*, 162:311–321, 2019.

[29] Chuantong Chen, Shijo Nagao, Katsuaki Suganuma, Jinting Jiu, Tohru Sugahara, Hao Zhang, Tomohito Iwashige, Kazuhiko Sugiura, and Kazuhiro Tsuruta. Macroscale and microscale fracture toughness of microporous sintered Ag for applications in power electronic devices. *Acta Materialia*, 129:41–51, 2017.

[30] Leiming Du, Dong Hu, René Poelm, Willem Van Driel, and Kouchi Zhang. Micro-cantilever bending test of sintered Cu nanoparticles for power electronic devices. In *2023 24th International Conference on Thermal, Mechanical and Multi-Physics Simulation and Experiments in Microelectronics and Microsystems (EuroSimE)*, pages 1–4. IEEE, 2023.

[31] Dong Hu, Leiming Du, Markus Alfreider, Jiajie Fan, Daniel Kiener, and Guoqi Zhang. Microscopic fracture toughness of notched porous sintered Cu micro-

cantilevers for power electronics packaging. *Materials Science and Engineering: A*, 897:146316, 2024.

[32] Brayan Paredes-Goyes, David Jauffres, Jean-Michel Missiaen, and Christophe L Martin. Grain growth in sintering: A discrete element model on large packings. *Acta Materialia*, 218:117182, 2021.

[33] A Wonisch, O Guillon, T Kraft, M Moseler, H Riedel, and J Rödel. Stress-induced anisotropy of sintering alumina: Discrete element modelling and experiments. *Acta Materialia*, 55(15):5187–5199, 2007.

[34] Branislav Dzepina, Daniel Balint, and Daniele Dini. A phase field model of pressure-assisted sintering. *Journal of the European Ceramic Society*, 39(2-3):173–182, 2019.

[35] Johannes Hötzer, Marco Seiz, Michael Kellner, Wolfgang Rheinheimer, and Britta Nestler. Phase-field simulation of solid state sintering. *Acta Materialia*, 164:184–195, 2019.

[36] Robert Termuhlen, Xanthippi Chatzistavrou, Jason D Nicholas, and Hui-Chia Yu. Three-dimensional phase field sintering simulations accounting for the rigid-body motion of individual grains. *Computational Materials Science*, 186:109963, 2021.

[37] Shota Okuno, Qiang Yu, and Yusuke Nakata. Influence of sintering conditions on mechanical properties of Ag-nano sintered material. In *2016 IEEE 18th Electronics Packaging Technology Conference (EPTC)*, pages 488–491. IEEE, 2016.

[38] Gong He, Guo Hongcun, Li Shujin, Zhou Junwen, and Yao Yao. Compressive failure mechanism of sintered nano-silver. *Journal of Materials Research*, 38(18):4201–4213, 2023.

[39] Yutai Su, Guicui Fu, Changqing Liu, Kun Zhang, Liguo Zhao, Canyu Liu, Allan Liu, and Jianan Song. Thermo-elasto-plastic phase-field modelling of mechanical behaviours of sintered nano-silver with randomly distributed micro-pores. *Computer Methods in Applied Mechanics and Engineering*, 378:113729, 2021.

[40] Lifeng Ding, Ruslan L Davidchack, and Jingzhe Pan. A molecular dynamics study of sintering between nanoparticles. *Computational Materials Science*, 45(2):247–256, 2009.

[41] Dong Hu, Zhen Cui, Jiajie Fan, Xuejun Fan, and Guoqi Zhang. Thermal kinetic and mechanical behaviors of pressure-assisted Cu nanoparticles sintering: A molecular dynamics study. *Results in Physics*, 19:103486, 2020.

5

[42] Yanan Hu, Yuexing Wang, and Yao Yao. Molecular dynamics on the sintering mechanism and mechanical feature of the silver nanoparticles at different temperatures. *Materials Today Communications*, 34:105292, 2023.

[43] Jingxiang Xu, Yuji Higuchi, Nobuki Ozawa, Kazuhisa Sato, Toshiyuki Hashida, and Momoji Kubo. Parallel large-scale molecular dynamics simulation opens new perspective to clarify the effect of a porous structure on the sintering process of Ni/YSZ multiparticles. *ACS applied materials & interfaces*, 9(37):31816–31824, 2017.

[44] Qingwei Guo, Hua Hou, Kaile Wang, Muxi Li, Peter K Liaw, and Yuhong Zhao. Coalescence of Al0.3CoCrFeNi polycrystalline high-entropy alloy in hot-pressed sintering: a molecular dynamics and phase-field study. *npj Computational Materials*, 9(1):185, 2023.

[45] Yunus Onur Yildiz. Morphological evolution of irregularly shaped Au nanoparticles during the sintering process and their mechanical performance. *Computational Particle Mechanics*, 10(6):1659–1667, 2023.

[46] Xu Liu, Shizhen Li, Jiajie Fan, Jing Jiang, Yang Liu, Huaiyu Ye, and Guoqi Zhang. Microstructural evolution, fracture behavior and bonding mechanisms study of copper sintering on bare DBC substrate for SiC power electronics packaging. *Journal of Materials Research and Technology*, 19:1407–1421, 2022.

[47] Leiming Du, Xiangnan Pan, and Youshi Hong. New insights into microstructure refinement in crack initiation region of very-high-cycle fatigue for SLM Ti-6Al-4V via precession electron diffraction. *Materialia*, 33:102008, 2024.

[48] Lu Qi, Suyun He, Chunjin Chen, Binbin Jiang, Yulin Hao, Hengqiang Ye, Rui Yang, and Kui Du. Diffusional-displacive transformation in a metastable β titanium alloy and its strengthening effect. *Acta Materialia*, 195:151–162, 2020.

[49] Xin Liu, Yu Zhou, Xinjie Zhu, Duoduo Wang, and Qunbo Fan. The failure mechanism at adiabatic shear bands of titanium alloy: high-precision survey using precession electron diffraction and geometrically necessary dislocation density calculation. *Materials Science and Engineering: A*, 746:322–331, 2019.

[50] Teng-Jan Chang, Hsing-Yang Chen, Chin-I Wang, Hsin-Chih Lin, Chen-Feng Hsu, Jer-Fu Wang, Chih-Hung Nien, Chih-Sheng Chang, Iuliana P Radu, and Miin-Jang Chen. Wake-up-free ferroelectric Hf0.5Zr0.5O2 thin films characterized by precession electron diffraction. *Acta Materialia*, 246:118707, 2023.

[51] Niels Cautaerts, Edgar F Rauch, Jiwon Jeong, Gerhard Dehm, and Christian H Liebscher. Investigation of the orientation relationship between nano-sized G-phase precipitates and austenite with scanning nano-beam electron diffraction using a pixelated detector. *Scripta Materialia*, 201:113930, 2021.

[52] Hongyu Xiao, Zhiping Wang, Jiwei Geng, Chengcheng Zhang, Yugang Li, Qing Yang, Mingliang Wang, Dong Chen, Zhuguo Li, and Haowei Wang. Precipitation and crystallographic relationships of nanosized η/η' precipitates at S-Al interface in Al-Zn-Mg-Cu alloy. *Scripta Materialia*, 214:114643, 2022.

[53] Jiwon Jeong, Niels Cautaerts, Gerhard Dehm, and Christian H Liebscher. Automated crystal orientation mapping by precession electron diffraction-assisted four-dimensional scanning transmission electron microscopy using a scintillator-based CMOS detector. *Microscopy and Microanalysis*, 27(5):1102–1112, 2021.

[54] Mario F Heinig, Dipanwita Chatterjee, Antonius TJ van Helvoort, Jakob Birkedal Wagner, Shima Kadkhodazadeh, Håkon Wiik Ånes, Frank Niessen, and Alice Bastos da Silva Fanta. High resolution crystal orientation mapping of ultrathin films in SEM and TEM. *Materials Characterization*, 189:111931, 2022.

[55] Ronan Henry, Thierry Blay, Thierry Douillard, Armel Descamps-Mandine, Isabelle Zacharie-Aubrun, Jean-Marie Gatt, Cyril Langlois, and Sylvain Meille. Local fracture toughness measurements in polycrystalline cubic zirconia using micro-cantilever bending tests. *Mechanics of Materials*, 136:103086, 2019.

[56] Daniel Sorensen, Eric Hintsala, Joseph Stevick, Jesse Pischlar, Bernard Li, Daniel Kiener, Jason C Myers, Hui Jin, Jia Liu, Douglas Stauffer, et al. Intrinsic toughness of the bulk-metallic glass vitreloy 105 measured using micro-cantilever beams. *Acta Materialia*, 183:242–248, 2020.

[57] Hao Zhang, Chuantong Chen, Jinting Jiu, Shijo Nagao, and Katsuaki Suganuma. Microstructural homogeneity of sintered Ag joint after pressureless sintering process. In *2017 International Conference on Electronics Packaging (ICEP)*, pages 122–124. IEEE, 2017.

[58] Chuantong Chen, Zheng Zhang, Dongjin Kim, Tetsuya Sasamura, Yukinori Oda, Ming-Chun Hsieh, Aya Iwaki, Aiji Suetake, and Katsuaki Suganuma. Interface reaction and evolution of micron-sized Ag particles paste joining on electroless Ni-/Pd-/Au-finished DBA and DBC substrates during extreme thermal shock test. *Journal of Alloys and Compounds*, 862:158596, 2021.

5

[59] Fan Yang, Wenbo Zhu, Weizhen Wu, Hongjun Ji, Chunjin Hang, and Mingyu Li. Microstructural evolution and degradation mechanism of SiC–Cu chip attachment using sintered nano-Ag paste during high-temperature ageing. *Journal of Alloys and Compounds*, 846:156442, 2020.

[60] Tamás Csanádi, Ahmad Azizpour, Marek Vojtko, and William G Fahrenholtz. The effect of crystal anisotropy on fracture toughness and strength of ZrB_2 microcantilevers. *Journal of the American Ceramic Society*, 107(3):1669–1681, 2024.

[61] Jicheng Gong and Angus J Wilkinson. Anisotropy in the plastic flow properties of single-crystal α titanium determined from micro-cantilever beams. *Acta Materialia*, 57(19):5693–5705, 2009.

[62] Gerhard Dehm, Balila Nagamani Jaya, Rejin Raghavan, and Christoph Kirchlechner. Overview on micro-and nanomechanical testing: New insights in interface plasticity and fracture at small length scales. *Acta Materialia*, 142:248–282, 2018.

[63] Aidan P Thompson, H Metin Aktulga, Richard Berger, Dan S Bolintineanu, W Michael Brown, Paul S Crozier, Pieter J In't Veld, Axel Kohlmeyer, Stan G Moore, Trung Dac Nguyen, et al. LAMMPS-a flexible simulation tool for particle-based materials modeling at the atomic, meso, and continuum scales. *Computer Physics Communications*, 271:108171, 2022.

[64] Alexander Stukowski. Visualization and analysis of atomistic simulation data with OVITO–the open visualization tool. *Modelling and simulation in materials science and engineering*, 18(1):015012, 2009.

[65] Yu Mishin, MJ Mehl, DA Papaconstantopoulos, AF Voter, and JD Kress. Structural stability and lattice defects in copper: Ab initio, tight-binding, and embedded-atom calculations. *Physical Review B*, 63(22):224106, 2001.

[66] Yu Mishin, M Asta, and Ju Li. Atomistic modeling of interfaces and their impact on microstructure and properties. *Acta Materialia*, 58(4):1117–1151, 2010.

[67] Timofey Frolov, David L Olmsted, Mark Asta, and Yuri Mishin. Structural phase transformations in metallic grain boundaries. *Nature communications*, 4(1):1899, 2013.

[68] Jian Han, Spencer L Thomas, and David J Srolovitz. Grain-boundary kinetics: A unified approach. *Progress in Materials Science*, 98:386–476, 2018.

[69] B Henrich, A Wonisch, T Kraft, M Moseler, and H Riedel. Simulations of the influence of rearrangement during sintering. *Acta Materialia*, 55(2):753–762, 2007.

[70] Douglas E Spearot, Mark A Tschopp, Karl I Jacob, and David L McDowell. Tensile strength of <1 0 0> and <1 1 0> tilt bicrystal copper interfaces. *Acta materialia*, 55(2):705–714, 2007.

[71] Daniel Trias, Josep Costa, Albert Turon, and JE Hurtado. Determination of the critical size of a statistical representative volume element (SRVE) for carbon reinforced polymers. *Acta materialia*, 54(13):3471–3484, 2006.

[72] IM Gitman, Harm Askes, and LJ Sluys. Representative volume: Existence and size determination. *Engineering fracture mechanics*, 74(16):2518–2534, 2007.

[73] Swantje Bargmann, Benjamin Klusemann, Jürgen Markmann, Jan Eike Schnabel, Konrad Schneider, Celal Soyarslan, and Jana Wilmers. Generation of 3D representative volume elements for heterogeneous materials: A review. *Progress in Materials Science*, 96:322–384, 2018.

[74] Xiaohui Tu, Ahmad Shahba, Jinlei Shen, and Somnath Ghosh. Microstructure and property based statistically equivalent RVEs for polycrystalline-polyphase aluminum alloys. *International Journal of Plasticity*, 115:268–292, 2019.

[75] RB Vieira, H Sehitoglu, and J Lambros. Representative volume elements for plasticity and creep measured from high-resolution microscale strain fields. *Acta Materialia*, 214:117021, 2021.

[76] Joseph Lifton and Tong Liu. An adaptive thresholding algorithm for porosity measurement of additively manufactured metal test samples via X-ray computed tomography. *Additive Manufacturing*, 39:101899, 2021.

[77] Małgorzata Makowska, Pradeep Vallachira Warriam Sasikumar, Lorenz Hagelüken, Dario F Sanchez, Nicola Casati, Federica Marone, Gurdial Blugan, Jürgen Brugger, and Helena Van Swygenhoven. Cracks, porosity and microstructure of Ti modified polymer-derived SiOC revealed by absorption-, XRD-and XRF-contrast 2D and 3D imaging. *Acta Materialia*, 198:134–144, 2020.

[78] Hans E Exner and Eduard Arzt. Sintering processes. *Sintering Key Papers*, pages 157–184, 1990.

[79] Wole Soboyejo. *Mechanical properties of engineered materials*. CRC press, 2002.

[80] Xu Long, Chongyang Du, Zhen Li, Hongcun Guo, Yao Yao, Xiuzhen Lu, Xiaowu Hu, Lilei Ye, and Johan Liu. Finite element analysis to the constitutive behavior of sintered silver nanoparticles under nanoindentation. *International Journal of Applied Mechanics*, 10(10):1850110, 2018.

[81] Yutai Su, Ziyi Shen, Xu Long, Chuantong Chen, Lehua Qi, and Xujiang Chao. Gaussian filtering method of evaluating the elastic/elasto-plastic properties of sintered nanocomposites with quasi-continuous volume distribution. *Materials Science and Engineering: A*, 872:145001, 2023.

[82] Yutai Su, Jiaqi Zhu, Xu Long, Liguo Zhao, Chuantong Chen, and Changqing Liu. Statistical effects of pore features on mechanical properties and fracture behaviors of heterogeneous random porous materials by phase-field modeling. *International Journal of Solids and Structures*, 264:112098, 2023.

[83] Jörg Hohe and Volker Hardenacke. Analysis of uncertainty effects due to microstructural disorder in cellular or porous materials. *International Journal of Solids and Structures*, 49(7-8):1009–1021, 2012.

[84] Gong He, Yao Yao, and Yang Yuting. Size effect on the fracture of sintered porous nano-silver joints: Experiments and Weibull analysis. *Journal of Alloys and Compounds*, 863:158611, 2021.

5

6

CONCLUSIONS AND OUTLOOK

6.1 Conclusions

In this thesis, I explored several aspects of the anisotropy in metallic materials, covering elastic and plastic regimes, microscale and macroscale.

I first investigated the incompatibility stress near grain boundaries induced by the elastic anisotropy of crystalline materials, using a bicrystal model. Although previous studies had explored incompatibility stress, they primarily focused on special grain boundaries. I demonstrated a unique property of the rotation for all fourth-rank tensors, here the elastic tensor: under Voigt notation, the rotated fourth-rank tensor can be expressed as the sum of the original tensor and a product of the anisotropy index and a rotation matrix-dependent function. Leveraging this transformation for elasticity, I derived the maximum incompatibility stress near the grain boundary under an external uniaxial load perpendicular to the grain boundary plane (Y-direction). I quantified incompatibility factor as $IF = (\sigma_1 + \sigma_3)/\sigma^{\mathrm{E}}$, then

$$
\begin{aligned}
IF^{\mathrm{max}} &= \frac{4s_{11} - 4s_{12} - 2s_{44}}{10s_{11} + 14s_{12} + s_{44}} \\
&= \frac{-2(C_{11} - C_{12} - 2C_{44})(C_{11} + 2C_{12})}{(10C_{11} - 4C_{12})C_{44} + (C_{11} - C_{12})(C_{11} + 2C_{12})},
\end{aligned}
\tag{6.1}
$$

where s_{ij} and C_{ij} are elastic components for cubic crystals within engineering Voigt notation (xx $\to$ 1, yy $\to$ 2, zz $\to$ 3, yz $\to$ 4, xz $\to$ 5, xy $\to$ 6, $\epsilon_4 = \epsilon_{yz} + \epsilon_{zy}$). For general grain boundaries, when placing a grain boundary plane in the XOZ plane and applying an external stress along the Y-axis, the IF is estimated as

$$
\begin{aligned}
IF &\approx \frac{1/E_{\mathrm{Y}}^{\mathrm{I}} - 1/E_{\mathrm{Y}}^{\mathrm{II}}}{(F_{22}^{\mathrm{I}} + F_{22}^{\mathrm{II}})\chi + 4s_{11} + 4s_{12}} \\
&\approx \frac{6(1/E_{\mathrm{Y}}^{\mathrm{I}} - 1/E_{\mathrm{Y}}^{\mathrm{II}})}{10s_{11} + 14s_{12} + s_{44}},
\end{aligned}
\tag{6.2}
$$

where $E_{\mathrm{Y}}^{\mathrm{I}}$ ($E_{\mathrm{Y}}^{\mathrm{II}}$) is the Young's modulus of grain I (II) along the global Y-axis. These findings provide insight into stress distributions in polycrystalline materials, which is critical for understanding material failure mechanisms such as crack propagation, creep, and fatigue. Furthermore, the understanding of incompatibility stress informs the design of texture, grain boundary engineering, and segregation engineering, thereby advancing the development of high-performance materials.

Building on the knowledge of IF, the influence of the grain boundary inclination angle relative to the uniaxial load direction on the incompatibility stress is systematically investigated. I discovered that for cubic crystals under arbitrary external stress states it is the deviatoric stress tensor that induces incompatibility stress at the grain boundary, while the hydrostatic stress component has no effect. For uniaxial loading, the maximum stress concentration at the grain boundary is

closely related to its spatial orientation. The grain boundary orientation is described by the angle between the grain boundary normal and the loading direction. For materials with $IF < 1$, the maximum incompatibility stress (or stress concentration) is likely to occur at grain boundaries oriented at 90°, while for materials with $IF > 1$, the maximum incompatibility stress tends to occur at grain boundaries oriented between 40° and 50°.

Next, I investigated the anisotropic plastic behavior of pearlite, a microstructure with important engineering applications. Pearlite is composed of alternating ferrite and cementite layers. For lamellar-structured pearlite with the Bagaryatskii orientation relationship, I analytically analyzed the elastic properties and slip systems in both cementite and ferrite using a modified bicrystal model. Surprisingly, a significant variation in the maximal Schmid factor was observed across different loading directions. Through carefully designed supercells, I demonstrated significant anisotropy in the plastic deformation of pearlite using molecular dynamics simulations. Simulation results showed that for loading directions within the interface plane, the yield strengths of pearlite ranged from a minimum of 9.5 GPa to a maximum of 17.0 GPa (calculated at a strain rate of $1 \times 10^9 s^{-1}$). It was generally argued that plastic deformation initiates in ferrite, with significant dislocation pile-up near the interface facilitating slip transfer into cementite layers. Interestingly, I found that under certain loading directions, slip bands in cementite activate before those in ferrite. Based on these observations, I propose a sequence of strengthening mechanisms: initial work-hardening in ferrite, slip activation in favorably oriented cementite, and slip transfer into unfavorably oriented cementite. These mechanisms, coupled with interfacial effects and carbon dissolution, result in sustained work-hardening over a wide range of strains, which explains the remarkable plastic deformation and exceptional tensile strength of pearlite. Additionally, both dislocations at the interface and the Schmid factor critically influence the activation of slip systems. This work provides two insights for material design. First, in pearlite, the orientation relationship between the lamellar stacking direction and the external loading direction does not fully capture its mechanical properties. Second, the successive strengthening mechanism in pearlite suggests a design strategy for other eutectic alloys to achieve high strength and ductility.

Finally, I investigated the relationship between the anisotropic mechanical properties and structural characteristics of sintered copper nanoparticles with porous structures. Unlike other sources of anisotropy, the structural anisotropy in sintered copper nanoparticles arises from the sintering process, where uniaxial compressive stress is typically applied to promote densification. However, this compressive stress also influences the structural evolution. Molecular dynamics simulations is employed to study the sintering and tensile processes of copper nanoparticles. While previous studies have focused on parameters such as relative density and

6

minimum areal density, here the structural differences in various directions are quantified using the orientation distribution of sintering necks and the uniformity of areal density across different orientations. This provides a new perspective for characterizing the structure of porous metallic materials. Simulations revealed that, along the loading direction during sintering, the areal relative density shows less variation, and sintering necks tend to align perpendicular to this direction, improving strength and fracture toughness in that direction. These findings agree well with experimental results. Principal component analysis is used to determine the orientation of sintering necks and employed statistical methods to elucidate the relationship between sintering neck orientation, deformation mechanisms, and the resulting strength and toughness of the sintered particles. This work demonstrates the potential of molecular dynamics simulations for studying grain boundary and surface-related behaviors during the sintering of multiple particles. It also provides insights for developing next-generation electronic packaging materials through combined experimental and simulation approaches.

This work underscores the significance of often-overlooked aspects in engineering applications. These factors may contribute to material failure, such as plastic deformation from stress concentration, indicating that more homogeneous materials could better satisfy specific needs. Conversely, tailoring these anisotropies can enhance material performance. Given developments in material processing and the use of materials at micro- and nanoscale levels, studies on the anisotropy across length scales may inform material design and microstructure optimization.

6.2 Outlook

This thesis has certain limitations and areas for future improvement. Future work could focus on the following three aspects:

i) Chapter 2 focused exclusively on the elastic anisotropy of cubic crystals. However, the methodology developed can be extended to other crystal systems and heterogeneous interfaces. For high-entropy alloys, where elastic constants vary significantly, the impact of crystalline anisotropy on microstructure evolution and mechanical properties remains largely unexplored.

ii) Although I have demonstrated the existence of incompatibility stress near grain boundaries within the framework of continuum mechanics, the stress on atoms in imperfect crystalline regions, particularly at grain boundaries, is strongly influenced by their local atomic environments as well. These atoms typically exhibit high potential energy and enhanced diffusivity, significantly affecting the properties of the material. Emerging high-precision interatomic potentials and advanced atomic environment descriptors could potentially

provide a more comprehensive description of the stress states of atoms near grain boundaries.

iii) In Chapter 4, I investigated the influence of the stress field near grain boundaries on slip activation. I anticipate that this stress field may have an even greater impact on phenomena that take place at longer time scales, such as diffusion and creep. While phase-field-based studies have explored these effects, atomic-scale investigations remain scarce. I hope to elucidate the influence of grain boundary stress fields on diffusion and creep at the atomic scale or to uncover relevant experimental evidence.

iv) In studying the sintering of nanoparticles, I recognized the importance of the initial powder distribution. In this work, I used a random generation method to construct multi-particle models, which resulted in a lower relative density compared to experimental observations. To better capture the effects of particle shape and size distribution, the modeling process should account for inter-particle sliding and friction, for example, by employing the discrete element method. This approach would enable a more accurate description of the sintering of non-spherical particles and powders with higher packing densities, aligning more closely with real-world conditions.

6

CURRICULUM VITÆ

Kai LIU

Born on February 04 1997 in Shaanxi, China

EDUCATION

04.2021-10.2025   PhD candidate in Material Science and Engineering
                    Delft University of Technology, the Netherlands

09.2018-07.2020   Master of Engineering in Materials Science
                    Harbin Institute of Technology, China

09.2014-07.2018   Bachelor in Material Science and Engineering
                    Harbin Institute of Technology, China

LIST OF PUBLICATIONS

JOURNAL ARTICLES

1. **Kai Liu**, Marcel HF Sluiter. "Stresses at grain boundaries: The maximum incompatibility stress in an infinitely extended elastic bicrystal under uniaxial loading." Scripta Materialia 234 (2023): 115570. 🏆

2. **Kai Liu**, Marcel HF Sluiter. "Incompatibility stress at inclined grain boundaries for cubic crystals under hydrostatic stress and uniaxial stress." Materialia 34 (2024): 102071.

3. **Kai Liu**, Fei Shuang, Marcel HF Sluiter. "Plastic Anisotropy in Pearlite: a Molecular Dynamics study with insights from the Periodic Bicrystal Model." Acta Materialia (2025): 121100.

4. Leiming Du, **Kai Liu** (co-first author), Dong Hu, Olof Bäcke, Xiao Hu, Xinrui Ji, Jiajie Fan, René H. Poelma, Magnus Hörnqvist Colliander, Guoqi Zhang. "Microstructural and mechanical anisotropy in pressure-assisted sintered copper nanoparticles." Acta Materialia (2025): 120772.

CO-AUTHORED ARTICLES

1. Jia-Ning Zhu, **Kai Liu**, Ton Riemslag, Frans D Tichelaar, Evgenii Borisov, Xiyu Yao, Anatoly Popovich, Richard Huizenga, Marcel Hermans, Vera Popovich. "Achieving superelasticity in additively manufactured Ni-lean NiTi by crystallographic design." Materials & Design 230 (2023): 111949.

2. Leiming Du, Xinrui Ji, **Kai Liu**, Jiajie Fan, Guoqi Zhang. "Investigating Coalescence Kinetics in Cu Nanoparticle by Molecular Dynamics and 3D Reconstruction." 2024 25th International Conference on Electronic Packaging Technology (ICEPT). IEEE, 2024.

3. Fei Shuang, **Kai Liu**, Yucheng Ji, Wei Gao, Luca Laurenti, Poulumi Dey. "Modeling Extensive Defects in Metals through Classical Potential-Guided Sampling and Automated Configuration Reconstruction." npj Computational Materials 11.1 (2025): 118.

4. Fei Shuang, Zixiong Wei, **Kai Liu**, Wei Gao, Poulumi Dey. "Universal machine learning interatomic potentials poised to supplant DFT in modeling general defects in metals and random alloys." Machine Learning: Science and Technology (2025).

🗎 Included in this thesis.

🏆 Acta Student Award, 2023

Acknowledgments

As my doctoral journey comes to an end, I find myself filled with a deep sense of nostalgia as I reflect on these past years. When I first became a PhD candidate, my senior colleague Rutger told me, "Four years seem like a long time, but when you don't pay attention, time slips by very fast." Over the years, I often recalled these words, and now, standing at the finish line, I truly understand their meaning. These years have been incredibly rewarding: the guidance of my supervisor, the camaraderie of friends and colleagues, the unique experience of living in a foreign country, and the growth in my research capabilities. I vividly remember the moment I made a breakthrough and excitedly presented my results to my supervisor, who exclaimed, "Wow, this is really something!" Seeing a chaotic jumble of numbers suddenly reveal a clear pattern was an unforgettable experience. Equally memorable were the times when, stuck in a rut, friends would pull me away for meals, drinks, badminton, or cycling — moments of pure joy.

First and foremost, I would like to express my deepest gratitude to my supervisor, Marcel Sluiter. His profound knowledge, charismatic personality, and insightful thinking have left an indelible mark on me. I often found myself venturing into unfamiliar territories during our discussions, only to realize later how essential those explorations were. Marcel would often say, "Wait a moment, my thinking isn't that fast," but in reality, his intellectual speed was unparalleled. His rigorous approach to research and his insistence that "every paper must be ready for others to read, and every submission must reflect your best effort" have deeply influenced me. His passion for teaching and research has been a constant source of inspiration, and it is his invaluable guidance that set me on this academic path. I am also immensely grateful to my co-promotor, Poulumi Dey, for her insightful discussions and the numerous opportunities she provided for collaboration and exchange, which greatly enriched my understanding of various topics.

I would like to extend my special thanks to Dr. Fei Shuang, Dr. Jianing Zhu, and Leiming Du for their countless discussions, thought-provoking questions, and selfless assistance. Our fruitful collaborations not only broadened the scope of my research, but also deepened my understanding of materials science. Their dedication, efficiency, and creativity have profoundly influenced me, and I wish them continued success as they scale new heights in their scientific endeavors.

To my friends — Xuan Liu, Binbin Zhang, Zhaorui Yan, Jiaxiang Yi, Sifeng He, Yang Yang, Jianing Zhu, Yaqi Guo, Xiaohui Liang, Zixiong Wei, Keer Zhang, Ziyu

Li, Mingkai Zhang, and so many more (I apologize if I've missed anyone) — thank you for making this period of my life so enjoyable and colorful, especially during the challenging times of Covid-19. I wish you all the best for your future endeavors. I also want to thank my labmates, Rutger Slooter and Naveen Mohandas, for their help, encouragement, and all the happy moments we shared.

Finally, I owe my deepest gratitude to my family. Without your endless support, unwavering encouragement, and understanding, I could never have come this far. To my girlfriend, although we are in different countries, your love has always been a constant source of strength. I look forward to braving the waves of life together and continuing our journey with courage.

Kai Liu
Delft, February 2025